

Habilitation à diriger des recherches
de l'Université de Lille - Sciences et Technologies
Spécialité : **Sciences Physiques**

présentée par

Saliya Coulibaly

Dynamique spatio-temporelle
des systèmes dissipatifs hors équilibre :
de l'ordre vers le chaos

*Spatiotemporal dynamics of dissipative systems
out of equilibrium : from order to chaos*

Soutenue publiquement le 17 novembre 2017 devant le Jury composé de :

Arnaud COUAIRON	Rapporteur	CNRS/École Polytechnique
Philippe GRELU	Rapporteur	Université de Bourgogne
Juan Ariel LEVENSON	Rapporteur	CNRS/Université de Paris Sud
Stefan WABNITZ	Examineur	Università di Brescia
Marc DOUAY	Examineur	Université de Lille - Sciences et Technologies
Majid TAKI	Garant de l'HDR	Université de Lille - Sciences et Technologies

Avant-propos

"Physics would be dull and life most unfulfilling if all physical phenomena around us were linear. Fortunately, we are living in a nonlinear world. While linearization beautifies physics, nonlinearity provides excitement in physics", Y.R. Shen dans **The Principles of Nonlinear Optics**. Ce passage provient de l'un de mes plus anciens contacts avec la littérature de la Physique du non-linéaire. En le lisant pour la première fois, j'étais loin d'imaginer qu'il allait être l'essence même de toute ma carrière scientifique. L'optique non-linéaire a été ma porte d'entrée dans ce *monde* au début de ma thèse. Après celle-ci, les différentes techniques de modélisation mathématique et numérique que j'avais dû apprendre à utiliser m'ont donné les moyens d'accéder à un domaine encore plus vaste: l'étude des phénomènes d'auto-organisation.

Mes recherches de position post-doctoral m'ont alors conduit à l'Université du Chili à Santiago. L'objectif principal de ce projet post-doctoral était d'explorer la formation d'autres formes de structures spatiales localisées dans les systèmes forcés paramétriquement. Mon retour à Lille pour une seconde position post-doctorale, suivi de mon recrutement en tant que Maître de conférences a aussi consacré le retour de l'Optique non-linéaire parmi mes thématiques de recherche et plus particulièrement l'Optique non-linéaire guidée.

Ce mémoire d'habilitation porte donc sur des travaux de recherche réalisés depuis la fin de ma thèse. Ils sont le fruit de collaborations avec les personnes suivantes : Majid TAKI (Lille), Marcel CLERC (Santiago du Chili), Monica GARCIA-ÑUSTES (Valparaiso), Sylvain BARBAY (Saclay), Mustapha TLIDI (Bruxelles). Puisque *"Enseigner, c'est apprendre deux fois"*—Joseph Joubert, mes collaborations avec les chercheurs en formation pendant ces différentes étapes de mon parcours ont été autant d'opportunités d'accroître mes compétences.

Je profite de ce préambule pour témoigner ma gratitude envers les membres du jury. Je voudrais également remercier toutes les personnes avec qui j'ai eu le plaisir de travailler durant ces années de recherche : qu'ils sachent que toutes ces collaborations m'ont été extrêmement agréables.

Contents

1	Introduction	5
I	Mathematical modeling of physical systems	9
2	The driven chain of pendulum	13
3	The driven spin chain	17
4	The driven water channel	21
5	Propagation in optical fibre	23
II	Contribution to the study of dissipative localized structures	29
6	Parametric dissipative structures	33
6.1	Soliton pair interaction	33
6.2	Hidden dynamics of parametrically driven systems	38
7	Spatiotemporal dynamics in optical fiber systems	41
7.1	Convective/Absolute instability of the NLS equation	41
7.2	Spatiotemporal chaos and rogue waves dynamics	45
III	Conclusion and Perspectives	51

List of Figures

2.1	Schematic representation of a vertically driven chain of pendula	13
3.1	Schematic representation of ferromagnetic plane	17
4.1	Schematic representation of the water surface elevation	21
5.1	Optical fiber refractive index profile	23
5.2	Optical fiber ring resonator	26
6.1	Illustration of a state of pair of interacting dissipative solitons	33
6.2	Interaction and collapse processes (theory)	35
6.3	Interaction and collapse processes (exp.)	36
6.4	Illustration coalescence cascade	36
6.5	Verification of the self-similarity law	37
6.6	Phase Shielding Soliton states	38
6.7	Uniform phase soliton stability	39
6.8	Two-dimensional phase shielding soliton	40
7.1	Schematic illustration of pinching process	42
7.2	Local wavenumber of the impulse response	43
7.3	Normalized output profiles	43
7.4	Schematic absolute and convective instabilities	44
7.5	Secondary convective/absolute instability	44
7.6	Soliton-induced spatiotemporal chaos in fiber ring cavity	47
7.7	Experimental observation of extreme events in a spatially extended microcavity laser	48
7.8	Correlation of spatiotemporal chaos characteristics and extreme events	49

Curriculum Vitae

Coulibaly Saliya

Université de Lille
Faculté de Science et Technologies
Département de Physique
Laboratoire PhLAM, Bât. P5-USTL
F-59655 Villeneuve d'Ascq cedex

Phone: +33(0)320336446
Fax: +33(0)320337020
Email: saliya.coulibaly@univ-lille1.fr
Homepage: <http://www.phlam.univ-lille1.fr>

Personal

- Born on January 20, 1977 in Kouassi-Daté Kro (RCI).
- French Citizen.

Education

- PhD in nonlinear Optics, University of Lille 1, title of the thesis: "Dissipative localized structures in optical parametric oscillators: convective vs. absolute instabilities and walk-off nonlinear effects", 2006.
- Master degree in Waves Propagation and properties of matter - University of Cocody (Ivory Coast)

Employment

- **Maître de Conférences** (Assistant Professor), University of Lille 1, since Sept. 2011.
- **ATER**, University of Lille 1, 09/2010–09/2011.
- **Postdoctoral position**, University of Lille 1, 06/2009–09/2010.
- **Postdoctoral position**, FCFM - University of Chile (Santiago), 04/2007–06/2009.

Research

Scientific production

- Peer review publications : 38
- Book chapter : 2
- Oral communications : 9

Partners

- Marcel Clerc [University of Chile (Santiago)]
- Mustapha Tlidi [Université Libre de Bruxelles]
- Sylvain Barbay [Centre de Nanosciences et de Nanotechnologies (Marcoussis)]
- Marc Wuilpart [University of Mons (Belgium)]

Projects

- Project ECOS-Sud C15E06 Lille–Valparaiso (Chile) [2016-2019]
Title: Study of formation of Chimera states in systems with local coupling.
- IAP Photonics@be of "The Belgian Science Policy Office" (Lille team)[2012-2017]
- ANR Blanc project OPTIROC (Lille team) [2012-2016]
Title: Optical Rogue Waves in Nonlinear Cavities.
- ANR international France-Chile COLORS (Lille team) [2011-2014]
Title: Controle des Structures Localisées et Rares en Optique.
- CONICYT-Chile Grant No. 3080041 [2007-2009]
Title: Oscillatory Localized domains in parametrically driven systems.

Training

- Postdocs supervision
 - Zheng LIU (*with Majid Taki*) [2014-2016]
 - Gaston TIOFACK (*with Majid Taki*) [2015-2017]
- PhD students
 - Mardia OUALI (*with Majid Taki*) [2, 3] : Defended on 13/12/2016
 - Lamyae DROUZI (*with Majid Taki*) [7]
- Ms degree students
 - Lamyae DROUZI (*with Majid Taki*)

Teaching

All my teachings are performed at the "UFR de Physique". They cover the three years of the undergraduate studies. The subjects concerned are mechanics, optics, vibratory phenomena and mathematical tools for physics. Since four years, I am in charge of the "Optics for biologists" teaching module.

Introduction

Introduction

This manuscript presents an overview of my research activities since the end of my PhD thesis. The following two words sum up these activities: *Dissipative structures*.

The concept of dissipative structures was introduced by I. Prigogine in the late 1960s to explain the process of structuring and spontaneous organization within systems far from the thermodynamic equilibrium. The basic idea was the following: contrary to the thermodynamics principle stating that irreversible processes usually move towards more disorder, self-organized and stable structures can arise from even more disordered systems [Nicolis and Prigogine, 1977]¹.

The authorship of the expression dissipative structure is undoubtedly attributed to Prigogine. However, the problematic of self-organization was previously posed in Schrödinger's *What's Life?* back in 1944 [Schrödinger, 1992]. Through this book Schrödinger discussed the following question: "How can the events in space and time which take place within the spatial boundary of a living organism be accounted for by physics and chemistry?". In its attempt to unify biology, physics and chemistry on a common basis, it is essentially the capacity of the living to defy the second principle of thermodynamics that is questioned [Schrödinger, 1992, Rossi et al., 2008]. Less than a decade later, Turing published his works showing how reaction-diffusion phenomenon of chemical species can generate spatial structuring [Turing, 1952], and suggest a link to biological patterns.

It is in this context that I. Prigogine has formulated the concept of dissipative structures providing a solution to this contradiction of living system: "create order from disorder" [Nicolis and Prigogine, 1977]. A few years later, H. Haken theorized the concept of *Synergetics* based on an approach similar to statistical physics to study transition from the disordered light of a lamp to the highly ordered light of a laser [Haken, 1978]. The main idea, consecrated by the elaboration of his widely admitted theory, is the link between self-organization and the breaking of symmetry, more specifically spontaneous symmetry breaking [Yates, 2012]. The symmetry invoked here refers to the spatial symmetry i.e. the homogeneous distribution of the system extension.

To study some problems of thermodynamic phase transition, Landau and Lifshitz [Landau and Lifshitz, 1940] have introduced the concept of symmetry-breaking from which, the *order parameter* concept is based. Behind this idea, Landau suggests that whenever a loss of symmetry takes place, a new thermodynamic parameter can be introduced such that its value is zero in the symmetric case. This order parameter can then be used to measure the amount of disorder in the broken symmetry state. An interesting feature in Landau's theory is that the order of the nonlinear expansion of the physical pertinent quantity² [Ginzburg and Landau, 1950, Binder, 1973, Devonshire, 1954] is defined by the type of transition.

¹http://www.nobelprize.org/nobel_prizes/chemistry/laureates/1977/prigogine-facts.html

²e.g. dipolar moment for magnetic material or superfluidity density for superconductor

This leads us to one of the crucial element needed for the emergence of order from disorder: nonlinearity. It is present in almost every area of modern science. It is that much linked to dissipative structures the latter has become a branch of what is now called nonlinear dynamics. As Turing pointed out, diffusion plays a key role in the symmetry breaking process. Beyond the diffusion phenomenon, here emphasis should put on the key role of all the spatial coupling processes. Hence, spatial symmetry breaking needs at least diffusion [Turing, 1952], diffraction [Newell and Moloney, 1992], dispersion (when by analogy time plays the role of the space e.g. in wave guide-based system) [Agrawal, 2013], local or global coupling in discrete system [Kaneko, 1986, Kuramoto, 1984]. The direct consequence of the underlying coupling phenomena is the selection of the characteristic length scale of the structures that could be supported by the considered system. Thus, the dimensions of the dissipative structures range from astronomic length scale (Jupiter's red spot) down to the nanoscale (scaffolding-induced stability of individual cells) [Scott et al., 2006]. The corresponding patterns are of such a variety that it would be futile to draw up an exhaustive list. However, among the most recurrent patterns reported in many fields of modern science such as biology, optics, chemistry, hydrodynamics and quantum physics, one has localized structures, square, stripe hexagonal patterns and vortices.

The general purpose of nonlinear physicists, be they use a stochastic or a deterministic approach, can be summarized into the following points:

- By mean of the known physical laws, find the set of nonlinear partial differential equations that describe the evolution of the system.
- Identify the symmetry breaking transition and describe the nature of the emerging patterns in the parameters space.

It is from this last point that the study of the dissipative structures have acquired its universal feature, which is essentially illustrated by the concept of instability. Indeed, any dynamical system undergoing a symmetry breaking implies an instability processes which can be addressed by the linear stability analysis recapitulated as follows. Generally speaking, the spatiotemporal evolution of a continuous system of n variables lumped together in the vector $\mathbf{u}(\mathbf{x}, t)$ is written as follows:

$$\partial_t \mathbf{u} = N(\mathbf{u}, \nabla, \alpha), \quad (1.1)$$

where N is a nonlinear function of $\mathbf{u}(\mathbf{x}, t)$, ∇ the spatial differential operator acting on \mathbf{u} and α the control parameter measuring the action of the external environment on the system.

Basically, the stability of a solution \mathbf{u}_0 is evaluated by setting $\mathbf{u} = \mathbf{u}_0 + \delta$. The linearization around \mathbf{u}_0 yield to the evolution of the perturbation δ

$$\partial_t \delta = \left. \frac{dN(\mathbf{u})}{d\mathbf{u}} \right|_{\mathbf{u}_0} \delta. \quad (1.2)$$

The system is said to be linearly stable if a perturbation decreases during the evolution and unstable otherwise. In case of neutral evolution—no decay nor amplification of the perturbation—the system is said to be linearly marginal. This case constitutes the transition point characterized by a specific value of the control parameter α . In addition, to determine the spatial length scales involved in the symmetry breaking, the decomposition of the perturbation into Fourier modes $\delta = \delta_q \exp(\mathbf{q} \cdot \mathbf{x})$ is the standard practice.

Next the linear stability is studied with respect to the modes q when acting upon the control parameter α . Even though it is a powerful tool to determine the length scales of the final dissipative structure, the linear stability analysis fails to describe the evolution beyond the critical point because of the diverging of the exponential growth. Therefore, to solve the fully nonlinear system, an approach is to introduce some order parameters and compute their evolution with respect to the distance from the critical point [Haken, 1978]. This approach is referred to in the literature as the weakly nonlinear approach and it is formally carried out by means of the *near-identity transformation* [Rand, 1994] method or the *multi-scale expansion* [Kevorkian and Cole, 1996]. In general, the form of the resulting order parameter equation is closely related to those of the eigenvalues of the linear operator corresponding to the considered solution, thus on the nature of the bifurcation. The universal aspect of these reduced equations comes from their only dependence on the nature of the bifurcation. They are referred to as amplitude equation in spatially extended systems or normal form otherwise. Such a *modus operandi*, starting with the linear stability analysis and ended with the amplitude equation is one of the three types of theoretical approaches generally applied to nonlinear dynamical systems. The second one, more qualitative, is based on topological techniques such as catastrophe theory or singularity theory to map the possible dynamical behaviors in the system [Kubicek and Marek, 1983]. The third approach consists of solving the full – microscopic – equations of motion of the considered system by means of computer simulations.

In practice, the latter approach is used in combination with one of the first two as verification and validation tool. However, the very existence of some sub-fields of nonlinear dynamical system theory is closely related to the development of numerical tools. When deterministic systems exhibit random evolutions, e.g. chaotic or spatiotemporal chaotic states are perfect examples. The theory of "few degrees of freedom" temporal chaos itself dates back from before the dissipative structures discipline [Cross and Hohenberg, 1993, Pismen, 2006]. The case of the works of E. Lorenz are the perfect illustration of the contingency between development of computer simulation and the rise of the theoretical understanding of the nature of chaos. In the same way, the spatiotemporal chaos theory developed to understand "how chaotic phenomena relate to dissipative structures" has taken advantage of the computer simulation approach.

Through these approaches, my research activities have focused on the mechanisms leading to the emergence of well localized structures in dissipative systems. Generally speaking, the first report on a well localized solution in an extended system goes back to the year 1844 by J.S. Russell [Russell, 1844]. A few decades later, they were mathematically understood as solutions of the class of integrable partial differential equations. Consequently, they form a family solutions resulting from a perfect balance between a broadening effect (diffraction or dispersion) and a material nonlinearity. While this condition effectively excluded the dissipative systems of those capable of supporting localized solutions, theoretical studies followed by experimental observations proved otherwise. Indeed, by a balance between the influx of energy and the losses in addition to the conditions stated previously, the extended dissipative systems are able to generate perfectly localized solutions and, unlike conservative localized structures, they are unique for each set of parameters.

It has been almost forty years since dissipative solitons are the object of particular attention in all fields of modern physics, as in biology, just to mention a few. It emerges from all the observations that the localized dissipative structures have a universal characteristic: they behave like particles. This property makes them dynamic objects with interaction capabilities whose potential applications are as diverse as the variety of systems in which they have been observed. Typical representatives example can be found in nonlinear optics, where one may mention the possibility of all optical switching and routing devices [Chen et al., 2012], opti-

cal data buffering [Firth, 2010], and optical logical gates [Ballarini et al., 2013]. Whether the prospect of technological applications technological scope is immediately obvious or not, the development of theoretical tools to understand the processes that support the emergence, evolution and interactions involving localized structures remains fundamental. These fundamental aspects, keeping in mind the experimental feasibility, are and will remain the main purpose of my research activities exposed here.

The manuscript is organized as follows: Part I covers the presentation of the dynamical systems that I have studied. For each case, after writing the equations of motion of the physical system the derivation of the reduced prototype model is considered. In addition, possible specific improvements of standard numerical integration methods is detailed when necessary. In part II, I present a selection of results of my contribution on exposing the domain of existence of dissipative localized structures, their interaction, and stability features. I conclude this report by current milestones on complex spatiotemporal dynamics in part III. Specifically, the emergence of spatiotemporal chaos in dissipative systems and its implications for some recent hot topics such as rogue waves dynamics is presented.



Mathematical modeling of physical systems

Abstract

Spontaneous and dramatic change in the spatial symmetry is inherent to self-organization or self-ordering in natural systems. From the beginning of this area of theoretical modern physics, the main challenge is the accuracy of the predictions. Addressing this challenge requires a good perception and identification of the underlying processes to determine the adequate physical law and fundamental principle that applies. Since the end of my thesis, I have studied a variety of systems. The aim of this part is to present an overview of these systems.

The first system is a vertically driven-damped chain of pendulum. The elementary constituent of this system is a pendulum with vertically oscillating pivot. Each pendulum of the chain is assumed to be elastically coupled to its nearest neighbor. The second system is a chain of spin submitted to an oscillating magnetic field. In this case, the elementary system is a spin animated by a precessional dynamic. It corresponds to a anisotropic ferromagnetic wire in the one dimensional case and the 2D version model corresponds to a ferromagnetic plane. The next system is a vertically shaken rectangular water channel.

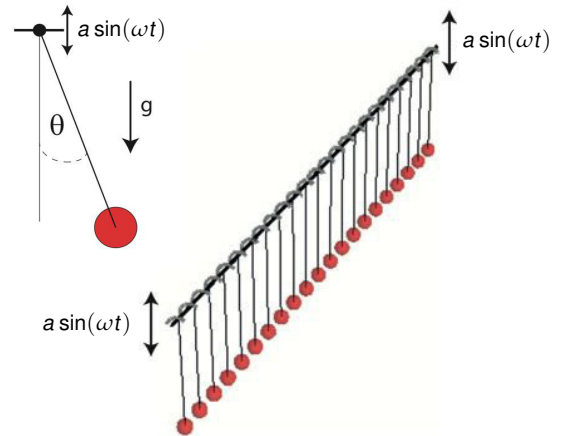
The aforementioned systems have in common the ability to exhibit parametric resonance when the driving is harmonically modulated. Therefore, they can be described by the same reduced model: the parametrically damped and driven nonlinear Schrödinger equation. The derivation of this equation starting from the microscopic equations is also considered.

In addition to parametrically driven systems, a large part of my activities is devoted to the pattern forming in optical systems. More specifically, I am interested on temporal instabilities on optical fiber-based waveguide. Two configurations are considered. In the first case, the propagation of the light pulse in an optical fiber is presented. After that, the modeling of a light circulating in a fiber with coupled ends is performed. The first case can be considered as a conservative system while the other is a dissipative one. The resulting models are the nonlinear Schrödinger equation and the Lugiato-Lefever equation, respectively. Before being named after Lugiato and Lefever in optics, this equation was referred as the driven and damped nonlinear Schrödinger equation.

The vertically driven and damped coupled chain of pendulum

The interest for the dynamics of coupled oscillator is a very old problem. The state of the art can be traced back to the proposition of Huygens [Huygens, 1669, Bennett et al., 2002] to use a set of two identical pendulum-watches to measure longitudes during sea navigation. Related phenomena include synchronization, quenching, phase locking, and amplitude death. All these phenomena are closely related to the nature of the coupling and also to the way that energy is injected in the system. In this chapter I consider the processes by which an energy storage parameter of a singly or multi-resonant system is harmonically modulated. Such a process known as parametric forcing, first studied by Faraday [Faraday, 1831] in the nineteenth century. Since then it has been shown to produce a large variety of dissipative structure in almost all the area of modern physics. A sketch of this physical system is given in Figure 2.1.

Figure 2.1: Schematic representation of a vertically driven chain of pendula: all pendulums are equally spaced by Δa and coupled with ideal spring and the horizontal rod oscillates vertically in time. For the sake of simplicity, a single pendulum is assumed to have a total mass m and a length L .



In this setup the deviation of the j -th pendulum of the chain experience the gravity (including the acceleration of the pivot) F_{gravity} , the elasticity due to neighborhood coupling F_{elastic} and the viscous friction $F_{\text{damping}} \propto \partial_t \theta_j$. Assuming the spacing much smaller than the individual pendula length L , then $F_{\text{elastic}} = -kL(\theta_{j+1} - 2\theta_j - \theta_{j-1})$. Since the displacement of the pivot is given by $a \sin(\omega t)$, the effective gravity reads $g \pm a\omega^2 \sin(\omega t)$, with the sign conveniently chosen depending on the origin of the date t . Hence, after Newton's second law the motion of the j -th pendulum of the chain is given by:

$$\frac{\partial^2 \theta_j}{\partial t^2} + 2\alpha \frac{\partial \theta_j}{\partial t} + \omega_0^2 [1 + 4\gamma \sin(\omega t)] \sin \theta_j - K(\theta_{j+1} - 2\theta_j - \theta_{j-1}) = 0, \quad (2.1)$$

where $\gamma = a\omega^2/(4\omega_0^2L)$, $K = k/m$ and α the damping parameter. This equation is the driven and damped version of the well-known Frenkel-Kontorova model. Hence, when the discreteness can be neglected the system can be described by the perturbed sine-Gordon [Braun and Kivshar, 2004] equation:

$$\frac{\partial^2\theta}{\partial t^2} + 2\alpha\frac{\partial\theta}{\partial t} + \omega_0^2[1 + 4\gamma\sin(\omega t)]\sin\theta - K\Delta a^2\frac{\partial^2\theta}{\partial x^2} = 0. \quad (2.2)$$

For a vanishing coupling and damping, the oscillators then obey to the Mathieu equation. In the $\omega - \gamma$ plane, this equation is known to have an infinite sequence of domains—the Arnold's tongues—in which the pendulum can acquire an undamped periodic motion around the vertical axis [Landau and Lifshitz, 1966]. These tongues are located at $\omega_n/\omega_0 = 2/n$ are increasingly narrower for higher values of n and for non vanishing damping the most visible one for small values of γ correspond to $n = 1$ also known as the 2:1 resonance. For small deviations, the following approximation $\sin\theta \sim \theta - \theta^3/6$ may apply. In practice, the small deviation regime corresponds to the situation where the damping and the driving strength are also small, says the quasi-reversible limit. It is also convenient to use the dimensionless form of Eq. (2.2) setting $t = T/\omega_0$, $\mu = \alpha/\omega_0$, $x = X\sqrt{K\Delta a^2/(2\omega_0^2)}$ and $\Omega = \omega/\omega_0$. Hence, in the quasi-reversible limit its follows:

$$\frac{\partial^2\theta}{\partial T^2} + 2\mu\frac{\partial\theta}{\partial T} + \theta - \frac{\theta^3}{6} + 4\gamma\sin(\Omega T)\theta - 2\frac{\partial^2\theta}{\partial X^2} = 0. \quad (2.3)$$

To explore the dynamical behavior of the system in the $\Omega - \gamma$ plane but close to the 2:1 resonance it is useful to introduce a detuning parameter such that $\Omega = 2(1 + \nu)$. In the quasi-reversible limit Eq. (2.3) is nothing but the harmonic oscillator perturbed with small damping, energy injection, weak coupling and anharmonicity. Consequently, one can introduce the following *ansatz*:

$$\theta(X, T) = A(X, T)e^{iT} + \bar{A}(X, T)e^{-iT} + W(A, \bar{A}, T). \quad (2.4)$$

In this *ansatz*, \bar{A} stands for the complex conjugate (c.c) of A and $W(A, \bar{A}, t)$ is a small correction term to the harmonic response ($W \ll A$) and we may also consider that $\partial_{TT}A \ll \partial_TA \ll A$ in addition to $\gamma \sim \mu \sim \nu \sim \partial_{XX} \ll 1$. Introducing (2.4) in (2.3) and collecting terms in $\{e^{iT}, e^{-iT}\}$ and their harmonics leads to:

$$\mathcal{L}W = \left(-2i\partial_TA - 2i\mu A + \frac{1}{2}|A|^2A + 2\partial_{XX}A + 2i\gamma\bar{A}e^{2ivT}\right)e^{iT} + \frac{1}{6}A^3e^{3iT} + 2i\gamma A e^{i(3+2\nu)T} + \text{c.c.}, \quad (2.5)$$

where the operator $\mathcal{L} = (\partial_{TT} + 1)$. The goal of the approach is then a proper evaluation of W . Let set g_{rhs} , the right hand side of Eq. (2.5). Hence, owing that $\mathcal{L}W = g_{\text{rhs}}$ is a linear equation in W , non-trivial solutions can be found if and only if the g_{rhs} is in the image of \mathcal{L} . This condition can be hold by the Fredholm's alternative¹ [Pismen, 2006] stating that the g_{rhs} is orthogonal to the Kernel of the adjoint operator \mathcal{L}^\dagger . To this end it is necessary to introduce an inner product of functions space. In the current case it reads:

$$\langle f, g \rangle = \frac{1}{2\pi} \int_{T_0}^{T_0+2\pi} \bar{f}(T) g(T) dT. \quad (2.6)$$

Here, it is straightforward to check that $\langle f, \mathcal{L}g \rangle = \langle \mathcal{L}^\dagger f, g \rangle$. That is, \mathcal{L} is a self-adjoint operator. Consequently, the elements of its Kernel are given by $\{e^{iT}, e^{-iT}\}$. This means that the result of any product that includes one of these elements and the operator \mathcal{L} or \mathcal{L}^\dagger is null. Hence, setting $\langle f | = e^{iT}$ and $|g \rangle = \mathcal{L}W = g_{\text{rhs}}$ the inner product gives:

¹This condition is also known as the solvability condition.

$$\partial_T B = -ivB - \mu B - i|B|^2 B - i\partial_{XX} B + \gamma \bar{B}, \quad (2.7)$$

where $A = 2Be^{ivT}$. Next, considering this latter result in Eq. (2.5) it follows:

$$W = - \left[\frac{1}{6} B^3 + i \frac{\gamma}{2} B \right] e^{3i(1+\nu)T}, \quad (2.8)$$

from which the *ansatz* can be rewritten as:

$$\theta(X, T) = 2B(X, T) e^{i(1+\nu)T} - \left[\frac{1}{6} B(X, T)^3 + i \frac{\gamma}{2} B(X, T) \right] e^{3i(1+\nu)T} + \text{c.c.} \quad (2.9)$$

Eq. (2.7) is the parametrically driven and damped nonlinear Schrödinger (PDNLS) equation [Barashenkov et al., 1991]. It is the prototype model highly used to describe parametrically forced system near to the quasi-reversible limit.

Ferromagnetic driven systems

As I mentioned in the introduction, one of the outstanding feature of the dissipative structures is that their characteristic length scale range from astronomic scale to nanoscale. Magnetic system by the characteristic length [Liu et al., 2005] of their interactions are very good candidates to observe micro and nanoscale dissipative structures. Dissipative structures of magnetization dynamics are widely used for information storage in magnetic materials. From theoretical point of view, two approaches are generally used to model the magnetization dynamics. The first one is based on writing the Heisenberg hamiltonian and the second one consists on energetic considerations. The former one is considered here.

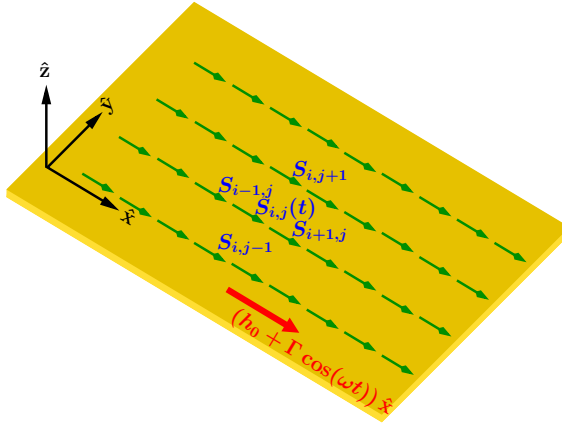


Figure 3.1: Schematic representation of a uniaxial anisotropic Heisenberg ferromagnetic layer. Small arrows represent the local magnetization ($\mathbf{S}_{i,j}$) and the large arrow stands for the external magnetic field.

Let's consider a two-dimensional anisotropic Heisenberg ferromagnetic layer formed by $N_x \times N_y$ spins or magnetic moment exposed to an external magnetic field, which is contained in the plane (x, y) and oriented in the direction $\hat{x} \equiv (1, 0, 0)$. Figure 3.1 depicts the setup of the considered system. Therefore, the Hamiltonian of the chain reads [Kittel, 1949, Zharnitsky et al., 1998]:

$$\mathcal{H} = \sum_{i,j}^N (-J_x \mathbf{S}_{i,j} \mathbf{S}_{i+1,j} - J_y \mathbf{S}_{i,j} \mathbf{S}_{i,j+1} + 2D(S_{i,j}^z)^2 - g\mu(S_{i,j}^x)H_x). \quad (3.1)$$

where $\{J_x, J_y\}$ are the exchange coupling constants, H_x and D account for the external magnetic field and the anisotropy energy, respectively. For the sake of simplicity, J_x and J_y will be taken identical in the following ($J_x = J_y = J$). When the quantum effects are small enough, the spin vectors $\mathbf{S}_{i,j}$ can be treated as classical spin or magnetic moment [Mikeska, 1978]. According to this latter assumption, the dynamics of the magnetic moment $\mathbf{S}_{i,j}$ is governed by $\dot{\mathbf{S}}_{i,j} = -\gamma \mathbf{S}_{i,j} \times (\partial \mathcal{H} / \partial \mathbf{S}_{i,j})$ [Kosevich et al., 1990], where γ is the gyromagnetic constant.

Hence, \mathbf{S}_i satisfies

$$\dot{\mathbf{S}}_{i,j} = -\gamma \mathbf{S}_{i,j} \times \left[-J(\mathbf{S}_{i-1,j} - 2\mathbf{S}_{i,j} + \mathbf{S}_{i+1,j}) - J(\mathbf{S}_{i,j-1} - 2\mathbf{S}_{i,j} + \mathbf{S}_{i,j+1}) + 4DS_{i,j}^z \hat{z} - g\mu H_x \hat{x} + 4J\mathbf{S}_{i,j} \right]. \quad (3.2)$$

Thus, taking $\mathbf{S}_{i,j}(t) \rightarrow \mathbf{S}(\mathbf{r}, t)$, where $\mathbf{r}(x, y)$ accounts for the coordinates in the plane and $J\gamma(\mathbf{S}_{i+1,j} - 2\mathbf{S}_{i,j} + \mathbf{S}_{i-1,j}) + J\gamma(\mathbf{S}_{i,j+1} - 2\mathbf{S}_{i,j} + \mathbf{S}_{i,j-1}) \rightarrow l_{\text{ex}}^2 \nabla_{\perp}^2 \mathbf{S}$, where l_{ex} denotes the characteristic interaction length and ∇_{\perp}^2 is the Laplacian operator in the new transversal coordinates ($\nabla_{\perp}^2 \equiv \partial_{xx} + \partial_{yy}$). The exchange length can be interpreted as the length below which atomic exchange interactions dominate typical magnetostatic fields. It also determines the thickness of soft-magnetic films above which the 2D magnetization dynamics assumed here fails [Liu et al., 2005].

Moreover, introducing phenomenologically the Gilbert damping, the motion of the magnetization field is governed by the well-known Landau-Lifshitz-Gilbert (LLG) equation:

$$\partial_{\tau} \mathbf{m} = -\mathbf{m} \times \left[l_{\text{ex}} \nabla_{\perp}^2 \mathbf{m} - \beta(\mathbf{m} \cdot \hat{z}) \hat{z} + \mathbf{h}_e - \alpha \partial_{\tau} \mathbf{m} \right], \quad (3.3)$$

where $\mathbf{m} = m_x \hat{x} + m_y \hat{y} + m_z \hat{z}$ stands for the unit vector of the magnetization; we have also introduce the following normalization $\{\tau \rightarrow \gamma M_s t, \beta \rightarrow 4D/\gamma, \mathbf{h}_e \rightarrow g\mu \mathbf{H}/\gamma M_s\}$ with M_s the magnetization of saturation defined as $\mathbf{m} = \mathbf{S}/M_s$; where $\beta > 0$ is the anisotropy constant (easy-plane magnetization), and α the damping parameter. This parameter for several types of material is small. When the magnetic field is time-dependent, the above model (3.3) is a time reversible system perturbed with injection and dissipation of energy. Hence, as far as these perturbations remain small the system can be consider in the quasi-reversible limit. Considering the external magnetic field along the \hat{x} -axis such that $\mathbf{h}_e = h(t)\hat{x}$, the equilibrium magnetization is parallel to the applied external field: $\mathbf{m}(\mathbf{r}, t) = (1, 0, 0)$. Then, taking advantage of the unitary norm of the local magnetization, it is convenient to write:

$$\mathbf{m} = \sqrt{1 - m_{\perp}^2} \hat{x} + \mathbf{m}_{\perp}(\mathbf{r}, t), \quad (3.4)$$

where $m_{\perp} = \sqrt{m_y^2 + m_z^2}$ is the component of the magnetization perpendicular to the easy-plane. Recalling the quasi-reversible limit, m_{\perp} should be smaller than 1. Therefore, the following approximation $\mathbf{m} \simeq (1 - m_{\perp}^2/2) \hat{x} + \mathbf{m}_{\perp}(\mathbf{r}, t)$ can be used in the cartesian projection of Eq. (3.4). Neglecting the nonlinear term higher than $O(m_y^3, m_y^2 m_z, m_z^3, m_y m_z^2)$ and those including a spatial derivative the precession dynamics is model by

$$\dot{m}_y = -(\beta + H) m_z - \alpha H m_y + l_{\text{ex}}^2 \nabla_{\perp}^2 m_z - \beta \frac{m_y^2 + m_z^2}{2} m_z, \quad (3.5a)$$

$$\dot{m}_z = H m_y - \alpha(\beta + H) m_z - l_{\text{ex}}^2 \nabla_{\perp}^2 m_y. \quad (3.5b)$$

Let's have a quick look on the case of uncoupled magnetic domains (all the spatial derivative are null) with constant external applied field. Extracting m_y in Eq. (3.5b) and replacing it in Eq. (3.5a) with respect to the time and replacing the term \dot{m}_z in equation (3.5a) after some algebra it follows at the leading order¹:

$$\dot{m}_z = -H_0(\beta + H_0^2) m_z - \alpha(\beta + 2H_0) \dot{m}_z + \frac{\beta}{2H_0} (\dot{m}_z^2 + H_0 m_z^2) m_z. \quad (3.6)$$

¹This is equivalent to consider that operators, variables, and parameter scale as $\alpha \sim m_y^2 \sim m_z^2 \ll 1$ and $\partial_t \sim H_0 \sim \beta \sim$ of order of $O(1)$.

This equation is the analogue of a nonlinear forced and damped oscillator with natural frequency $\omega_0 = \sqrt{H_0(\beta + H_0)}$. Now back to the full set of Eqs. (3.5) with the external magnetic field composed of constant and periodic terms, the resulting setup can be consider in the parametric forcing regime : $H = H_0 + h_1(\tau) = H_0 + \Gamma \sin[2\omega_0(1 + \nu)\tau]$ with $\nu \ll 1$. As for the case of the driven chain of pendulum, the response of the system can be grasped by introducing:

$$\begin{pmatrix} m_x \\ m_y \end{pmatrix} = A(\mathbf{r}, \tau) e^{i\omega_0\tau} \begin{pmatrix} \sqrt{H_0 + \beta} \\ -i\sqrt{H_0} \end{pmatrix} + \text{c.c.} + \mathbf{W}. \quad (3.7)$$

Hence, using the scaling $\Gamma \sim \alpha \sim \nu \sim \nabla_{\perp}^2 \ll 1$ together with $\partial_{\tau\tau}A \ll \partial_{\tau}A \ll A$ it comes at the leading order:

$$\begin{aligned} \mathcal{L}\mathbf{W} &= \partial_{\tau}A \begin{pmatrix} \sqrt{H_0 + \beta} \\ -i\sqrt{H_0} \end{pmatrix} e^{i\omega_0\tau} + (l_{\text{ex}}^2 \nabla_{\perp}^2 - i\alpha\omega_0)A \begin{pmatrix} i\sqrt{H_0} \\ \sqrt{H_0 + \beta} \end{pmatrix} e^{i\omega_0\tau} \\ &\quad - \frac{\Gamma}{2}\bar{A} \begin{pmatrix} -i\sqrt{H_0} \\ \sqrt{H_0 + \beta} \end{pmatrix} e^{2i\omega_0\nu\tau} e^{i\omega_0\tau} \\ &\quad + i\frac{\beta}{2}\sqrt{H_0}(4H_0 + \beta)|A|^2 A \begin{pmatrix} 1 \\ 0 \end{pmatrix} e^{i\omega_0\tau} + i\frac{\beta^2}{2}\sqrt{H_0}A^3 \begin{pmatrix} 1 \\ 0 \end{pmatrix} e^{3i\omega_0\tau} + \text{c.c.} \end{aligned} \quad (3.8)$$

In this relation, the linear operator \mathcal{L} and its adjoint \mathcal{L}^{\dagger} are given by

$$\mathcal{L} = \begin{pmatrix} \partial_{\tau} & H_0 + \beta \\ -H_0 & \partial_{\tau} \end{pmatrix} \quad \text{and} \quad \mathcal{L}^{\dagger} = \begin{pmatrix} -\partial_{\tau} & -H_0 \\ H_0 + \beta & -\partial_{\tau} \end{pmatrix}. \quad (3.9)$$

Then, the elements of the Kernel of \mathcal{L}^{\dagger} are $\{e^{i\omega_0\tau}\mathbf{v}, e^{-i\omega_0\tau}\bar{\mathbf{v}}\}$ with $\mathbf{v} = (\sqrt{H_0}, -i\sqrt{H_0 + \beta})^T$ and the inner product is defined as follows:

$$\langle \mathbf{f}, \mathbf{g} \rangle = \frac{\omega_0}{2\pi} \int_{\tau_0}^{\tau_0 + \omega_0/2\pi} \bar{\mathbf{f}}(\tau) \cdot \mathbf{g}(\tau) d\tau. \quad (3.10)$$

where the symbol \cdot denotes the inner product of vectors with complex components i.e. the dot product of \mathbb{C}^2 , and $\bar{\mathbf{f}}$ is the complex conjugate of the vector \mathbf{f} . The amplitude of $m_z(z, t)$ satisfies

$$2\omega_0\partial_{\tau}A = -i\frac{\beta(\omega_0^2 + 3H_0^2)}{2}|A|^2A - i(\beta + 2H_0)l_{\text{ex}}^2\nabla_{\perp}^2A - \alpha\omega_0(\beta + 2H_0)A + \frac{\beta\Gamma}{2}\bar{A}e^{2i\nu\omega_0\tau}. \quad (3.11)$$

Finally, the 2D version of equation Eq. (2.7) is found after setting

$$B = \sqrt{\frac{\beta(\omega_0^2 + 3H_0^2)}{4\omega_0^2}} A e^{-i\nu\omega_0\tau}, \quad (3.12a)$$

$$(X, Y) = \sqrt{\frac{2\omega_0^2}{(\beta + 2H_0)}} \begin{pmatrix} x \\ y \end{pmatrix}, \quad (3.12b)$$

$$\mu = \frac{\alpha(\beta + 2H_0)}{(2\omega_0)}, \quad (3.12c)$$

$$\gamma = \frac{\Gamma\beta}{4\omega_0^2}, \quad (3.12d)$$

$$T = \omega_0\tau. \quad (3.12e)$$

Notice that 1D equivalent of Eq. (3.11) can be derive in the same way considering an easy plane ferromagnetic wire.

The vertically driven rectangular water channel

The history of the parametric instability began with the Faraday experiments in which a liquid was driven by vertical harmonic oscillations. Since then, dynamics of standing waves produced by such a forcing is still extensively studied. Elsewhere, these studies have played a crucial role in the experimental evidence of a large variety of dissipative structures. From the theoretical point of view, mathematical description of Faraday experimental setup have been started with the seminal paper of Benjamin and Ursell [Benjamin and Ursell, 1954] where they analyzed Faraday waves of an irrotational inviscid fluid. The main result of this analysis is providing an interpretation of the linear behavior of the inviscid fluid as a Mathieu oscillator. Later, an extension of this to the damped version for viscous fluid have been provided [Cerdeira and Tirapegui, 1998]. Immediately afterwards the observation of non-propagative hydrodynamic soliton [Wu et al., 1984], many theoretical studies have attempted to model the contribution of the nonlinearities [Miles, 1984, Larraza and Putterman, 1984, Zhang and Vinals, 1997]. With the same goal to describe the evolution of the free surface of a fluid in a closed basin as depicted by Figure 4.1, many strategies have been used [Gordillo, 2012]. Remarkably, many of these approach have produced similar results. Only two of the main strategies are recalled here. The first one

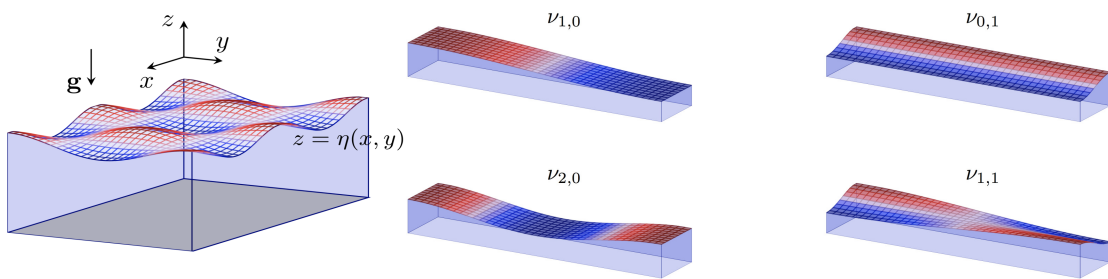


Figure 4.1: Schematic representation of the water surface elevation to be studied. The ν_{ij} are some of the canonical modes ν_{ij} supported by a rectangular basin of length l , breadth w , and filled with a fluid layer of depth d [Gordillo, 2012].

proposed by Larraza and Putterman [Larraza and Putterman, 1984] consists on the theoretical description of the system depicted by Figure 4.1. It starts by writing the equations for the bulk (Laplace equation), the impermeability condition for the walls and the bottom and the kinematic and dynamic boundary condition at the free-surface (Bernoulli principal) for an ideal irrotational inviscid fluid. With the notations introduced in Figure 4.1 it results the following

set of equations:

$$\nabla^2 \Phi = 0, \quad \text{in } V \quad (4.1a)$$

$$\nabla \Phi \cdot \mathbf{n} = 0, \quad \text{at } \partial C \quad (4.1b)$$

$$\partial_z \Phi - \partial_t \eta - \nabla_{\perp} \eta \cdot \nabla_{\perp} \Phi = 0, \quad (4.1c)$$

$$\partial_t \Phi + \frac{1}{2} (\nabla \Phi)^2 + g(1 - f(t))\eta - \frac{\gamma}{\rho} \kappa = 0. \quad \text{at } z = \eta(\mathbf{x}) \quad (4.1d)$$

Next this set of equations is directly expanded up to the third order.¹ The second approach proposed by Miles invokes the average Laplacian method (see e.g. [Miles, 1984] for further details). In both cases, it appears that the amplitude equation for the surface elevation is closely related to the canonical modes v_{ij} (i and $j \in \mathbb{R}$) sketched in Figure 4.1. According to the experimental observations [Wu et al., 1984], the dominant mode corresponds to v_{01} . The expression of the surface elevation in this case is given by [Umeki, 1991, Denardo et al., 1990]:

$$\eta(x, y, t) = [\eta_1(x, t) e^{i\omega t} + \text{c.c.}] \cos(\pi y/w) + [\eta_2(x, t) e^{2i\omega t} + \text{c.c.} + \eta_2^{(0)}(x, t)] \cos(2\pi y/w). \quad (4.2)$$

Here ω stands for the half of the driving frequency. In the following, the acceleration of this driving is taken in the quasi-reversible limit and $(\omega - \omega_1)/\omega \ll 1$ where $\omega_1 = \sqrt{gkT}$, with $k = \pi/w$ and $T = \tanh(kd)$, is the frequency related to the transverse mode. Under these considerations, η_1 represents the slowly varying (in both time and space) amplitude of the dominant mode v_{01} . Hence, η_2 and $\eta_2^{(0)}$ are small compared to η_1 . Following the approach of Larraza and Putterman, at the leading order, the solvability condition gives²

$$2i\omega \partial_t \eta_1 - c^2 \partial_x^2 \eta_1 - (\omega^2 - \omega_1^2 - 2i\omega\alpha) \eta_1 - 2i\omega^2 \Gamma \bar{\eta}_1 - \delta \omega^2 k^2 |\eta_1|^2 \eta_1 = 0, \quad (4.3)$$

where

$$c^2 = \frac{g}{2k} [T + kd(1 - T^2)], \quad (4.4a)$$

$$\delta = \frac{1}{8} (6T^4 - 5T^2 + 16 - 9T^{-2}). \quad (4.4b)$$

After introducing

$$T = \omega t, \quad (4.5a)$$

$$X = \frac{x}{c\omega}, \quad (4.5b)$$

$$\nu = \frac{\omega^2 - \omega_1^2}{2\omega^2}, \quad (4.5c)$$

$$\mu = \frac{\alpha}{\omega}, \quad \text{and} \quad (4.5d)$$

$$A = k \sqrt{2\delta} \eta_1 \quad (4.5e)$$

one recovers the Eq. (2.7).

¹Notice that in their original work Larraza and Putterman did not treat the periodic forcing.

²The damping parameter α has been introduced through $\partial_t \rightarrow \partial_t + \alpha$. This suppose that the damping effects are coming only from the kinematic viscosity. However, in [theseLeo] other sources of the dissipation have been discussed in detail.

Propagation in fiber optics

The three examples presented before are illustrative for the universality of the processes underlying the dynamics of the dissipative structures. Specifically, parametric forcing have played a crucial role on the understanding of solitons being dissipative or conservative. However, there is an area where solitons rapidly became not only laboratory curiosities but also of many technological interests: said nonlinear optics. Beyond solitons, the development of nonlinear optics in the following the mastery of lasers have greatly contributed to the experimental and theoretical studies of self-organization. In this history, nonlinear fibers optics is one of the most important achievement. In particular the availability of low-loss fibers at the beginning of seventies was the start of this revolution. In this section the fundamental concepts behind the modeling of the light-matter interactions in optical fibers are presented.

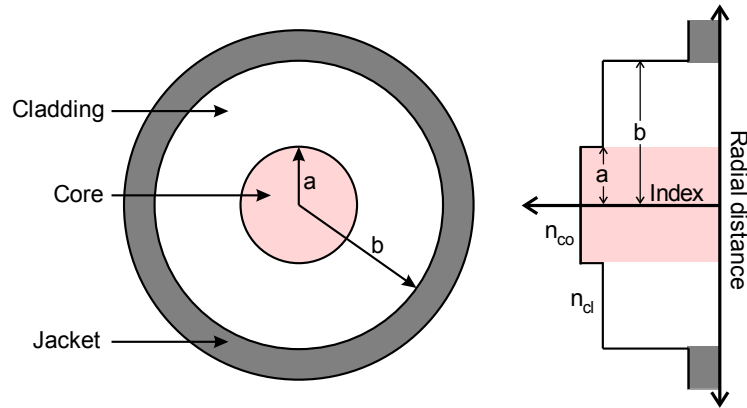


Figure 5.1: Sketch of refractive index profile and the cross-sectional diagram of a step-index fibre.

Generally speaking, a successful propagation in an optical fiber consists on guiding a light wave inside a central glass core with a refractive index n_{co} . This core is surrounded by a cladding whose refractive index n_{cl} is slightly lower than n_{co} allows the necessary total internal reflexion. Fibers with such a structure (see Figure 5.1) are referred to as step-index fibers, while graded-index fibers are characterized by a gradual decrease of the index from the core to the cladding [Agrawal, 2013]. The approach presented here is based on the propagation in step-index fibre. The evolution of the electric along the fiber is given by:

$$\nabla^2 \mathbf{E}(\mathbf{r}, t) - \frac{1}{c^2} \frac{\partial^2 \mathbf{E}(\mathbf{r}, t)}{\partial t^2} = \mu_0 \frac{\partial^2 \mathbf{P}_l(\mathbf{r}, t)}{\partial t^2} + \mu_0 \frac{\partial^2 \mathbf{P}_{nl}(\mathbf{r}, t)}{\partial t^2}, \quad (5.1)$$

where $c = (\mu_0 \epsilon_0)^{-1/2}$ is the speed of the light in vacuum. μ_0 and ϵ_0 are the vacuum permeability and the permittivity, respectively. ∇^2 is the Laplacian associated to $\mathbf{r} = x\hat{x} + y\hat{y} + z\hat{z}$. \mathbf{P}_l and

\mathbf{P}_{nl} are the linear and nonlinear polarization vectors, respectively. Since an optical fiber has cylindrical symmetry, and so it is a centro-symmetric medium, the leading nonlinearity is cubic. Hence,

$$\mathbf{P}_l(\mathbf{r}, t) = \epsilon_0 \int_{-\infty}^{\infty} \chi^{(1)}(t-t') \mathbf{E}(\mathbf{r}, t') dt' \quad (5.2a)$$

and

$$\mathbf{P}_{nl}(\mathbf{r}, t) = \epsilon_0 \iiint_{-\infty}^{\infty} \chi^{(3)}(t-t_1, t-t_2, t-t_3) (\mathbf{E}(\mathbf{r}, t_1) \cdot \mathbf{E}(\mathbf{r}, t_2)) \mathbf{E}(\mathbf{r}, t_3) dt_1 dt_2 dt_3 \quad (5.2b)$$

In general, the contributions of the nonlinear part in the total refractive index is small. Consequently \mathbf{P}_{nl} can be treated as a small perturbation to \mathbf{P}_l . For pulses larger enough (duration not shorter than 100 fs), the spectral width $\Delta\omega$ and the central frequency are such that $\Delta\omega/\omega_0 \ll 1$ (quasi-monochromatic field). Under these assumptions and considering a maintained polarization of the electric field, the slowly varying envelope approximation can be used:

$$\mathbf{E}(\mathbf{r}, t) = \frac{1}{2} \hat{x} [E(\mathbf{r}, t) e^{i\omega_0 t} + \text{c.c.}]. \quad (5.3)$$

Therefore, the polarizations can be written in the same form as:

$$\mathbf{P}_l(\mathbf{r}, t) = \frac{1}{2} \hat{x} [P_l(\mathbf{r}, t) e^{i\omega_0 t} + \text{c.c.}]. \quad (5.4a)$$

$$\mathbf{P}_{nl}(\mathbf{r}, t) = \frac{1}{2} \hat{x} [P_{nl}(\mathbf{r}, t) e^{i\omega_0 t} + \text{c.c.}]. \quad (5.4b)$$

Inserting (5.3) in (5.6) leads to:

$$P_l(\mathbf{r}, t) = \epsilon_0 \int_{-\infty}^{\infty} \chi^{(1)}(t-t') E(\mathbf{r}, t') e^{-i\omega(t-t')} dt'. \quad (5.5)$$

Next assuming that the nonlinear response is instantaneous, the time dependence of $\chi^{(3)}$ is given by the product of three delta function of the form $\delta(t-t_i)$. That is, the nonlinear polarization reads $\mathbf{P}_{nl}(\mathbf{r}, t) = \epsilon_0 \chi^{(3)} |\mathbf{E}(\mathbf{r}, t)|^2 \mathbf{E}(\mathbf{r}, t)$. Substituting (5.3) in (5.4b) and keeping only resonant terms the nonlinear polarization can be written as follows:

$$P_{nl}(\mathbf{r}, t) = \epsilon_0 \epsilon_{nl} E(\mathbf{r}, t), \quad (5.6)$$

where the nonlinear dielectric constant $\epsilon_{nl} \equiv \frac{3}{4} \chi^{(3)} |E(\mathbf{r}, t)|^2$ can be assumed constant in the limit of validity of the slowly varying envelope approximation. With this assumption, Eq. (5.1) in the Fourier space can be written in the form:

$$\nabla^2 \tilde{E} - \epsilon(\omega) k_0^2 \tilde{E} = 0, \quad (5.7)$$

where $k_0 = \omega/c$, $\epsilon(\omega) = 1 + \tilde{\chi}^{(1)}(\omega) + \epsilon_{nl}$, and

$$\tilde{E}(\mathbf{r}, \omega - \omega_0) = \frac{1}{2\pi} \int_{-\infty}^{\infty} E(\mathbf{r}, t) e^{i(\omega - \omega_0)t} dt. \quad (5.8)$$

According to the assumptions made above the effective dielectric constant can be written

$$\epsilon(\omega) = n(\omega)^2 + n(\omega) \Delta n, \quad (5.9)$$

with $\Delta n = n_2(\omega) |E|^2 + i \frac{\alpha_f}{2k_0}$ such that $\Delta n \ll n(\omega)$. In practice, when $V = k_0 a \sqrt{n_{co}^2 - n_{cl}^2} < 2.405$, the transverse distribution of the intensity profile is very closed to the TEM_{00} mode. Then, the solution of (5.7) can be obtained introducing

$$\tilde{E}(\mathbf{r}, \omega - \omega_0) = F(x, y) \tilde{A}_0(z, \omega - \omega_0) e^{i\beta_0 z}, \quad (5.10)$$

where $F(x, y)$, $\tilde{A}_0(z, \omega - \omega_0)$, and β_0 are the transverse profile, the slowly longitudinal envelope, and the propagation constant, respectively. It results from the slowly varying envelope approximation that $\partial_z^2 \tilde{A}_0 \ll \partial_z \tilde{A}_0 \ll \tilde{A}_0$. Therefore F , \tilde{A}_0 and β_0 are solutions of the following set of eigenvalue problems:

$$\left(\frac{\partial^2}{\partial x^2} + \frac{\partial^2}{\partial y^2} \right) F - [n^2 k_0^2 + 2nk_0^2 \Delta n - \tilde{\beta}^2] F = 0, \quad (5.11a)$$

$$2i\beta_0 \frac{\partial \tilde{A}_0}{\partial z} + (\tilde{\beta}^2 - \beta_0^2) \tilde{A}_0 = 0 \quad (5.11b)$$

where $\tilde{\beta}$ to be determined, is the eigenvalue for both transverse and longitudinal operators. Setting $\tilde{\beta} = \beta(\omega) + \Delta\beta$ such that $\Delta\beta \sim \Delta n \ll \beta(\omega)$, the leading order gives [Agrawal, 2013]:

$$F(x, y) \approx e^{-\frac{x^2+y^2}{w^2}}, \quad (5.12)$$

where $w/a \approx 0.65 + 1.619V^{-3/2} + 2.879V^{-6}$. As far as $V < 2.405$, the single propagation mode is not affected by Δn . Next $\Delta\beta$ is found to be:

$$\Delta\beta = \frac{k_0 \iint_{-\infty}^{\infty} \Delta n |F(x, y)|^2 dx dy}{\iint_{-\infty}^{\infty} |F(x, y)|^2 dx dy}. \quad (5.13)$$

Making use of the approximation $\tilde{\beta}^2 - \beta_0^2 \approx 2\beta_0(\tilde{\beta} - \beta_0)$, Eq. (5.11b) becomes:

$$\frac{\partial \tilde{A}_0}{\partial z} = i[\beta(\omega) + \Delta\beta - \beta_0] \tilde{A}_0. \quad (5.14)$$

At this point, it is worthy to note that $\beta(\omega) = n(\omega) \frac{\omega}{c}$ manifests the chromatic dispersion of the fiber. In practice, this dependence is given by a Taylor expansion of the dispersion relation around the carrier frequency ω_0 as:

$$\beta(\omega) = \beta_0 + \sum_{m=1}^{\infty} \frac{\beta_m}{m!} (\omega - \omega_0)^m, \quad (5.15)$$

with $\beta_m = \left. \frac{d^m \beta}{d\omega^m} \right|_{\omega=\omega_0}$ ($m = 0, 1, 2, \dots$). Finally the equation of the propagation in the Fourier space is given by:

$$\frac{\partial \tilde{A}_0}{\partial z} = i \left[\beta_1 (\omega - \omega_0) + \sum_{m=2}^{\infty} \frac{\beta_m}{m!} (\omega - \omega_0)^m + \Delta\beta \right] \tilde{A}_0 \quad (5.16)$$

which, going back to the time domain can be written in the form:

$$\frac{\partial A_0}{\partial z} = \beta_1 \frac{\partial A_0}{\partial t} + i \sum_{m=2}^{\infty} (-i)^m \frac{\beta_m}{m!} \frac{\partial^m A_0}{\partial t^m} - \frac{\alpha_f}{2} A_0 + i \frac{k_0 n_2 \iint_{-\infty}^{\infty} |F(x, y)|^4 dx dy}{\iint_{-\infty}^{\infty} |F(x, y)|^2 dx dy} |A_0|^2 A_0. \quad (5.17)$$

In this equation, A_0 is in units of electric field (V/m). However, for practical reasons it is convenient to have a direct link with the optical power. Therefore, introducing

$$\begin{aligned} A_{\text{eff}} &= \frac{\left(\iint_{-\infty}^{\infty} |F(x, y)|^2 dx dy \right)^2}{\iint_{-\infty}^{\infty} |F(x, y)|^4 dx dy}, \\ |A|^2 &= \frac{1}{2} \epsilon_0 n c |A_0|^2 \iint_{-\infty}^{\infty} |F(x, y)|^2 dx dy, \\ \gamma &= \frac{2\omega_0 n_2}{\epsilon_0 n c^2 A_{\text{eff}}}, \quad \text{and} \\ T &= t - \beta_1 z, \end{aligned}$$

(5.1) can be written in the form of the generalized nonlinear Schrödinger (NLS) equation:

$$\frac{\partial A}{\partial z} = -\frac{\alpha}{2}A + i \sum_{m=2}^{\infty} (-i)^m \frac{\beta_m}{m!} \frac{\partial^m A}{\partial T^m} + i\gamma |A|^2 A. \quad (5.19)$$

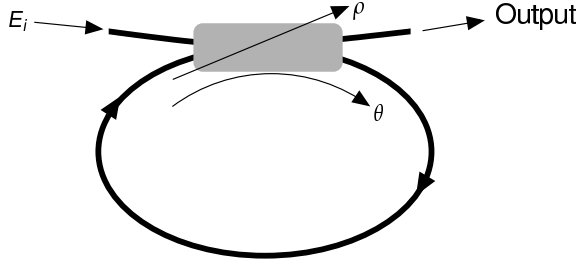


Figure 5.2: Sketch of an optical fiber ring resonator. The ends of the fiber are lumped together with a coupler (in gray) with intensity transmission θ and reflexion ρ .

By coupling the ends of an optical fiber, the resulting passive resonator is modeled by considering Eq. (5.19) together with some adequate boundary conditions. Hence, a fiber ring cavity, as depicted in Figure 5.2, can be analytically described as follows¹:

$$\partial_z A^{(j)}(z, T) = -\frac{\alpha}{2}A^{(j)}(z, T) - i\frac{\beta_2}{2} \frac{\partial^2 A^{(j)}(z, T)}{\partial T^2} + i\gamma |A^{(j)}(z, T)|^2 A^{(j)}(z, T), \quad (5.20a)$$

$$A^{(j+1)}(0, T) = \sqrt{\theta}E_i(T) + \sqrt{\rho}A^{(j)}(L, T) \exp(-i\Phi_0), \quad (5.20b)$$

where Φ_0 is the linear phase accumulated after a round trip. This set of equations, is referred to as the Ikeda map [Ikeda, 1979] or full map equations. From the analytical point of view, except for the linear stability analysis, it is a hard task to study nonlinear evolution of such a system directly via Eqs. (5.20). When a light pulse with peak power P_0 and duration T_0 is injected into the fiber, one can define the dispersion length $L_D = \sqrt{T_0/|\beta_2|}$ and the nonlinear length $L_{NL} = (\gamma P_0)^{-1}$. Hence, for a propagation length L much smaller than L_D and L_{NL} the pulse can be considered unaffected by the dispersion effects (e.g., temporal spreading) and the nonlinear effects (e.g., self-phase modulation), respectively. In this case, if in addition the finesse \mathcal{F} is high enough $\Delta\omega \ll \omega_{FSR}$, the mean-field approximation can be used to describe the full map equations. Consequently, after one roundtrip the solution of (5.20a) can be written in the form:

$$\begin{aligned} A^{(j)}(L, T) &\approx A^{(j)}(0, T) + L \left. \frac{\partial A^{(j)}(0, T)}{\partial z} \right|_{z=0} \\ &\approx \left[1 - \frac{\alpha L}{2} - i\frac{\beta_2 L}{2} \frac{\partial^2}{\partial T^2} + i\gamma L |A^{(j)}(0, T)|^2 \right] A^{(j)}(0, T). \end{aligned} \quad (5.21a)$$

For a resonant pumping, the acquired phase after a roundtrip is $2k\pi$ where the integer k labels the cavity resonances. Then, the distance to the closest cavity resonance is measured introducing $\delta = 2k\pi - \Phi_0$. Assuming $\delta \sim \theta \ll 1$, the term $\sqrt{\rho} \exp(-i\Phi_0)$ in (5.21a) can be written in the form:

$$\sqrt{\rho} \exp(-i\Phi_0) = \sqrt{1-\theta} \exp(-i\Phi_0) \approx \left(1 - \frac{\theta}{2}\right)(1 - i\delta) \approx 1 - \frac{\theta}{2} - i\delta.$$

Using this approximation after inserting (5.21a) in (5.20b) leads to:

$$A^{(j+1)}(0, T) \approx \sqrt{\theta}E_i(T) + \left[1 - \frac{\theta}{2} - \frac{\alpha L}{2} - i\delta - i\frac{\beta_2 L}{2} \frac{\partial^2}{\partial T^2} + i\gamma L |A^{(j)}(0, T)|^2 \right] A^{(j)}(0, T). \quad (5.22)$$

¹Without loss of generality, we take into account only the group velocity dispersion β_2 .

From this equation, one can easily identify the quantity that measures the change in the temporal profile from one roundtrip to another at the coupler as $A^{(j+1)}(0, T) - A^{(j)}(0, T) \approx t_R \partial_{t'} A(t', T)$ with $t' = jt_R$. Finally setting:

$$S = E_i \sqrt{\gamma \theta L}, \quad (5.23a)$$

$$\psi = A \sqrt{\gamma L}, \quad (5.23b)$$

$$t = \frac{t'}{t_R}, \quad (5.23c)$$

$$\tau = T \sqrt{\frac{2}{|\beta_2 L|}}, \quad (5.23d)$$

$$\alpha = \frac{\theta + \alpha_f L}{2}, \quad (5.23e)$$

$$\eta = \text{sgn}(\beta_2) = \pm 1, \quad (5.23f)$$

the mean-field evolution is given by the Lugiato-Lefever model:

$$\frac{\partial \psi}{\partial t} = S - (\alpha + i\delta) \psi + i |\psi|^2 \psi - i\eta \frac{\partial^2 \psi}{\partial \tau^2}. \quad (5.24)$$

It is the prototype mean field model for the passive Kerr resonators [Grelu, 2015]. Note that, before laser systems, Eq. (5.24) has been derived in early reports to describe the plasma driven by a radio frequency field [Morales and Lee, 1974, Nozaki and Bekki, 1984] and the condensate in the presence of an applied ac field [Kaup and Newell, 1978].



Contribution to the study of dissipative localized
structures

Abstract

In this part of the manuscript I present a selection of some milestone of my research activities on the field covered by the different systems described in the previous part. There is no particular motivations of their choice and no chronological link neither. It is just an overview and other choice may be also relevant since many of these works are connected.

I will begin with my contribution on the theoretical prediction of the interaction of parametrically excited dissipative localized structures (LS) in one dimensional extension. As I mentioned in the introductory part, dissipative localized structures can be understood as macroscopical particles. Owing to, they may be described by a family of continuous parameters such as their location, charge, width, just to mention a few. Particles are also known to interact. That is, solitons are also expected to do so. The problem of interaction of localized structures has begun with the born theory of soliton itself [Zabusky and Kruskal, 1965] and keeps being of great interest. In the context of parametrically driven systems, many experimental works have reported such an interaction. Similar behavior of particles such as attraction or repulsion has been observed and studied. In general, it is the phase of the soliton that plays the role of the charge. Our contribution to this area has provided a theoretical background to this interaction. The calculations were performed through the parametrically driven and damped nonlinear Schrödinger equation. The experimental validation of our theory was realized by measurements in a vertically accelerated water channel. The successful prediction of isolated pair interaction theory motivated us to consider the case of one-dimensional multi-soliton interaction as an analog of diluted gas of particles. This study allows the prediction of the power law of the multi-soliton interaction. On the basis of this power law, we have proposed a protocol to parametrically excite dissipative localized structures without the need of perturbations that falls in their basin of attraction. The theory developed for the localized structures interaction has also revealed the key role played by the phase. By a careful numerical analysis of the exact soliton solution of the PDNLS equation (2.7), it appears that the phase can acquire a non-uniform distribution. The study of this hidden phase dynamics is also presented. It leads to the proposition of novel type of dissipative LS which we have named *phase shielding soliton*. The PDNLS equation is undoubtedly a good model to describe parametrically excited dissipative structures.

In what concerns my activities on optical system, I have chosen to first present the results obtained in revisiting the spatiotemporal linear stability analysis. In the introductory part, I have mentioned the symmetry breaking process in terms of a homogeneous state which breaks up into a periodic state. This process shared by many physical systems is widely referred to as the modulational instability (MI). In the general context of the linear stability analysis, MI is characterized by assuming the solutions of the linearized equations of motion having the form of a *monochromatic* wave. It is known as the normal-mode approach which is an indispensable part of any linear stability analysis. However, within the normal-mode approach the dynamics of realistic spatially localized perturbations cannot be treated. To address this dynamics, one has to treat an initial-value problem formulation for the linearized equations of motion. Therefore, the use of the spatiotemporal theory in terms of convective and absolute instability

must be employed. This theory attempts to address the answer to the following questions. How does one describe the dynamical evolution of a localized pulse (wave packet) with both finite duration and size (finite spectrum and finite wave number) that emerges from fluctuations in unstable regime? What are the carrier frequency and wave number of the merging pulse? And more importantly what is the group velocity of the pulse? During its evolution does the wave packet spread in all directions (absolute unstable regime) or not (convective unstable regime)? Finally, if any, is there any transition from one regime to another? The answers to these questions are even more fundamental when the considered system exhibits intrinsic parity symmetry breaking. We have considered these problems in two contexts: the case of simple propagation described by the Nonlinear Schrödinger equation and also the case of the fiber ring cavity where the effects of the slope of the dispersion curve have been included. The results of this latter case can be clearly identified as the starting point of one of my currently main concerns: the spatiotemporal chaos and their connection to the extreme events or rogue waves dynamics. Extreme events or rogue waves are also called freak waves, killer waves, abnormal waves, depending on the authors. They are occasional occurrence of abrupt excursions to values that differ significantly from the average level. In just a few short years, the study of extreme events has become a topic of growing interest. Optical analogue of the hydrodynamic rogue waves are short duration and intense light pulse. They may result from collisions of solitons or from emergence of a class of exact solutions of the mathematical model under study. Extreme events were initially studied in the context of conservative systems. However, these concerns rapidly extended to dissipative systems. This part of the manuscript is devoted to a description of the formulation of tools from the theory of chaos. The connection of measured pertinent observables with the emergence of extreme event is also discussed.

Parametric dissipative structures: *Interactions and hidden dynamics*

6.1/ Soliton pair interaction

Related publications: [32, 34, 35]

This work was done during my postdoctoral position at the University of Chile in Santiago. The general purpose was the study of parametrically excited dissipative LS. At this moment, an unexplored feature was the behavior of such a LS when coexisting with another one. Indeed, there were many attempts in this direction in both experiments and numerics without providing an analytical prediction [Gordillo, 2012]. Here below the outline of our attempts to address this theoretical lack starting with the Eq. (2.7). For a negative detuning ($\nu < 0$), Eq. (2.7) has non trivial exact steady *solitonic* solutions of the form [Barashenkov et al., 1991]:

$$\cos(2\theta_0) = \frac{\mu}{\gamma}, \quad (6.1a)$$

$$R_{\pm}(X) = \sqrt{2}\delta_{\pm}\operatorname{sech}(\delta_{\pm}[X - X_0]), \quad (6.1b)$$

where $\delta_{\pm} = \sqrt{-\nu - \gamma \sin(2\theta_0)} = \sqrt{-\nu \pm \sqrt{\gamma^2 - \mu^2}}$ such that $\psi(X, \tau) \equiv \psi_{\pm}(X) = \chi R_{\pm}(X)e^{i\theta_0}$.

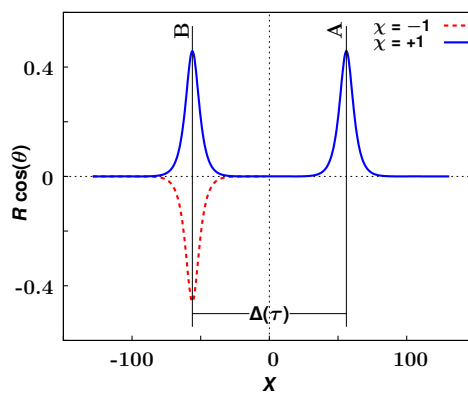


Figure 6.1: Illustration of a state of pair of interacting dissipative solitons. The aim of the theoretical study is the determination of the effective phase and the instantaneous velocity ($\dot{\Delta}$) of solitons.

Thus, these solitons are completely characterized by: two related parameters, amplitude ($\sqrt{2}\delta_{\pm}$) and width (δ_{\pm}^{-1}), the phase, θ_0 that is fixed by the balance between injection and dissipation of energy, plus two others arbitrary parameters, the position (X_0) linked to spatial translation symmetry displayed by Eq. (2.7) and the *polarity* ($\chi = \pm 1$, hence this is a sign parameter). ψ_+ solutions are stable only when $\mu < \gamma < \sqrt{\mu^2 + \nu^2}$ with small detuning. That is, describing the interaction of adjacent and isolated two solitons given is equivalent to model the configuration depicted in Figure 6.1.

A solution of this state can be written as

$$R(X, \tau) = R_+^0 \left(X - \frac{\Delta(\tau)}{2} \right) + \chi R_+^0 \left(X + \frac{\Delta(\tau)}{2} \right) + \rho(X, \Delta), \quad (6.2a)$$

$$\theta(X, \tau) = \theta_0 + \varphi(X, \Delta), \quad (6.2b)$$

where $\rho(X, \Delta)$ and $\varphi(X, \Delta)$ are small correction functions. For simplicity, we focus on the parameter region near the saddle-node bifurcation, that is $\sqrt{\gamma^2 - \mu^2} \ll \mu \sim \gamma$. In addition, we consider that the solitons are sufficiently separated from each other (diluted) so then we can consider that $\Delta(t)$ varies slowly. Consequently, we have $\ddot{\Delta} \ll \dot{\Delta} \ll 1$ and $\Delta \cdot \delta_+^{1/2} \gg 1$. Introducing the ansatz $\psi = R(X, \tau) \exp[i\theta(X, \tau)]$ in Eq. (2.7), and using the parameter variation method, we obtained after straightforward calculations (see Ref. [Clerc et al., 2009] and details therein) the expression of the phase correction $\varphi(X, \Delta)$ and the instantaneous position $\Delta(t)$ of the form:

$$\varphi = \dot{\Delta} \Theta(X, \Delta) + O(\sqrt{\gamma - \mu}), \quad (6.3a)$$

$$\dot{\Delta} = -\frac{3\chi \langle \partial_{z_+} R_{+,+} | R_{+,+}^2 R_{+,-} \rangle}{2\mu \langle \partial_{z_+} R_{+,+} | W\Theta \rangle}, \quad (6.3b)$$

where

$$\Theta(X, \Delta) \equiv -\int_{-\infty}^X \frac{dX'}{2W^2} \int_{-\infty}^{X'} dy W(\partial_{z_+} R_{+,+} - \chi \partial_{z_-} R_{+,-}), \quad (6.4a)$$

$$\langle \partial_{z_+} R_{+,+} | W\Theta \rangle = -\int_{-\infty}^{\infty} dz \partial_z R_{+,+} W(z) \int_{-\infty}^X \frac{dX'}{W^2(X')} \int_{-\infty}^{X'} dy W(y) \Lambda(y), \quad (6.4b)$$

$$\langle \partial_{z_+} R_{+,+} | R_{+,+}^2 R_{+,-} \rangle = \int_{-\infty}^{\infty} dz \partial_z R_{+,+}(z) R_{+,+}^2(z) R_{+,-}(z + \Delta), \quad (6.4c)$$

$$W = R_+^0(z_+ \equiv X - \Delta/2) + \chi R_+^0(z_- \equiv X + \Delta/2) = (R_{+,+} + \chi R_{+,-}), \quad (6.4d)$$

$$\Lambda(y) \equiv \partial_{z_+} R_{+,+}(y) - \chi \partial_{z_-} R_{+,-}(y). \quad (6.4e)$$

Integrals (6.4.a-c) can be evaluated taking whichever of the two solitons and considering the asymptotic tendency of one soliton around the other one. For this purpose, let us consider the soliton $R_{+,+}$ (which is represented by the curve around A in Figure 6.1), where the soliton represented by the curve around B decays exponentially: $R_{+,-}(z + \Delta) \approx 2\sqrt{2}\delta_+ e^{-\delta_+(z+\Delta)}$. Then the integral (6.4.c) can be approximated by

$$\langle \partial_{z_+} R_{+,+} | R_{+,+}^2 R_{+,-} \rangle \approx 2\sqrt{2}\delta_+ e^{-\delta_+\Delta} \int_{-\infty}^{\infty} dz \partial_z R_{+,+}(z) R_{+,+}^2(z) e^{-\delta_+z}, \quad (6.5)$$

leading finally to the law of soliton pair interaction [Clerc et al., 2009]

$$\dot{\Delta} \approx -\mathcal{R}\chi e^{-\delta_+\Delta}, \quad (6.6)$$

where

$$\mathcal{R} = \frac{3\sqrt{2}\delta_+ \int_{-\infty}^{\infty} dz \partial_z R_{+,+}(z) R_{+,+}^2(z) e^{-\delta_+z}}{\mu \int_{-\infty}^{\infty} dz \partial_z R_{+,+} W(z) \int_{-\infty}^X \frac{dX'}{W^2(X')} \int_{-\infty}^{X'} dy W(y) \Lambda(y)} \quad (6.7)$$

is a positive constant. In the limit of large interaction distance, \mathcal{R} explicitly reads:

$$\mathcal{R} = \frac{8\delta_+^3}{\mu}. \quad (6.8)$$

Therefore, the dynamics of a pair of solitons is over-damped and governed by interactions

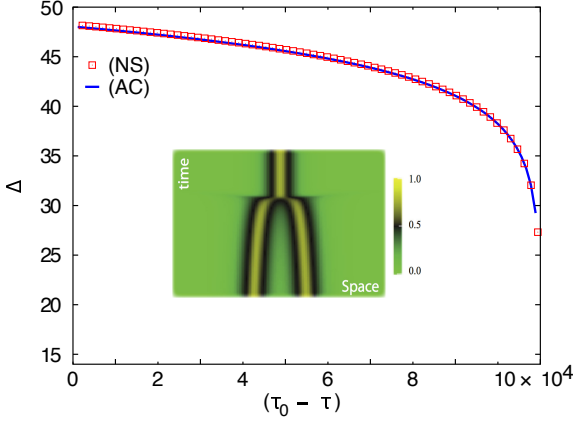


Figure 6.2: Temporal evolution of two soliton separation distance $\Delta(t)$. The red squares stand for the distance obtained numerically from Eq. (2.7). The corresponding spatiotemporal diagram is given in inset. The solid line is obtained from the formula (6.9). The parameters are $\mu = 0.115$, $\gamma = 0.27$, and $\nu = -0.063$.

that decrease exponentially with the soliton-soliton distance. This interaction is attractive (repulsive) when solitons are in (out of) phase, that is for $\chi = 1$ ($\chi = -1$). For a given initial condition, we can integrate the evolution of the soliton distance, which takes the form

$$\Delta(\tau) = \frac{1}{\delta_+} \ln(\delta_+ \mathcal{R}(\tau_0 - \tau)), \quad (6.9)$$

where τ_0 is determined by the initial condition by

$$\tau_0 = \chi \frac{e^{\delta_+ \Delta_0(\tau=0)}}{\delta_+ \mathcal{R}}, \quad (6.10)$$

and Δ_0 accounts for both the initial condition and the critical separation distance.

For in-phase solitons, formula (6.9) is valid only for $\tau < \tau_0$. This time is related to the characteristic time of fusion between the two particles. Hence, two dissipative solitons that are in-phase follow a logarithmic decrease of their separation distance. Otherwise, the separation distance increases. The configuration depicted in Fig 6.1 has been used as the initial condition of the numerical integration of Eq. (6.9). The result is displayed in Fig 6.2. As can be seen from this figure, evolution of the intra-pulse separation distance is in a good agreement with the analytical prediction. The experimental measurements in the rectangular water channel described in chapter 4 are also in a good agreement with the logarithmic law predicted by the Eq. (6.9) as shown in Figs. 6.3.

With an adequate initial condition, a multi-soliton state can be formed (see e.g. Fig 6.4a). The evolution of this state displays a cascade of pair interaction described above. In such a state, the evolution is mainly mediated by the nearest neighbor interaction because of the exponentially decaying interaction strength. Hence, the multi-soliton state can be seen as a set of three interacting solitons as depicted in Fig 6.4b. Therefore, time needed to move from three to a single soliton is given by $\tau'_0 \propto e^{\delta_+ \tilde{\Delta}} + e^{3\delta_+ \tilde{\Delta}/2}$, where $2\tilde{\Delta}$ is the distance between the $(i-1)$ -th and $(i+1)$ -th soliton. When $\tilde{\Delta}$ is large, the following approximation: $\tau_0 \approx \tau_1 = e^{3\delta_+ \tilde{\Delta}/2}$ may be used. For a large number of solitons it is convenient to follow the evolution of the average distance defined as

$$\langle \Delta \rangle = \frac{\sum_{i=0} (z_{i+1} - z_i)}{N}, \quad (6.11)$$

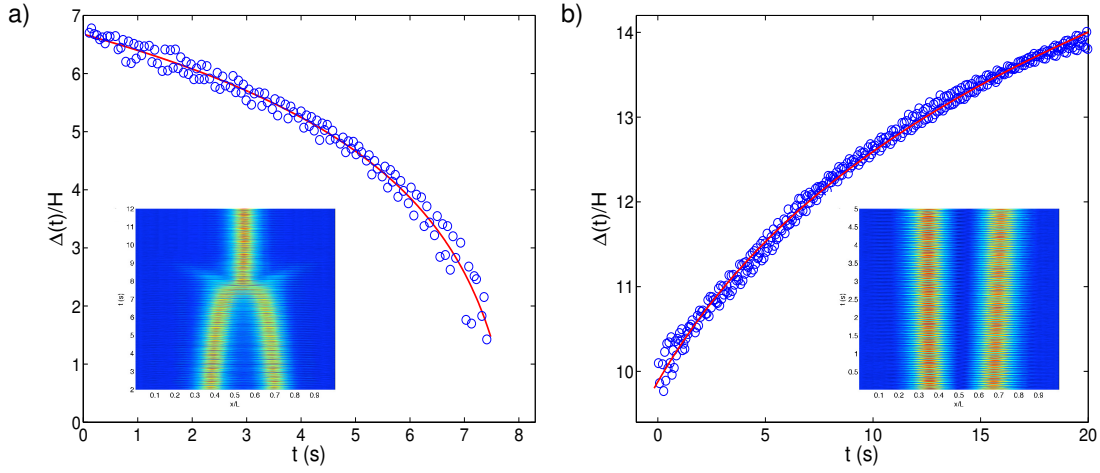


Figure 6.3: Interaction processes of two solitons in phase (a) and out of phase (b) obtained experimentally in a vertically driven rectangular water container. The symbols (\circ) are extracted from the surface elevation profile $h(x, t)$ (density plots inserts). The continuous curves are the corresponding fit $\Delta(t) = a \cdot \ln(b \cdot (t_0 - t))$ motivated by formula (6.9). Adjusted parameters are: $\{a/H = 2.1 \pm 0.2, b = 2.8 \pm 0.6 \text{ s}^{-1} \text{ and } t_0 = 8.2 \pm 0.2 \text{ s}\}$ and $\{a/H = 3.0 \pm 0.2, b = 3.8 \pm 0.9 \text{ s}^{-1} \text{ and } t_0 = 6.9 \pm 0.6 \text{ s}\}$ for (a) and for (b), respectively.

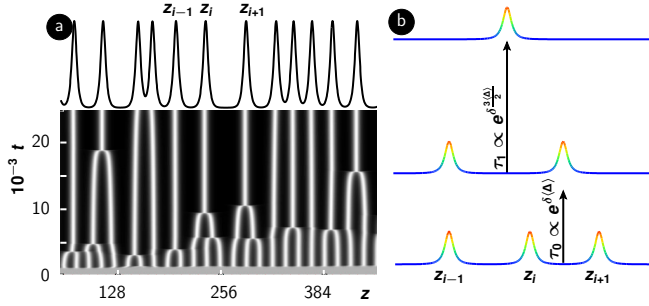


Figure 6.4: (a) Amplitude spatio-temporal density plot of numerical solution of Eq. (2.7) for $\mu = 0.05$, $\gamma = 0.053$, and $\nu = -0.03$. The black solid line represents the profile at a given time. (b) Geometrical picture of the three interacting solitons.

with N the number of dissipative solitons. Consequently, the average distance $\langle\Delta\rangle$ is an implicit function of the time through the quantity N which is a time-dependent function as a consequence of the coalescence process ($\langle\Delta\rangle = f(t)$). Changing the distance from $\langle\Delta\rangle$ to $\langle\Delta\rangle + \langle\Delta\rangle_0$ produces a dilation of the collision time from t_0 to $t_0 e^{3\delta\langle\Delta\rangle_0/2}$. Thus, the dynamics controlled by Eq. (6.11) is self-similar. Introducing the following self-similar law

$$z_{i+1} - z_{i-1} \rightarrow z_{i+1} - z_{i-1} + \langle\Delta\rangle_0, \quad (6.12a)$$

$$t \rightarrow t e^{3\delta\langle\Delta\rangle_0/2}, \quad (6.12b)$$

Eq. (6.11) is invariant. We get that $f(t)$ must satisfy the condition:

$$f(t) + 2\langle\Delta\rangle_0 = f(te^{3\delta\langle\Delta\rangle_0/2}),$$

from which we deduce the temporal evolution of the average distance $\langle\Delta\rangle$ as coarsening law:

$$\langle\Delta\rangle = \langle\Delta\rangle_0 + \frac{4}{3\delta} \ln t, \quad (6.13)$$

where $\langle\Delta\rangle_0$ is an arbitrary constant depending on the initial condition. Therefore, for a dilute gas of solitons the average separation between solitons grows logarithmically with time. Finally,

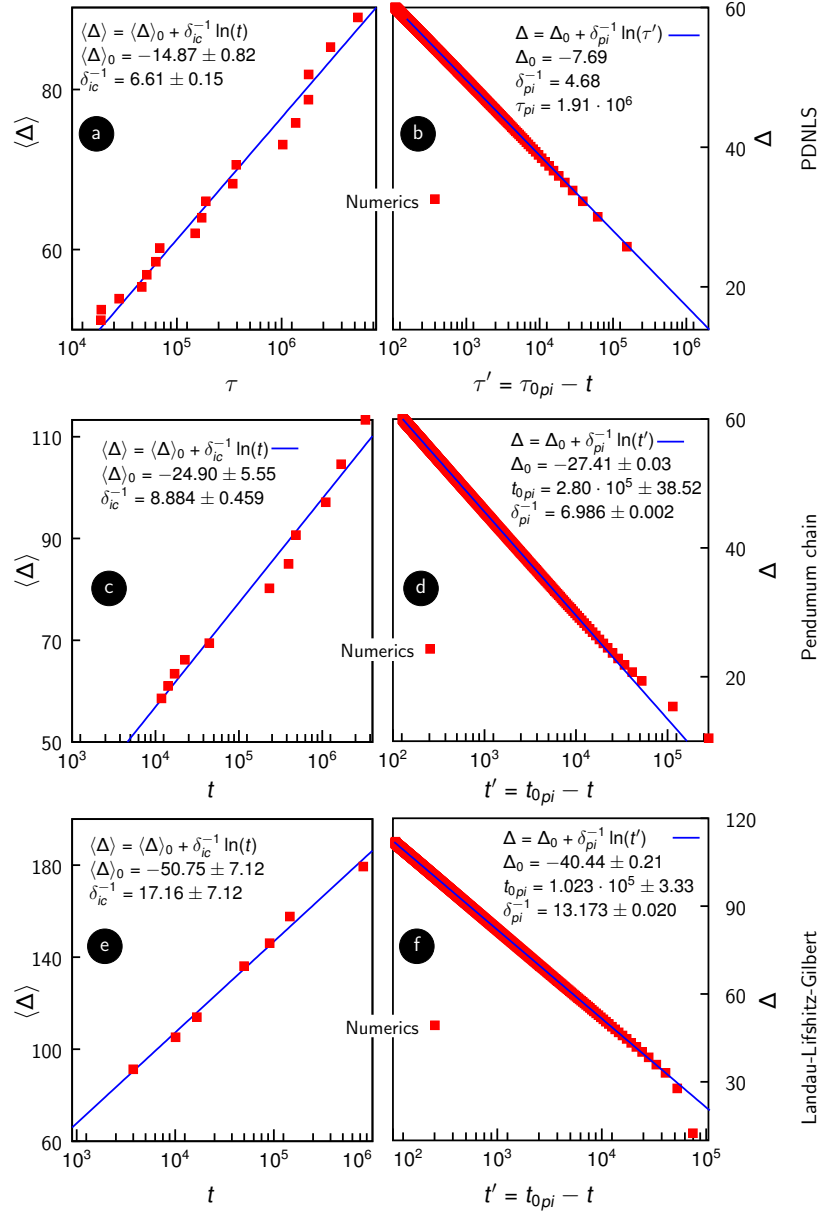


Figure 6.5: Left column: Average soliton-soliton distance evolution for the coalescence cascade. Right column: the separation distance for a soliton pair that survives almost to the end of the cascade coalescence process. Squares represent the numerical results and the blue solid lines give the nonlinear interpolations with respect to our analytical predictions Eqs. (6.9) and (6.13). The numerical results obtained from: (a-b) the PDNLS equation [$\mu = 0.05$, $\gamma = 0.053$, and $\nu = -0.03$]; (c-d) the pendulum chain [$\gamma = 0.21$, $\mu = 0.1$, $\nu = -0.03$] and (e-f) the ferromagnetic spin chain [$H_0 = 0.2$, $h_1 = 0.044$, $\beta = 4.8$, $\alpha = 0.02$, $\nu = -0.03$].

numerical simulations of the prototype model of Eq. (2.7), the chain of pendulum Eq. (2.2), and the 1D chain of spin Eq. (3.3) provide a validation of this power law (see Figure 6.5).

Parametrically excited solitons given by (6.1) appear via a saddle-node bifurcation. Hence, they are generated only if an external perturbation falls into their basin of attraction. Any spontaneous formation is *a priori* not possible. By contrast, a non zero homogeneous steady state can emerge spontaneously inside the Arnold's tongue $|\nu| \leq \sqrt{\gamma^2 - \mu^2}$. This homogeneous

solution is modulationally unstable in the stability domain of the solitons. Then, starting with a detuning inside the tongue and switching in the stability domain of the non-propagative soliton, modulational instabilities leads to a cascade of coalescing collisions (cf. Figs. 6.4). The law of Eq. (6.13) allows the estimation of the time to reach an quasi-stationary solitons state, with any external energy injection.

6.2/ Hidden dynamics of parametrically driven systems

Related publications: [19, 25, 31]

From the study of the interaction process, it follows from (6.3a) that the surviving soliton should present a homogeneous phase profile. Instead of, we have observed that the phase still displaying a complex dynamics. Therefore, we have closely analyzed the phase dynamics of the single soliton to check if the observed non-homogeneous phase was a remanent effect of the interaction. The results of the numerical simulations were surprising. Even starting with a single soliton, many non-homogeneous phase distributions were observed. Some of these results are displayed in Figure 6.6. In all the cases, we can observe the variation in the

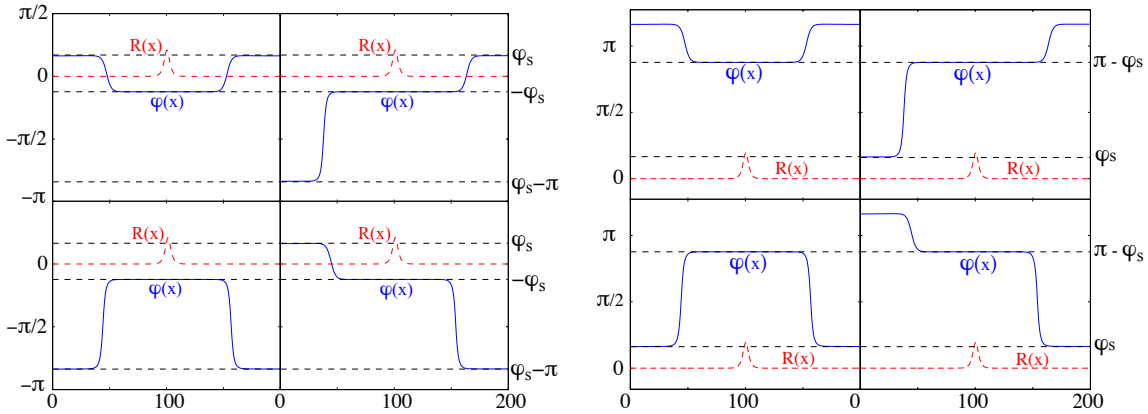


Figure 6.6: Different Phase Shielding Soliton states (PSS) in the parametrically driven damped non-linear Schrödinger equation with $\mu = 0.10$, $\nu = -0.12$, $\gamma = 0.14$, and $L = 200$. Dashed (red) and solid (blue) lines account for the modulus and phase of the complex field, respectively.

structure of the phase far from the location of the *center-of-mass* of the soliton. Therefore, without loss of generality the profile of the phase can be studied considering the asymptotic behavior of the amplitude. Next, owing to the symmetry displayed by the observed distributions, the analytical treatment could be done in a semi-infinite domain. Let's recall the *ansatz* $\psi = R(X, \tau) \exp[i\phi(X, \tau)]$ with $R(X, \tau)$ given by (6.1b). Taking $R(X, \tau) \rightarrow 2\sqrt{2\delta}e^{-\sqrt{\delta}(X-X_0)}$ for $(X - X_0) \rightarrow \infty$ the equation for $\phi(X, \tau)$ can be written in the form:

$$\partial_{XX}\phi = 2\sqrt{\delta}\partial_X\phi + \mu - \gamma \cos(2\phi). \quad (6.14)$$

This equation has heteroclinic solutions corresponding to phase fronts, which are analytically well described by the following *ansatz*:

$$\phi_F \approx \arctan \left[\sqrt{\frac{\gamma - 2\mu}{\gamma + 2\mu}} \tanh \frac{\sqrt{\gamma^2 - 4\mu^2}(X - X_f)}{\sqrt{-8\nu + 4\sqrt{\gamma^2 - 4\mu^2}}} \right], \quad (6.15)$$

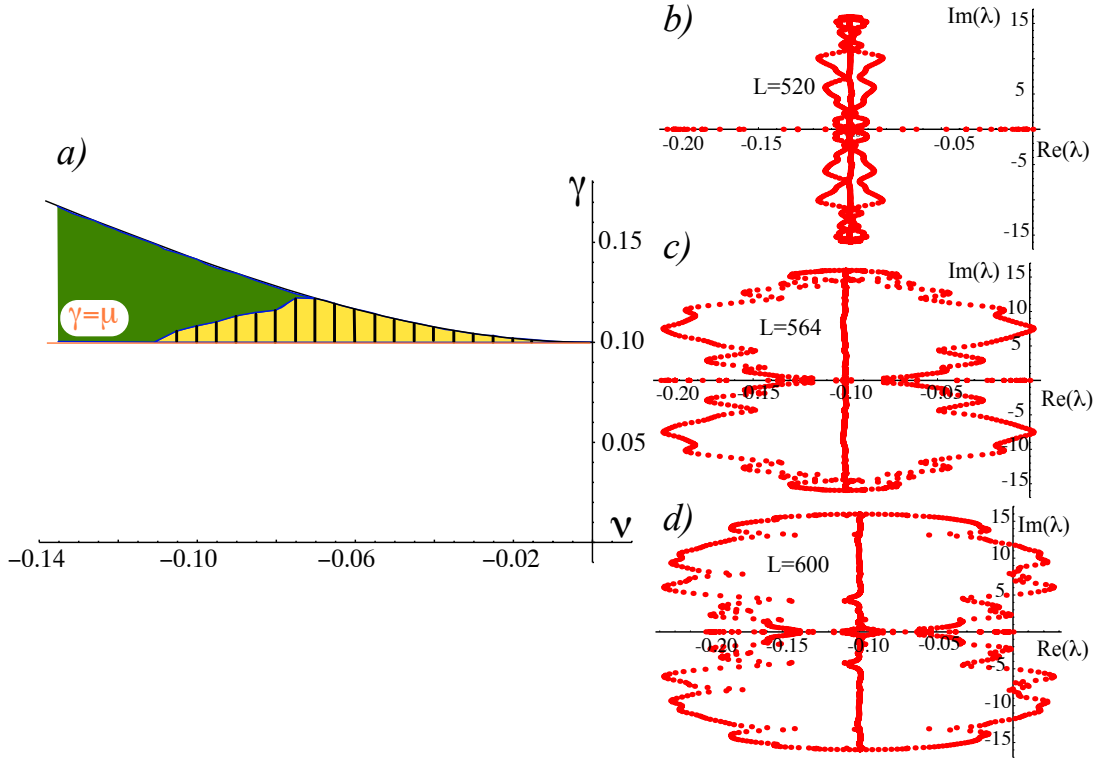


Figure 6.7: Stability of solitons: a) Bifurcation diagram in the $\gamma - \nu$ space for $\mu = 0.1$, the painted region corresponds to the phase shielding soliton region and striped area is the region of soliton with constant phase. b), c) and d) are the spectra of the soliton with constant phase before (system size $L = 520$), during ($L = 564$) and after ($L = 600$) the bifurcation, respectively, for $\gamma = 0.105$, $\mu = 0.1$, and $\nu = -0.08$.

where x_f accounts for the position of phase front, i.e. the point at which the spatial derivative of the phase front has its global maximum. Hence, using the same strategy as in the study of the solitons interaction leads to an equation for the position x_f :

$$\dot{X}_f = A + B e^{-2\sqrt{\delta}X_f}, \quad (6.16)$$

with $A = \int_{-\infty}^{\infty} [\nu + \delta + \sin(2\varphi_F) - (\partial_z \varphi_F)^2] \partial_z \varphi_F dz / C$, $C = \int_{-\infty}^{\infty} (\partial_z \varphi_F)^2 dz$ and $B = 8\delta \int_{-\infty}^{\infty} e^{-2\sqrt{\delta}z} \partial_z \varphi_F dz / C$ where $z = X - X_f$. A and B are real quantities whose signs depend on the transient phase configuration. However, in most of the configurations, they are of opposite sign providing stable equilibrium solution X_f^s for X_f . Generally speaking, X_f^s roughly corresponds to the homogenous extension of the phase around the soliton. Consequently, the constant phase soliton can be observed only if the spatial domain is smaller than X_f^s . This result has been confirmed by the stability analysis of the constant phase soliton by computing its linear spectrum for different sizes of the system as shown in Figure 6.7.

In two dimensional extended systems, parametrically excited stable solitons have been also observed. In that case, we have shown that the solitons always embed all the possible stable configurations that can be observed in the 1D case. This result is summed up by the Figure 6.8.

Numerical simulations have also been performed to confirm the presence of the shell-type phase structure in the microscopic set of equations. The main observations are that in many

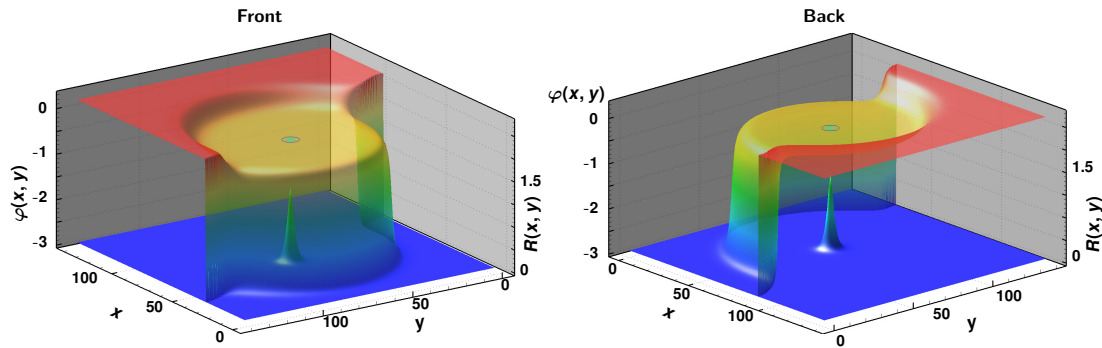


Figure 6.8: Front and back view Phase shielding soliton observed in two-dimensions for the Eq (2.7) with $\gamma = 0.140$, $\nu = -0.068$ and $\mu = 0.125$.

cases only a 2π symmetric phases remains. Careful investigations have shown the key role played by the higher order correction terms in each particular system. These corrections correspond to higher-order terms that are not taken into account in the amplitude equation approach at dominant order. Such corrections are negligible far from the position of the dissipative soliton but become relevant in the phase near the soliton core. The presence of corrective terms also affects the phase dynamics itself, as the phase front dynamics is led by an exponentially small force.

Spatiotemporal dynamics in optical fiber systems: *Convective/Absolute instability and spatiotemporal chaos*

7.1/ Convective/Absolute instability of the Nonlinear Schrödinger equation

Related publications: [7, 17, 21, 23, 27]

Developed by Briggs [Briggs, 1964], the study of the dynamics of an initial localized disturbances, i.e., absolute and convective instabilities, is treated as a linear initial-value problem. The key tool consists on the evaluation of the asymptotic solution of the problem in both space and time, using a combined Fourier-Laplace transform and a consistent mathematical formalism (see also [Bers, 1973]). Here, this theory is revisited in the framework of the scalar NLS.

In the reference frame corresponding to a stationary observer, the linear response of a dynamical system can be expressed as an inverse Fourier-Laplace integral:

$$\varphi(x, t) = \int_{-\infty}^{\infty} dk \int_{i\sigma-\infty}^{i\sigma+\infty} \frac{S(\omega, k)}{D(\omega, k)} e^{i(kx_0 - \omega t)} d\omega, \quad (7.1)$$

where the function $S(\omega, k)$ represents the external perturbations, and $D(\omega, k)$ the dispersion-relation function of the system. In the inverse Laplace integral in (7.1), the integration is performed along the Bromwich contour [Drazin and Reid, 2004],

$$\mathcal{B} = \{\omega | \omega_i = \sigma, -\infty < \omega_r < \infty\}, \quad (7.2)$$

where σ is greater than the maximum growth rate of the monochromatic waves, $\sigma > \sigma_m = \max\{\omega_i | D(k, \omega) = 0, -\infty < k < \infty\}$.

In practice, it is convenient to consider the general case of the solution in a frame of reference moving with the velocity V with respect to the absolute frame, that is $x = x_0 + Vt$, where x_0 is fixed. In the moving frame, by a change of variable in the double integral the solution can be brought to the form

$$\varphi(x_0 + Vt, t) = \int_{-\infty}^{\infty} dk \int_{i\sigma-\infty}^{i\sigma+\infty} \frac{S(\omega + Vk, k)}{D(\omega + Vk, k)} e^{i(kx_0 - \omega t)} d\omega. \quad (7.3)$$

Since the function $S(\omega, k)$ represents the external disturbance is in some sense arbitrary. That is, it does not affects the asymptotic properties of the solution.

Therefore, given that V is fixed, the Briggs [Briggs, 1964] collision criterion (see also [Bers, 1973]) may apply in the evaluation of the integral (7.3). This criterion allows to identify

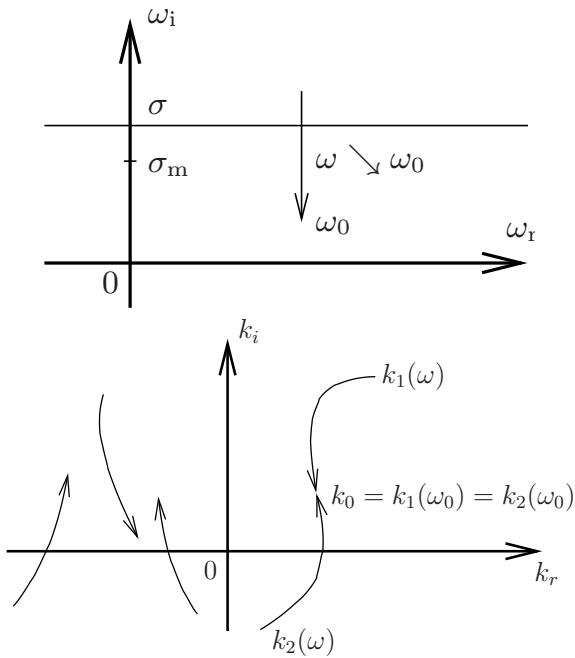


Figure 7.1: Movement $\omega \searrow \omega_0$ of ω (top) and the corresponding conformal map in the complex k plane (bottom). It illustrates the collision of two k -roots originating on opposite sides of the real k -axis when $\omega \searrow \omega_0$.

the points in the upper complex half-plane, $\{\omega_i > 0\}$, that contribute to the temporal growth of the solution. For the solution given in (7.1) the identification is performed as follows. Let ω_0 be a point in the upper complex half-plane (positive gain) and let $\omega \searrow \omega_0$ denotes a movement of the point ω along the vertical line passing through ω_0 from above the Bromwich contour till ω_0 , as illustrated in the top panel of Figure 7.1. We also denote $k_n(\omega), n = 1, 2, \dots$, all the k -roots of $D(k, \omega) = 0$. For ω laying above the Bromwich contour, all the k -roots are located away from the real k -axis because $\sigma > \sigma_m$. When $\omega \searrow \omega_0$ the k -roots move in the complex k -plane. The point ω_0 contributes to the growth of the solution if and only if, in the most common case, two of the k -roots originating on opposite sides of the real k -axis collide when ω reaches the point ω_0 in the movement $\omega \searrow \omega_0$. This type of a collision is called a pinching collision. Generally, a collision of at least two of the several k -roots originating on opposite sides of the real k -axis will produce a point ω_0 contributing to the instability [Brevdo, 1988, Ward et al., 2000]. Hence, at the collision point $k = k_0$, the function $D(k, \omega)$ has at least a double root in k . Formally, the latter satisfies:

$$D(\omega + Vk, k) = 0, \quad \frac{\partial D(\omega + Vk, k)}{\partial k} = 0, \quad (7.4)$$

which simplifies to $\frac{d\omega(k_0)}{dk} = 0$. Finally, the contribution of a point (ω_0, k_0) to the asymptotic solution ($t \rightarrow \infty$) is given by:

$$C(x_0, \omega_0) = a(k_0, \omega_0, x_0) \frac{1}{\sqrt{t}} e^{ik_0 x_0} e^{-i\omega_0 t}, \quad (7.5)$$

where $k = k_0$ is the collision point as described above. In many cases, the k -roots of $D(k, \omega) = 0$ cannot be explicitly computed analytically. If so, the points satisfying the collision criterion can be found by numerically following the movement of the images of the Bromwich contour on the complex k -plane under the transformations $k = k_n(\omega), n = 1, 2, \dots$. Hence, the asymptotic evolution of $C(x_0, \omega_0)$ is an exponential growth (decay) if $\{\Re(\omega_0) > 0\}$ ($\{\Re(\omega_0) < 0\}$). For $\Re(k_0) = 0$ one can then observe $t^{-1/2}$ power law decay.

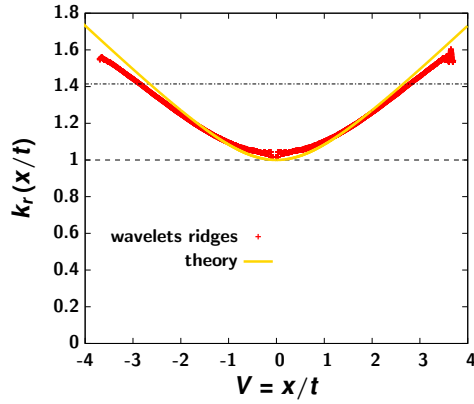


Figure 7.2: Local wavenumber of the impulse response (solid line) and the wavelet ridges (+) of the numerical solution of the Eq. (5.19) from an initial impulse condition.

We have used the approach described above in the case of the nonlinear Schrödinger equation (5.19),¹ and obtained the impulse response. Here, I only focus on the result of our analysis of the phase. Indeed, the analytical solution provides us an access to the instantaneous phase profile. Therefore, we have compared this profile with those obtained by the numerical integration of the Eq. (5.19) for a large nonlinear length to validate the linear approximation. The instantaneous profile was computed by detecting the wavelet ridges. The result is displayed in Figure 7.2. As can be seen from this figure, no local wavenumber exists in the band $|k_r^0| < 1$

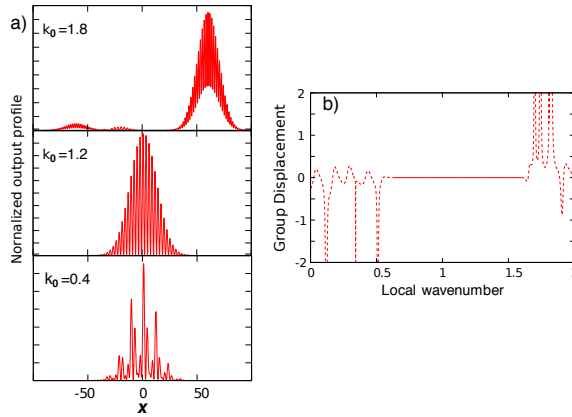


Figure 7.3: Normalized output profiles corresponding to Gaussian initial perturbations ($\varphi(x, 0) \propto e^{-(x/20)^2} e^{-ik_0 x}$). Integration time is $t = 30$.

(see Figure 7.2). This result is quiet surprising, since the initial condition is characterized by a homogeneous spectrum. To elucidate this point, we have integrated Eq. (5.19) starting with a gaussian wavepacket. The results are summarized in Figure 7.3 which gives different characteristic behaviors. Indeed, for a range of k_0 around 1 the growth of the wavepacket preserve the initial profile. Outside this range the initial profile is lost. Hence, by analogy to the *group delay* of a temporal pulse, we have computed the *group displacement*. This quantity provide an estimation of the translational shift variation as a function of the wavenumber of an impulse traveling through the system. The result is given in Figure 7.3b. As can be seen from this figure, the *group displacement* is zero for $0.6 \leq k \leq 1.7$ and presents fast variations elsewhere. On the other hand it appears from this result that starting with a pulse with central wavenumber lying in the aforementioned region does not produce any distortion. In contrary, any initial pulse with central wavenumber outside this region will experience some distortions leading to a non-localized structure as can be seen from right panels on Figure 7.3a.

When the considered system exhibits an intrinsic symmetry-breaking, two scenarios can be observed from the growing wavepacket. In the first scenario, the localized disturbance moves

¹Actually, we have use the spatial version of the Eq. (5.19): $\psi_t = i\psi_{xx} + i|\psi|^2\psi$.

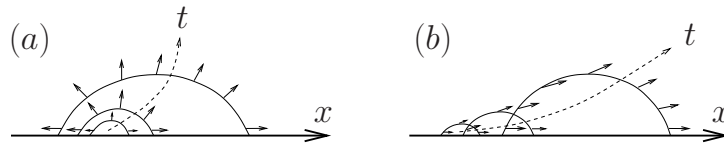


Figure 7.4: (a) Absolute instability; (b) convective instability

away from the place of its origin, but spreads in space fast enough so that, at every point of the medium, growth occurs destroying eventually the base state throughout. This is the scenario of absolute instability. In the alternative scenario, the temporally growing wave-train propagates in space more rapidly than it spreads leaving behind, during such a development, a decaying disturbance at every fixed point in space. In this case the medium is called absolutely stable, but convectively unstable. A schematic one-dimensional illustration of the spatiotemporal evolution of the envelope of wave-train in the absolutely unstable case and in the convectively unstable, but absolutely stable case is presented in Figure 7.4. In optical fiber systems, when the group velocity dispersion parameter (β_2) is small, the effect of the slope of the dispersion curve (β_3) can become important. The impact of this latter parameter has been widely explored. All these study have pointed out that third order dispersion deeply impacts the evolution when evolving state is localized. In the case of the fiber ring cavity, the nonlinear stage of the modulational instability is also affected. Consequently, the slowly varying envelope S of the modulational instability was found to obey to following equation:

$$\frac{\partial S}{\partial t} = S + (1 + ib)\frac{\partial^2 S}{\partial \tau^2} - (1 + ic)|S|^2 S, \quad (7.6)$$

where b and c are real values that vanished for $\beta_3 = 0$. This equation is referred to as the complex Ginzburg-Landau equation. In turn, this envelope has a traveling solution whose stability can be studied in scope of the convective/absolute theory. The transition from convective to absolute regime was already reported. However, as shown by the results of the numerical simulations in Figure 7.5 of the Eq. (7.6) the transition coincides with a spatiotemporal complex dynamics.

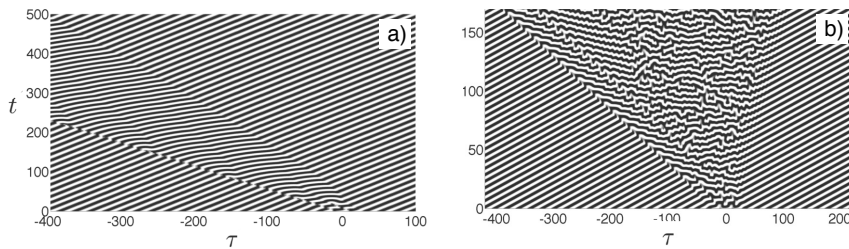


Figure 7.5: Convective (a) and absolute (b) instabilities displayed by the traveling wave solution of the complex Ginzburg-Landau equation.

This result was a turning point in my activities. Indeed, the Lugiato-Lefever equation is known to support extremely complex dynamics since the first derivations. The general applicability of this equation to driven dissipative passive resonators, plus the abundance of the complexity that it exhibits was the motivation to have some tools that can be used when conventional tools fail². In this sense, one of the best ways to address the stability whenever the nature of the regime (from linear to strongly nonlinear) is to consider it in the sense of

²By conventional tool, I mean linear and weakly nonlinear analyses.

Lyapunov. The following section is devoted to the basics and the application of this theory to some new concerns of the nonlinear dynamical system theory: the study of rogue waves.

7.2/ Spatiotemporal chaos and rogue waves dynamics

Related publications: [3, 6, 9, 8, 11]

When a dynamical system displays complex behavior, a major concern is to know how far nearby initial conditions in the phase space will be separated after a large number of iterations. To do so, one of the best approaches is the computation of the Lyapunov exponents. Here below, an introduction to this quantity initially called *Characteristic numbers of functions* by Lyapunov. Let's consider the case of a map given by: $x_{n+1} = f(x_n)$ where $f(x)$ is nonlinear function. That is, after one iteration, x_0 produces x_1 . Therefore, if we assume $|\delta x_0| \ll 1$ such that $\tilde{x}_0 = x_0 + \delta x_0$ produces $\tilde{x}_1 = x_1 + \delta x_1$ then,

$$\tilde{x}_1 = x_1 + \delta x_1 = f(x_0 + \delta x_0) \approx f(x_0) + \left. \frac{df}{dx} \right|_{x_0} \delta x_0. \quad (7.7)$$

From the single iteration deviation expression $\delta x_1 \approx f'(x_0) \delta x_0$ it follows for n -th iterations: $\delta x_1 = \prod_{m=0}^{n-1} f'(x_m) \delta x_0$. While the perturbations are small, for large enough iterations n , it is expected that $|\delta x_1| = \kappa^n |\delta x_0|$, where

$$\kappa \approx \lim_{n \rightarrow \infty} \left(\left| \frac{\delta x_1}{\delta x_0} \right| \right)^{1/n}. \quad (7.8)$$

Later, introducing the Lyapunov exponent $\lambda = \ln \kappa$ leads to

$$\lambda = \lim_{n \rightarrow \infty} \frac{1}{n} \sum_{m=0}^{n-1} \ln(|f'(x_m)|). \quad (7.9)$$

Actually, this is the largest Lyapunov exponent. Its determination allows the demonstration of a chaotic ($\lambda > 0$) or a non-chaotic ($\lambda < 0$) dynamical behavior. The computation of the largest Lyapunov exponent is a useful tool for low dimensional system (in general no more than 3 dynamical variables). For a d -dimensional system ($d \geq 3$) it is convenient to compute not only the largest exponent but a set of exponents also named Lyapunov spectrum. To introduce this concept, let's consider a d -dimensional system given by:

$$\frac{d\mathbf{u}}{dt} = \mathbf{F}(\mathbf{u}), \quad (7.10)$$

with an initial condition \mathbf{u}_0 and $\mathbf{u} \in \mathbb{R}^d$. Then, the evolution of a small perturbation \mathbf{w} of a trajectory $\tilde{\mathbf{u}}(t)$ in the phase space is described by the following linearized equation:

$$\frac{d\mathbf{w}}{dt} = \left. \frac{\partial \mathbf{F}(\mathbf{u})}{\partial \mathbf{u}} \right|_{\tilde{\mathbf{u}}} \mathbf{w} = M(\tilde{\mathbf{u}}) \mathbf{w}. \quad (7.11)$$

The Jacobian $M(\tilde{\mathbf{u}})$ is a function of time via $\tilde{\mathbf{u}}(t)$. Now, after some large time evolution, a set of initial conditions for Eq. (7.11) formed by a sphere of radius l is expected to transform into an ellipsoid with d principal axes. Let's label l_j , $j = 1, d$ these principal axes. Hence, the Lyapunov exponents for the trajectory $\tilde{\mathbf{u}}(t)$ are given by:

$$\lambda_j = \lim_{t \rightarrow \infty} \frac{1}{t} \ln \left(\frac{l_j}{l} \right). \quad (7.12)$$

In practice, the set of initial conditions is composed of N orthonormal vectors \mathbf{w}_k ($k = 1..N$) of radius one obtained by applying the modified Gram-Schmidt orthogonalization procedure such that $\langle \mathbf{w}_m, \mathbf{w}_n \rangle = \delta_{mn}$ and $\|\mathbf{w}_k\| = 1 \forall k$. The resulting initial condition matrix is given by $\mathbf{W}(t_0) = [\mathbf{w}_1(t_0) \ \mathbf{w}_2(t_0) \ \cdots \ \mathbf{w}_N(t_0)]$. Then, each iteration from t to $t + \Delta t$ transforms \mathbf{W} to \mathbf{W}' following (7.11). Next, the Gram-Schmidt procedure is applied again leading to $\mathbf{W}' = \mathbf{QR}$. Therefore, \mathbf{Q} is an orthogonal matrix and \mathbf{R} an upper-triangular matrix. The columns of \mathbf{Q} are then used as the initial conditions for the next iteration, while from the diagonal elements of \mathbf{R} it follows:

$$\lambda_k^n = \frac{1}{\Delta t} \ln \mathbf{R}_{kk}, \quad (7.13)$$

for the n -th iteration. Finally, for $n \rightarrow \infty$, the Lyapunov spectrum is obtained by averaging the λ_k^n and sorting descending ($\lambda_1 \geq \lambda_2 \geq \cdots \geq \lambda_N$). When a system is demonstrated chaotic, with the Lyapunov spectrum, one may be interested in the minimal number of variable to describe this attractor. There are many definition of the dimension of a chaotic attractor. However, after the computation of the Lyapunov spectrum, it is convenient to use the conjecture proposed by Yorke and Kaplan: the so-called Yorke-Kaplan dimension (D_{YK}) or Lyapunov dimension. In terms of the Lyapunov spectrum the Yorke-Kaplan dimension is given by [Ott, 2002]

$$D_{YK} \equiv p + \frac{\sum_{i=1}^p \lambda_i}{|\lambda_{p+1}|}, \quad (7.14)$$

where p is the largest integer that satisfies $\sum_{i=1}^p \lambda_i > 0$. The Lyapunov spectrum is also a useful tool to differentiate low dimensional temporal chaos and high dimensional spatiotemporal chaos. The Ruelle's conjecture states that the Lyapunov exponents should converge to a continuous spectrum in the presence of a spatiotemporal chaos. As a consequence, $D_{YK} \propto L^{nd}$ where nd is the number of *spatial* variables.

Taking advantage of the computing facility in the laboratory, we have implemented a parallel version of the algorithm described above. This implementation was performed to be independent of the dynamical system. Hence, we were able to apply it to various systems. Only two of them are presented here.

■ Spatiotemporal chaos of bistable ring resonators

The Lugiato-Lefever equation (5.24) is known to operate in both monostable or bistable regime. To do so, one has to set $\delta > \sqrt{3}\alpha$ for the bistability otherwise the system will operate in the monostable regime. In case of bistability, the Eq. (5.24) can exhibit a dissipative localized structure. By increasing the driving strength, this localized structure undergoes an Andronov-Hopf bifurcation leading to a breathing localized structure. Increasing further the driving, the breathing localized structure can seed two equal-speed counter-propagating fronts between the homogeneous and a complex spatiotemporal states. This process is illustrated in Figure 7.6a and 7.6b. The complex dynamics presented here was already reported. However, for the first time we were able to perform a rigorous characterization in terms of the Lyapunov spectrum. This leads to the conclusion that the complex dynamics observed is of a spatiotemporal chaos nature. We have also shown that the Yorke–Kaplan dimension can be considered as a good order parameter to characterize the bifurcation diagram associated with spatiotemporal chaos (see 7.6c). Finally, we have identified different operating regimes, in particular the co-existence between the spatiotemporal chaos, the breathing localized structure, and the homogeneous steady state.

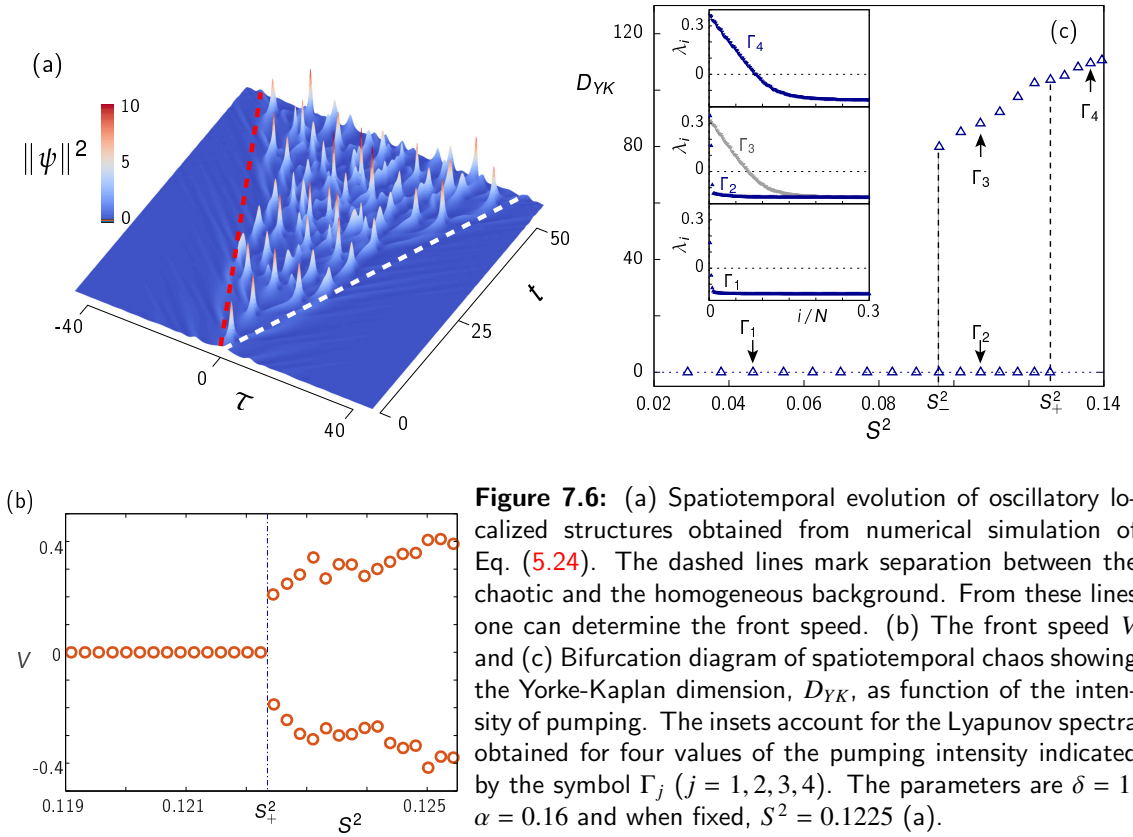


Figure 7.6: (a) Spatiotemporal evolution of oscillatory localized structures obtained from numerical simulation of Eq. (5.24). The dashed lines mark separation between the chaotic and the homogeneous background. From these lines one can determine the front speed. (b) The front speed V and (c) Bifurcation diagram of spatiotemporal chaos showing the Yorke-Kaplan dimension, D_{YK} , as function of the intensity of pumping. The insets account for the Lyapunov spectra obtained for four values of the pumping intensity indicated by the symbol Γ_j ($j = 1, 2, 3, 4$). The parameters are $\delta = 1$, $\alpha = 0.16$ and when fixed, $S^2 = 0.1225$ (a).

■ Spatiotemporal chaos-induced dissipative extreme events in a laser cavity

In recent years, a great effort has been devoted to the understanding of the observed large deviations in extended deterministic systems, the so called extreme events. As defined in [Nicolis and Nicolis, 2012], a time-recording of the dynamics of a macroscopic systems maintained out of equilibrium may consist of well defined periods where a relevant variable undergoes small variations around a well defined level. Occasionally, abrupt excursions to higher values that differ significantly from the average may appear, and these excursions are called extreme events. These events are ubiquitous in the nature. In optics, an extreme event is characterized by a rare and intense optical intensity pulse. The study of extreme events and extreme waves [Onorato et al., 2013] has been motivated by the analogy with rogue waves in hydrodynamics [Kharif and Pelinovsky, 2003] that are giant waves observed in the ocean. Indeed, some conservative systems in optics and deep water waves in the ocean can share a common description by the nonlinear Schrödinger equation [Solli et al., 2007]. Most of the studies in this context have taken place in optical fibers where the interplay of nonlinearity, dispersion and noise can generate extreme events [Dudley et al., 2008, Mussot et al., 2009, Kibler et al., 2010, Arecchi et al., 2011]. Extreme events in conservative systems are often associated with the merging dynamics of coherent structures [Antikainen et al., 2012, Birkholz et al., 2013, Pierangeli et al., 2015], and this mechanism has also been found in a dissipative, fiber-laser systems [Mussot et al., 2009, Lecaplain et al., 2012]. Other mechanisms observed in dissipative systems involve stochastically induced transitions in multi-stable systems [Pisarchik et al., 2011] or the temporal chaotic dynamics in a non spatially extended laser with optical injection [Bonatto et al., 2011]. Extreme events have been found in a variety of optical cavity systems, such as an injected nonlinear optical cavity [Montina et al., 2009], fiber lasers [Randoux and Suret, 2012,

[Lecaplain et al., 2012], solid-state lasers [Kovalsky et al., 2011], optical liquid crystal light valve with optical feedback [Clerc et al., 2016], and semiconductor lasers [Bonatto et al., 2011, Bosco et al., 2013]. Within the framework of a collaboration with our partners in Santiago and Paris-Saclay, the role of spatial coupling has been studied in an extended microcavity laser with integrated saturable absorber [Selmi et al., 2016]. Without the spatial coupling, this system is known to be free of any irregular dynamics. However, experimental measurements in a unidimensional configuration unveiled an increasing complexity with the pump power. From a theoretical perspective, the model of the aforementioned experiment consists in three coupled nonlinear partial differential equations

$$\begin{aligned}\frac{\partial E}{\partial t} &= [(1 - i\alpha)G + (1 - i\beta)Q - 1]E + i\frac{\partial^2 E}{\partial x^2}, \\ \frac{\partial G}{\partial t} &= \gamma_g [\mu - G(1 + |E|^2)], \\ \frac{\partial Q}{\partial t} &= \gamma_q [-\gamma - Q(1 + s|E|^2)],\end{aligned}\quad (7.15)$$

for the intracavity electric field amplitude $E(x, t)$, the carrier density in the gain (saturable absorber) medium $G(x, t)$ ($Q(x, t)$). The non-radiative carrier recombination rates are γ_g and γ_q with pumping μ and linear absorption γ . Our computation of the Lyapunov spectrum shows that the complexity induced the spatial coupling is spatiotemporal chaos.

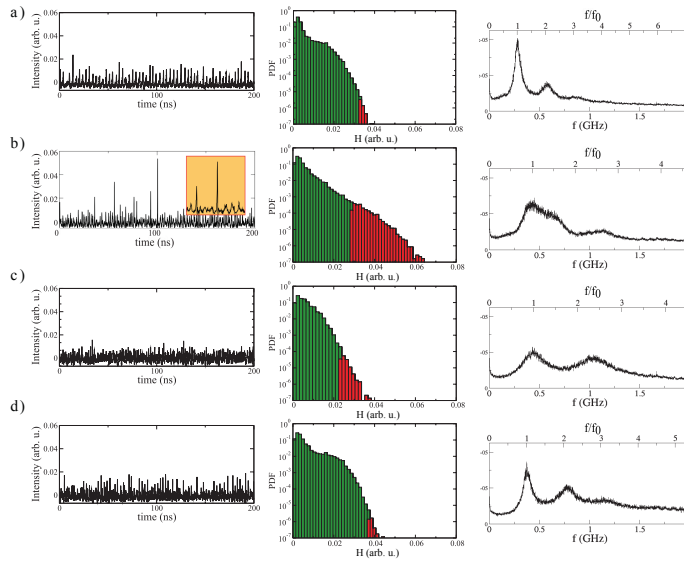


Figure 7.7: Experimental observation of extreme events in a spatially extended microcavity laser. Excerpt of the temporal evolution of the intensity at a fixed position, corresponding logarithm of the PDF of the intensity height H and Fourier spectrum for different normalized pump values P/P_{th} : a) 1.02, b) 1.17, c) 1.20 and d) 1.25. Extreme events ($AI > 2$) are emphasize in red.

The outstanding feature of this result is that the emergence of this complexity is followed by a change in the statistics of the experimental intensity profile. Indeed, as can be seen from Figure 7.7, records of the intensity above the significant wave height appear in a non-gaussian statistics.

Next the ratio of the extreme events and the kurtosis was studied with respect to the laser pump. The results are recorded in Figure 7.8. The main conclusion from this study is

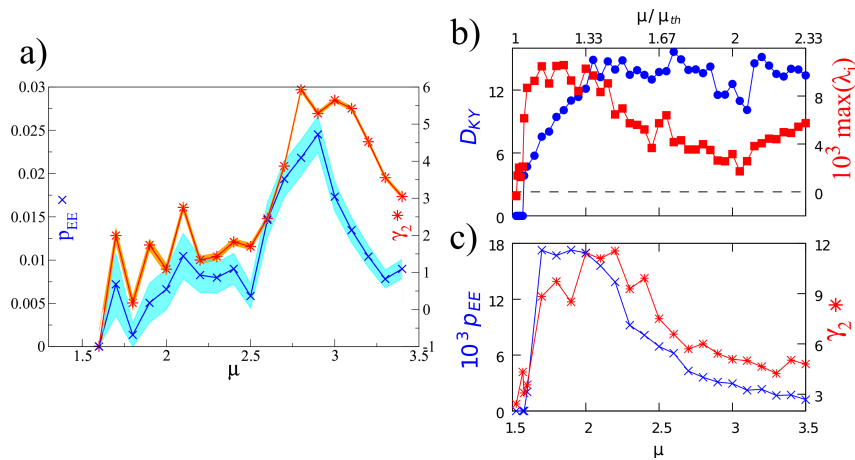


Figure 7.8: Emergence of extreme events and spatiotemporal chaos according to different observables. a) proportion of extreme events p_{EE} (\times) and excess kurtosis γ_2 ($*$) as function of pump parameter μ considering the height of the total intensity across the laser. b): largest Lyapunov exponent $\max(\lambda_i)$ (squares) and Kaplan-Yorke dimension D_{KY} (circles, from Eq.(??)) as function of pump parameter μ . c): proportion of extreme events p_{EE} (\times) and excess kurtosis γ_2 ($*$) as function of pump parameter μ considering the intensity of the local spatiotemporal maxima.

that the spatiotemporal chaos is prerequisite to observe the extreme events in this system, but increasing the complexity does not imply more extreme events. Then, coupling the statistical, spectral and chaos analyses we have identified the quasi-periodicity to be the route to the spatiotemporal chaos. Consequently, at the onset of the chaotic regime the dynamics is dominated by a spatiotemporal intermittency. It is also in this regime that the highest ratio of extreme event are recorded.



Conclusion and Perspectives

Throughout this report, I exposed an overview of my research activities since the end of my PhD thesis. These activities are widely dominated by the control of the localized dissipative structures which are ubiquitous in the nature. They are of a great interest for the scientific community since they can represent the macroscopic analogs of elementary physical particles. Thanks to this particle like behavior, mechanisms behind the formation, the interaction, and motion of localized structures remain a challenge. In particular, localized structures of physical systems in which losses must be balanced by energy injection are of particular interest. Among the ways to inject energy in dissipative systems, the one of harmonically modulating some parameters took a particular place in my activities. In this case, a resonance can be achieved by modulating a relevant parameter close to the twice of the natural frequency of the system. The parametrically excited localized structures are parametrized by one continuous parameter: the position which appears to be arbitrary. In the presence of another localized state, this position becomes a dynamic parameter. The theoretical study of the pair-interaction has given a law which decreases exponentially with the separation distance and it is attractive (repulsive) for two dissipative solitons that are in phase (out of phase). The majority of the dissipative structures can arise spontaneously above a given threshold. Conversely, in general, a dissipative solitary wave needs an external perturbation that falls into its basin of attraction. However, solitary wave generated parametrically coexist with homogeneous state, that is easier to excite. This homogeneous state always undergoes an instability leading to an irregular cascade of attractive solitons pair-interaction. The time scale of the formation of the non propagative multi-soliton state obeys a self-similar law, which has been derived from the two isolated soliton interaction law. Far from the position of its *center-of-mass*, parametric dissipative soliton can develop an unexpected non uniform phase profile. The asymptotic exponential decay of the amplitude has been shown to rule the transient dynamics before reaching the equilibrium configurations. The denominated phase shielding solitons have been also observed in two-dimension. These 2D solitons are characterized by always embedding in the same state all the possible stable configurations observed in 1D.

Since many years, my research activities have also focused in optical fiber systems. The modulational instability process has been intensively studied in this system. It is the result of an instability of a continuous wave solution of the generic model used to describe this system: the Nonlinear Schrödinger equation. The studies of this instability are generally based on the Fourier modal decomposition of the perturbation. When modulation instability is seeded by a localized initial condition, the latter approach fails and the stability may be addressed by means of an initial-value problem formalism. This approach allows us to compute the global (spatiotemporal) gain of the system which displays a gap in the band of standard modulationally unstable wavenumber. We also show through the determination of the group displacement that this band gap induced a region of wavenumbers where the group delay vanishes. In this region we have observed that pulses maintain their shape without distortion. However, any initial pulse with a wavenumber outside this region experiences many distortions. The same approach was also used in a setup where the ends of a fiber are coupled. The effect of the internal parity symmetric breaking coming from the slope of the dispersion curve has been included. The transition from convective to absolute instability was shown to coincide with the complex spatiotemporal evolution. An adequate tool to address the characterization of such complex dynamics is the computation of Lyapunov spectrum. Generally speaking the Lyapunov exponents are obtained by an algorithm based on the Gram-Schmidt orthonormalization. We have implemented this algorithm using parallel computing tools in a way that is free of the considered physical system. In the fiber ring cavity, for the first time, we were able to give a rigorous demonstration of the spatiotemporal chaos mediated by unstable breathing cavity soliton. In another cavity system, a semi-conductor laser with saturable absorber, the

spatiotemporal chaos has been shown to induce the emergence of extreme events.

Although the study of extreme events keeps attracting a great interest in nonlinear physics, the topic is now in the mature stage. From now on, the main concerns are not the evidence of these structures, but rather how to manipulate them. The question of their predicability has also arisen as a major concern. Before addressing these questions, their detection in a complex dynamical evolution is of crucial importance. In this scope, the experiment seems to be ahead of the theory. Indeed, many recent reports of fast measurement techniques leading to real time observation of extreme events. However, from a theoretical point of view, all these observations are the opportunity to consider many questions about the mechanisms of energy exchange upstream and downstream of the formation of extreme events. Fortunately, like Lyapunov exponents, the dynamical systems theory has many other performant tools that can be used to address these problems. In particular, *information theory* can be of special interest. In short- and midterm place it is in this direction that I would like to focus my activities.

List of publications

- [1] Tiofack, C., Coulibaly, S., Taki, M., De Bièvre, S., and Dujardin, G. Periodic modulations controlling kuznetsov-ma soliton formation in nonlinear schrödinger equations. *Physics Letters A* **381** (2017), 1999.
- [2] Ouali, M., Coulibaly, S., Taki, M., and Tlidi, M. Extended and localized hopf-turing mixed-mode in non-instantaneous kerr cavities. *Optics Express* **25** (2017), 4714.
- [3] Liu, Z., Ouali, M., Coulibaly, S., Clerc, M., Taki, M., and Tlidi, M. Characterization of spatiotemporal chaos in a kerr optical frequency comb and in all fiber cavities. *Opt. Lett.* **42** (2017), 1063.
- [4] Liu, Z., Coulibaly, S., Taki, M., and Akhmediev, N. Kerr frequency combs and triangular spectra. *Opt. Lett.* **42** (2017), 2126.
- [5] Hontinfinde, R., Coulibaly, S., Megret, P., Taki, M., and Wuilpart, M. Nondestructive distributed measurement of supercontinuum generation along highly nonlinear optical fibers. *Opt. Lett.* **42** (2017), 1716.
- [6] Ferré, M. A., Clerc, M. G., Coulibaly, S., and Rojas, René G. and Tlidi, M. Localized structures and spatiotemporal chaos: comparison between the driven damped sine-gordon and the lugiato-lefever model. *Eur. Phys. J. D* **71** (2017), 172.
- [7] Drouzi, L., Coulibaly, S., Taki, M., and Laabidi, K. Group-velocity-mismatch-induced transition from absolute to convective instability in birefringent fibers. *Phys. Rev. A* **95** (2017), 063826.
- [8] Coulibaly, S., Clerc, M., Selmi, F., and Barbay, S. Extreme events following bifurcation to spatiotemporal chaos in a spatially extended microcavity laser. *Phys. Rev. A* **95** (2017), 023816.
- [9] Clerc, M., Ferré, M., Coulibaly, S., Rojas, R., and Tlidi, M. Chimera-like states in an array of coupled-waveguide resonators. *Opt. Lett.* **42** (2017), 2906.
- [10] Tiofack, C. G., Coulibaly, S., and Taki, M. Generation of multiple compression points for akhmediev breather with periodic coefficients In "Roadmap on optical rogue waves and extreme events" edited by N. Akhmediev. *Journal of Optics* **18** (2016), 063001.
- [11] Selmi, F., Coulibaly, S., Loghmari, Z., Sagnes, I., Beaudoin, G., Clerc, M. G., and Barbay, S. Spatiotemporal chaos induces extreme events in an extended microcavity laser. *Phys. Rev. Lett.* **116** (2016), 013901.
- [12] Louvergneaux, E., Odent, V., Coulibaly, S., Bortolozzo, U., and Residori, S. Control and generation of drifting patterns by asymmetrical fourier filtering. *Phys. Rev. E* **93** (2016), 010201.

- [13] Liu, Z., Leo, F., Coulibaly, S., and Taki, M. Secondary instabilities and chaos in optical ring cavities. *Springer Proceedings in Physics* **173** (2016), 167.
- [14] Clerc, M., Coulibaly, S., Ferré, M., García-Ñustes, M., and Rojas, R. Chimera-type states induced by local coupling. *Phys. Rev. E* **93** (2016), 052204.
- [15] Tiofack, C., Coulibaly, S., Taki, M., De Bièvre, S., and Dujardin, G. Comb generation using multiple compression points of peregrine rogue waves in periodically modulated nonlinear schrödinger equations. *Phys. Rev. A* **92** (2015), 043837.
- [16] León, A. O., Clerc, M. G., and Coulibaly, S. Traveling pulse on a periodic background in parametrically driven systems. *Phys. Rev. E* **91** (2015), 050901.
- [17] Coulibaly, S., Louvergneaux, E., Taki, M., and Brevdo, L. Spatiotemporal wave-train instabilities in nonlinear schrödinger equation: revisited. *Eur. Phys. J. D* **69** (2015), 186.
- [18] Clerc, M. G., Coulibaly, S., Laroze, D., León, A. O., and Núñez, A. S. Alternating spin-polarized current induces parametric resonance in spin valves. *Phys. Rev. B* **91** (2015), 224426.
- [19] Clerc, M., Coulibaly, S., Garcia-Ñustes, M., and Zárate, Y. Transverse phase shielding solitons in the degenerated optical parametric oscillator. *Opt. Commun.* **354** (2015), 163.
- [20] Clerc, M., Coulibaly, S., del Campo, F., Garcia-Nustes, M., Louvergneaux, E., and Wilson, M. Recurrent noise-induced phase singularities in drifting patterns. *Phys. Rev. E* **92** (2015), 050902.
- [21] Liu, Z., Leo, F., Coulibaly, S., and Taki, M. Secondary instabilities in all fiber ring cavities. *Phys. Rev. A* **90** (2014), 033837.
- [22] León, A. O., Clerc, M. G., and Coulibaly, S. Dissipative structures induced by spin-transfer torques in nanopillars. *Phys. Rev. E* **89** (2014), 022908.
- [23] Coulibaly, S., Taki, M., and Tlidi, M. Universal power law for front propagation in all fiber resonators. *Optics Express* **22** (2014), 483.
- [24] Tlidi, M., Bahloul, L., Cherbi, L., Hariz, A., and Coulibaly, S. Drift of dark cavity solitons in a photonic-crystal fiber resonator. *Phys. Rev. A* **88** (2013), 035802.
- [25] Clerc, M. G., Garcia-Ñustes, M. A., Zárate, Y., and Coulibaly, S. Phase shielding soliton in parametrically driven systems. *Phys. Rev. E* **87** (2013), 052915.
- [26] Clerc, M. G., Fernández-Oto, C., and Coulibaly, S. Pinning-depinning transition of fronts between standing waves. *Phys. Rev. E* **87** (2013), 012901.
- [27] Urzagasti, D., Laroze, D., Clerc, M., Coulibaly, S., and Pleiner, H. Two-soliton precession state in a parametrically driven magnetic wire. *Journal of Applied Physics* **111** (2012), 07D111.
- [28] Coulibaly, S., Liu, Z., Taki, M., and Agrawal, G. Parametric gain control of a pulse in birefringent photonic crystal fibers. *Phys. Rev. A* **86** (2012), 033802.
- [29] Clerc, M., Coulibaly, S., and Laroze, D. Localized waves in a parametrically driven magnetic nanowire. *Europhys. Lett.* **97** (2012), 30006.

- [30] Coulibaly, S., Taki, M., and Akhmediev, N. Convection-induced stabilization of optical dissipative solitons. *Opt. Lett.* **36** (2011), 4410.
- [31] Clerc, M. G., Coulibaly, S., Garcia-Nustes, M. A., and Zárata, Y. Dissipative localized states with shieldlike phase structure. *Phys. Rev. Lett.* **107** (2011), 254102.
- [32] Clerc, M., Coulibaly, S., Gordillo, L., Mujica, N., and Navarro, R. Coalescence cascade of dissipative solitons in parametrically driven systems. *Phys. Rev. E* **84** (2011), 036205.
- [33] Clerc, M., Coulibaly, S., and Laroze, D. Localized states and non-variational ising-bloch transition of a parametrically driven easy-plane ferromagnetic wire. *Physica D* **239** (2010), 72.
- [34] Clerc, M., Coulibaly, S., and Laroze, D. Interaction law of 2d localized precession states. *Europhys. Lett.* **90** (2010), 38005.
- [35] Clerc, M., Coulibaly, S., Mujica, N., Navarro, R., and Sauma, T. Soliton pair interaction law in parametrically driven newtonian fluid. *Phil. Trans. R. Soc. A* **367** (2009), 3213.
- [36] Clerc, M., Coulibaly, S., and Laroze, D. Parametrically driven instability in quasi-reversal systems. *Int. J. Bifurcation Chaos* **19** (2009), 3525.
- [37] Clerc, M., Coulibaly, S., and Laroze, D. Nonvariational isingbloch transition in parametrically driven systems. *Int. J. Bifurcation Chaos* **19** (2009), 2717.
- [38] Coulibaly, S., Durniak, C., and Taki, M. Spatial dissipative solitons under convective and absolute instabilities in optical parametric oscillators. *Lect. Notes Phys.* **751** (2008), 261.
- [39] Clerc, M., Coulibaly, S., and Laroze, D. Localized states beyond the asymptotic parametrically driven amplitude equation. *Phys. Rev. E* **77** (2008), 056209.
- [40] Brazhnyi, V., Konotop, V., Coulibaly, S., and Taki, M. Field patterns in periodically modulated optical parametric amplifiers and oscillators. *Chaos* **17**, 3 (2007), 037111.

Bibliography

- [Agrawal, 2013] Agrawal, G. (2013). *Nonlinear Fiber Optics (Fifth Edition)*. Academic Press, Boston.
- [Antikainen et al., 2012] Antikainen, A., Erkintalo, M., Dudley, J. M., and Genty, G. (2012). On the phase-dependent manifestation of optical rogue waves. *Nonlinearity*, 25(7):R73.
- [Arecchi et al., 2011] Arecchi, F. T., Bortolozzo, U., Montina, A., and Residori, S. (2011). Granularity and inhomogeneity are the joint generators of optical rogue waves. *Phys. Rev. Lett.*, 106:153901.
- [Ballarini et al., 2013] Ballarini, D., De Giorgi, M., Cancellieri, E., Houdré, R., Giacobino, E., Cingolani, R., Bramati, A., Gigli, G., and Sanvitto, D. (2013). All-optical polariton transistor. *Nature Communications*, 4:1778.
- [Barashenkov et al., 1991] Barashenkov, I., Bogdan, M., and Korobov, V. (1991). Stability diagram of the phase-locked solitons in the parametrically driven, damped nonlinear schrödinger equation. *EPL (Europhysics Letters)*, 15(2):113.
- [Benjamin and Ursell, 1954] Benjamin, T. B. and Ursell, F. (1954). The stability of the plane free surface of a liquid in vertical periodic motion. In *Proceedings of the Royal Society of London A: Mathematical, Physical and Engineering Sciences*, volume 225, pages 505–515. The Royal Society.
- [Bennett et al., 2002] Bennett, M., Schatz, M. F., Rockwood, H., and Wiesenfeld, K. (2002). Huygens's clocks. *Proceedings: Mathematical, Physical and Engineering Sciences*, 458(2019):563–579.
- [Bers, 1973] Bers, A. (1973). *Theory of absolute and convective instabilities*, In *International Congress on Waves and Instabilities in Plasmas*. Auer, G., Cap, F. (eds.), Innsbruck (Austria).
- [Binder, 1973] Binder, K. (1973). Time-dependent ginzburg-landau theory of nonequilibrium relaxation. *Phys. Rev. B*, 8:3423.
- [Birkholz et al., 2013] Birkholz, S., Nibbering, E. T. J., Brée, C., Skupin, S., Demircan, A., Genty, G., and Steinmeyer, G. (2013). Spatiotemporal rogue events in optical multiple filamentation. *Phys. Rev. Lett.*, 111:243903.
- [Bonatto et al., 2011] Bonatto, C., Feyereisen, M., Barland, S., Giudici, M., Masoller, C., Leite, J. R. R., and Tredicce, J. R. (2011). Deterministic optical rogue waves. *Phys. Rev. Lett.*, 107:053901.
- [Bosco et al., 2013] Bosco, A. K. D., Wolfersberger, D., and Sciamanna, M. (2013). Extreme events in time-delayed nonlinear optics. *Opt. Lett.*, 38(5):703–705.
- [Braun and Kivshar, 2004] Braun, O. M. and Kivshar, Y. S. (2004). *The Frenkel-Kontorova Model: Concepts, Methods, and Applications*. Springer-Verlag Berlin Heidelberg.

- [Brevdo, 1988] Brevdo, L. (1988). A study of absolute and convective instabilities with an application to the eady model. *Geophysical & Astrophysical Fluid Dynamics*, 40(1-2):1–92.
- [Briggs, 1964] Briggs, R. (1964). *Electron-Stream Interaction with Plasmas*. Research monograph. MIT Press.
- [Cerdeira and Tirapegui, 1998] Cerdeira, E. and Tirapegui, E. (1998). Faraday's instability in viscous fluid. *Journal of Fluid Mechanics*, 368:195–228.
- [Chen et al., 2012] Chen, Z., Segev, M., and Christodoulides, D. N. (2012). Optical spatial solitons: historical overview and recent advances. *Reports on Progress in Physics*, 75(8):086401.
- [Clerc et al., 2009] Clerc, M., Coulibaly, S., Mujica, N., Navarro, R., and Sauma, T. (2009). Soliton pair interaction law in parametrically driven newtonian fluid. *Philosophical Transactions of the Royal Society of London A: Mathematical, Physical and Engineering Sciences*, 367(1901):3213–3226.
- [Clerc et al., 2016] Clerc, M. G., González-Cortés, G., and Wilson, M. (2016). Extreme events induced by spatiotemporal chaos in experimental optical patterns. *Opt. Lett.*, 41(12):2711–2714.
- [Cross and Hohenberg, 1993] Cross, M. C. and Hohenberg, P. C. (1993). Pattern formation outside of equilibrium. *Rev. Mod. Phys.*, 65:851–1112.
- [Denardo et al., 1990] Denardo, B., Wright, W., Putterman, S., and Larraza, A. (1990). Observation of a kink soliton on the surface of a liquid. *Physical review letters*, 64(13):1518.
- [Devonshire, 1954] Devonshire, A. (1954). Theory of ferroelectrics. *Advances in physics*, 3(10):85–130.
- [Drazin and Reid, 2004] Drazin, P. G. and Reid, W. H. (2004). *Hydrodynamic stability*. Cambridge university press.
- [Dudley et al., 2008] Dudley, J. M., Genty, G., and Eggleton, B. J. (2008). Harnessing and control of optical rogue waves insupercontinuum generation. *Opt. Express*, 16(6):3644–3651.
- [Faraday, 1831] Faraday, M. (1831). On a peculiar class of acoustical figures; and on certain forms assumed by groups of particles upon vibrating elastic surfaces. *Philosophical Transactions of the Royal Society of London*, 121:299–340.
- [Firth, 2010] Firth, W. (2010). Temporal cavity solitons: Buffering optical data. *Nat Photon*, 4(7):415.
- [Ginzburg and Landau, 1950] Ginzburg, V. and Landau, L. (1950). On the theory of superconductivity. *Zh. Eksp. Teor. Fiz.*, 20:1064 [English translation in: L. D. Landau, "Collected papers," Oxford: Pergamon Press (1965), 546.].
- [Gordillo, 2012] Gordillo, L. (2012). *Non-propagating hydrodynamic solitons in a quasi-one dimensional free surface subject to vertical vibrations*. PhD dissertation, Universidad de Chile.
- [Grelu, 2015] Grelu, P. (2015). *Nonlinear optical cavity dynamics: from microresonators to fiber lasers*. John Wiley & Sons.

- [Haken, 1978] Haken, H. (1978). *Synergetics*. Springer-Verlag, Berlin.
- [Huygens, 1669] Huygens, C. (1669). Instructions concerning the use of pendulum-watches, for finding the longitude at sea. *Philosophical Transactions*, 4(45-56):937–976.
- [Ikeda, 1979] Ikeda, K. (1979). Multiple-valued stationary state and its instability of the transmitted light by a ring cavity system. *Optics communications*, 30(2):257–261.
- [Kaneko, 1986] Kaneko, K. (1986). *Collapse of tori and genesis of chaos in dissipative systems*. World Scientific.
- [Kaup and Newell, 1978] Kaup, D. and Newell, A. (1978). Theory of nonlinear oscillating dipolar excitations in one-dimensional condensates. *Physical Review B*, 18(10):5162.
- [Kevorkian and Cole, 1996] Kevorkian, J. and Cole, J. (1996). Multiple scale and singular perturbation problems. *Applied Mathematical Sciences*, 114.
- [Kharif and Pelinovsky, 2003] Kharif, C. and Pelinovsky, E. (2003). Physical mechanisms of the rogue wave phenomenon. *European Journal of Mechanics - B/Fluids*, 22(6):603 – 634.
- [Kibler et al., 2010] Kibler, B., Fatome, J., Finot, C., Millot, G., Dias, F., Genty, G., Akhmediev, N., and Dudley, J. M. (2010). The peregrine soliton in nonlinear fibre optics. *Nat Phys*, 6(10):790–795.
- [Kittel, 1949] Kittel, C. (1949). Physical theory of ferromagnetic domains. *Reviews of modern Physics*, 21(4):541.
- [Kosevich et al., 1990] Kosevich, A. M., Ivanov, B., and Kovalev, A. (1990). Magnetic solitons. *Physics Reports*, 194(3-4):117.
- [Kovalsky et al., 2011] Kovalsky, M. G., Hnilo, A. A., and Tredicce, J. R. (2011). Extreme events in the ti:sapphire laser. *Opt. Lett.*, 36(22):4449–4451.
- [Kubicek and Marek, 1983] Kubicek, M. and Marek, M. (1983). *Computational Methods in Bifurcation Theory and Dissipative Structures*. Springer-Verlag.
- [Kuramoto, 1984] Kuramoto, Y. (1984). *Chemical Oscillations, Waves, and Turbulence*. 3Island Press.
- [Landau and Lifshitz, 1940] Landau, L. and Lifshitz, E. (1940). *Statistical Physics*. Clarendon Press.
- [Landau and Lifshitz, 1966] Landau, L. and Lifshitz, E. (1966). *Micanipue* (trans. from russian). *MIR Moscow*.
- [Larrazza and Putterman, 1984] Larrazza, A. and Putterman, S. (1984). Theory of nonpropagating hydrodynamic solitons. *Physics Letters A*, 103(1-2):15–18.
- [Lecaplain et al., 2012] Lecaplain, C., Grelu, P., Soto-Crespo, J. M., and Akhmediev, N. (2012). Dissipative rogue waves generated by chaotic pulse bunching in a mode-locked laser. *Phys. Rev. Lett.*, 108:233901.
- [Liu et al., 2005] Liu, Y., Sellmyer, D., and Shindo, D. (2005). *Handbook of Advanced Magnetic Materials vol. 1*. Springer.

- [Mikeska, 1978] Mikeska, H. (1978). Solitons in a one-dimensional magnet with an easy plane. *Journal of Physics C: Solid State Physics*, 11(1):L29.
- [Miles, 1984] Miles, J. W. (1984). Parametrically excited solitary waves. *Journal of Fluid Mechanics*, 148:451–460.
- [Montina et al., 2009] Montina, A., Bortolozzo, U., Residori, S., and Arecchi, F. T. (2009). Non-gaussian statistics and extreme waves in a nonlinear optical cavity. *Phys. Rev. Lett.*, 103:173901.
- [Morales and Lee, 1974] Morales, G. and Lee, Y. (1974). Ponderomotive-force effects in a nonuniform plasma. *Physical Review Letters*, 33(17):1016.
- [Mussot et al., 2009] Mussot, A., Kudlinski, A., Kolobov, M., Louvergneaux, E., Douay, M., and Taki, M. (2009). Observation of extreme temporal events in cw-pumped supercontinuum. *Opt. Express*, 17(19):17010–17015.
- [Newell and Moloney, 1992] Newell, A. C. and Moloney, J. V. (1992). *Nonlinear optics*. Addison-Wesley.
- [Nicolis and Nicolis, 2012] Nicolis, G. and Nicolis, C. (2012). *Foundations of complex systems: emergence, information and prediction*. World Scientific, Singapore.
- [Nicolis and Prigogine, 1977] Nicolis, G. and Prigogine, I. (1977). *Self-organization in nonequilibrium systems*. Wiley, New York.
- [Nozaki and Bekki, 1984] Nozaki, K. and Bekki, N. (1984). Solitons as attractors of a forced dissipative nonlinear schrödinger equation. *Physics Letters A*, 102(9):383–386.
- [Onorato et al., 2013] Onorato, M., Residori, S., Bortolozzo, U., Montina, A., and Arecchi, F. (2013). Rogue waves and their generating mechanisms in different physical contexts. *Physics Reports*, 528(2):47 – 89.
- [Ott, 2002] Ott, E. (2002). *Chaos in Dynamical Systems*. Cambridge University Press.
- [Pierangeli et al., 2015] Pierangeli, D., Di Mei, F., Conti, C., Agranat, A. J., and DelRe, E. (2015). Spatial rogue waves in photorefractive ferroelectrics. *Phys. Rev. Lett.*, 115:093901.
- [Pisarchik et al., 2011] Pisarchik, A. N., Jaimes-Reátegui, R., Sevilla-Escoboza, R., Huerta-Cuellar, G., and Taki, M. (2011). Rogue waves in a multistable system. *Phys. Rev. Lett.*, 107:274101.
- [Pismen, 2006] Pismen, L. (2006). *Patterns and Interfaces in Dissipative Dynamics*. Springer Series in Synergetics. Springer Berlin Heidelberg.
- [Rand, 1994] Rand, R. H. (1994). *Topics in nonlinear dynamics with computer algebra*, volume 1. CRC Press.
- [Randoux and Suret, 2012] Randoux, S. and Suret, P. (2012). Experimental evidence of extreme value statistics in raman fiber lasers. *Opt. Lett.*, 37(4):500–502.
- [Rossi et al., 2008] Rossi, F., Ristori, S., Rustici, M., Marchettini, N., and Tiezzi, E. (2008). Dynamics of pattern formation in biomimetic systems. *Journal of Theoretical Biology*, 255(4):404.

- [Russell, 1844] Russell, J. S. (1844). Report on waves. In *14th meeting of the British Association for the Advancement of Science*, volume 311, page 1844.
- [Schrödinger, 1992] Schrödinger, E. (1992). *What is life?: With mind and matter and autobiographical sketches*. Cambridge University Press.
- [Scott et al., 2006] Scott, A. et al. (2006). *Encyclopedia of nonlinear science*. Routledge.
- [Selmi et al., 2016] Selmi, F., Coulibaly, S., Loghmari, Z., Sagnes, I., Beaudoin, G., Clerc, M. G., and Barbay, S. (2016). Spatiotemporal chaos induces extreme events in an extended micro-cavity laser. *Phys. Rev. Lett.*, 116:013901.
- [Solli et al., 2007] Solli, D. R., Ropers, C., Koonath, P., and Jalali, B. (2007). Optical rogue waves. *Nature*, 450(7172):1054–1057.
- [Turing, 1952] Turing, A. (1952). The chemical theory of 185. morphogenesis. *Phil. Trans. Roy. Soc. B*, 7.
- [Umeki, 1991] Umeki, M. (1991). Parametric dissipative nonlinear schrödinger equation. *Journal of the Physical Society of Japan*, 60(1):146–167.
- [Ward et al., 2000] Ward, H., Ouarzazi, M., Taki, M., and Glorieux, P. (2000). Influence of walkoff on pattern formation in nondegenerate optical parametric oscillators. *Physical Review E*, 63(1):016604.
- [Wu et al., 1984] Wu, J., Keolian, R., and Rudnick, I. (1984). Observation of a nonpropagating hydrodynamic soliton. *Physical Review Letters*, 52(16):1421.
- [Yates, 2012] Yates, F. E. (2012). *Self-organizing systems: The emergence of order*. Springer Science & Business Media.
- [Zabusky and Kruskal, 1965] Zabusky, N. J. and Kruskal, M. D. (1965). Interaction of "solitons" in a collisionless plasma and the recurrence of initial states. *Physical review letters*, 15(6):240.
- [Zhang and Vinals, 1997] Zhang, W. and Vinals, J. (1997). Pattern formation in weakly damped parametric surface waves. *Journal of Fluid Mechanics*, 336:301–330.
- [Zharnitsky et al., 1998] Zharnitsky, V., Mitkov, I., and Levi, M. (1998). Parametrically forced sine-gordon equation and domain wall dynamics in ferromagnets. *Physical Review B*, 57(9):5033.

Selected publications

Optics Letters

Characterization of spatiotemporal chaos in a Kerr optical frequency comb and in all fiber cavities

Z. LIU,¹ M. OUALI,¹ S. COULIBALY,^{1,*} M. G. CLERC,² M. TAKI,¹ AND M. TLIDI³

¹Université de Lille, CNRS, UMR 8523-PhLAM-Physique des Lasers Atomes et Molécules, F-59000 Lille, France

²Departamento de Física, FCFM, Universidad de Chile, Casilla 487-3, Santiago, Chile

³Optique Nonlinéaire Théorique, Université Libre de Bruxelles (U.L.B.), CP 231, Campus Plaine, B-1050 Bruxelles, Belgium

*Corresponding author: saliya.coulibaly@univ-lille1.fr

Received 28 December 2016; revised 10 February 2017; accepted 13 February 2017; posted 14 February 2017 (Doc. ID 283776); published 3 March 2017

Complex spatiotemporal dynamics have been a subject of recent experimental investigations in optical frequency comb microresonators and in driven fiber cavities with Kerr-type media. We show that this complex behavior has a spatiotemporal chaotic nature. We determine numerically the Lyapunov spectra, allowing us to characterize different dynamical behavior occurring in these simple devices. The Yorke–Kaplan dimension is used as an order parameter to characterize the bifurcation diagram. We identify a wide regime of parameters where the system exhibits a coexistence between the spatiotemporal chaos, the oscillatory localized structure, and the homogeneous steady state. The destabilization of an oscillatory localized state through radiation of counter-propagating fronts between the homogeneous and the spatiotemporal chaotic states is analyzed. To characterize better the spatiotemporal chaos, we estimate the front speed as a function of the pump intensity. © 2017 Optical Society of America

OCIS codes: (070.5753) Resonators; (190.4370) Nonlinear optics, fibers; (190.3100) Instabilities and chaos; (190.5530) Pulse propagation and temporal solitons.

<https://doi.org/10.1364/OL.42.001063>

Experiments supported by numerical simulations of driven cavities such as whispering-gallery-mode microresonators leading to optical frequency comb generation have demonstrated the existence of complex spatiotemporal dynamics [1]. Similar complex dynamics have been observed in all-fiber cavities [2–4]. In most of these studies, complex behaviors are characterized by a power spectrum [1], filtering spatiotemporal diagrams [4], embedding dimension, and time series analysis [2,3]. However, these tools are inadequate to distinguish between spatiotemporal chaos, low dimensional chaos, and turbulence. A classification of these phenomena has been reported in the literature (see for instance [5–11]). In the case of spatiotemporal chaos, the Lyapunov spectrum has a continuous

set of positive values. This matches the definition that has been proposed in [5,7]. In the case of a low dimensional chaos, the Lyapunov spectrum possesses a discrete set of positive values. However, the turbulence or weak turbulence is characterized by a power law cascade of a scalar quantity such as energy and norm [12]. On the basis of the Lyapunov spectrum, we cannot conclude that the system develops a turbulence.

In this Letter, we characterize the complex behavior reported in the paradigmatic Lugiato–Lefever equation (LLE, [13]) that describes Kerr optical frequency combs and fiber cavities. For this purpose, we use a rigorous tools of dynamical systems theory. We show that this complex behavior has a spatiotemporal chaotic nature. We estimate the Lyapunov spectra. The Yorke–Kaplan dimension (D_{YK}) is used as an order parameter to establish the bifurcation diagram of the spatiotemporal chaos. In addition, we show that the spatiotemporal chaos, the oscillatory localized state and the homogeneous steady state (HSS) can coexist in a finite range of the pumping intensity. The destabilization of an oscillatory localized state through radiation of counter-propagating fronts between the HSS and the spatiotemporal chaotic state is also discussed by estimating the front speed as a function of the pump intensity.

Driven Kerr cavities with a high Fresnel number—assuming that the cavity is much shorter than the diffraction and the nonlinearity spatial scales—is described in the mean field limit by the LLE [13]. This equation has been extended to model both fiber cavities [14,15] and optical frequency comb generation [16–18], in which the diffraction is replaced by dispersion. This model reads

$$\frac{\partial \psi}{\partial t} = S - (\alpha + i\delta)\psi + \frac{i}{2} \frac{\partial^2 \psi}{\partial \tau^2} + i|\psi|^2\psi, \quad (1)$$

where $\psi(t, \tau)$ is the normalized slowly varying envelope of the electric field that circulates within the cavity, and S is the amplitude of the injected field which is real and constant. The time variable t corresponds to the slow evolution of ψ over successive round-trips. τ accounts for the fast dynamics that describes how the electric field envelope changes along the fiber [14–16]. The parameters α and δ are the cavity losses,

and the cavity detuning, respectively. In addition, Eq. (1) has been derived in the context of left-handed materials [19]. Note that Eq. (1) has been derived in early reports to describe the plasma driven by a radio frequency field [20,21] and the condensate in the presence of an applied ac field [22].

The model, Eq. (1), supports stationary localized [23] and self-pulsating localized [24] structures. In the conservative limit, $(\alpha, S) \rightarrow (0, 0)$, localized structures have analytical solutions [25–28]. It has been also shown that, in this limit, localized structures can exhibit regular time oscillations and display a complex behavior [25–27]. An example of complex spatiotemporal behavior is plotted in the $\tau - t$ map of Fig. 1(a). The time evolution of the field amplitude that circulates inside the cavity exhibits large amplitude localized pulses. These pulses have irregular distribution along the τ coordinate [see Fig. 1(a)]. The characterization of this behavior can be achieved by means of Lyapunov exponents, which provide an information about the sensitivity of close initial conditions [7]. When the largest Lyapunov exponent is positive, the system develops chaos, but not necessarily a spatiotemporal chaos. To distinguish between these two complex dynamical behaviors, it is necessary to compute the Lyapunov spectra composed by a set of exponents [5–7]. Spatiotemporal chaos has a Lyapunov spectrum with a *continuous* set of positive values. In contrast, chaos possesses a Lyapunov spectrum with a discrete set of positive values. The Lyapunov exponents is denoted by $\{\lambda_i\}$, where i labels the exponents ($i = 1, \dots, N$) and $\lambda_p \leq \lambda_q$ ($p \geq q$). By using the strategy proposed in [29,30], we compute numerically the Lyapunov spectrum for large N . The numerical simulations are obtained by using periodic boundary conditions that are compatible with both Kerr optical frequency combs and fiber cavity geometries. Figure 1(b) shows a typical continuous Lyapunov spectrum. Hence, we infer that the complex dynamical behavior shown in Fig. 1(a) is a spatiotemporal chaos.

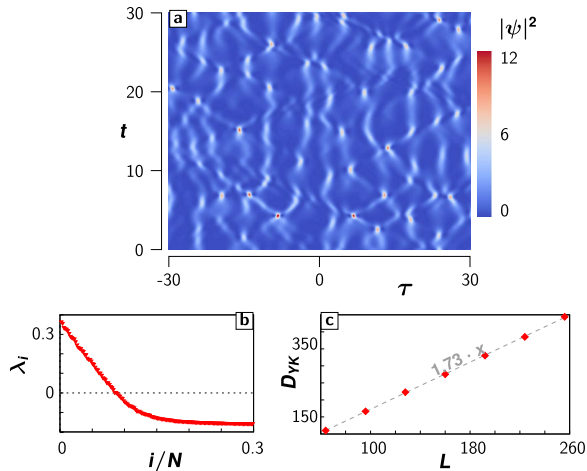


Fig. 1. Spatiotemporal chaos. (a) $\tau - t$ map shows a complex spatiotemporal behavior obtained by numerical simulation of Eq. (1) with $\alpha = 0.16$, $\delta = 1$, and $S^2 = 0.16$ with 512 grid points. (b) Corresponding Lyapunov spectrum, and (c) Yorke–Kaplan dimension as a function of the system size L is indicated by the diamond red points. $L = 512\Delta\tau$ with $\Delta\tau$ is the step-size integration. The linear growth of D_{YK} dimension is fitted by a slope of 1.73, as shown by the gray dashed line.

The main feature of the Lyapunov spectra is that they are proportional to the physical system size. This implies that the upper limit of the strange attractor dimension of spatiotemporal chaos—the Kaplan–Yorke dimension (D_{YK})—is an extensive quantity that increases with the physical system size [6]. This latter quantity provides an information on the level of the strange attractor complexity and is defined by [31]

$$D_{YK} \equiv p + \frac{\sum_{i=1}^p \lambda_i}{\lambda_{p+1}}, \quad (2)$$

where p is the largest integer that satisfies $\sum_{i=1}^p \lambda_i > 0$. Figure 1(c) displays D_{YK} as a function of the number of discretization points, which shows that this dimension is indeed an extensive physical quantity as it linearly increases with the system size. Therefore, as one increases the system size, the dimension of the strange attractor grows proportionally.

To establish the bifurcation diagram of the spatiotemporal chaos, we fix the detuning and the dissipation values, and we numerically estimate D_{YK} by varying the pumping intensity. The initial condition consists of a single peak localized structure. The summary of the results is illustrated in Fig. 2. When increasing the pump intensity, the LLE has a zero Yorke–Kaplan dimension, i.e., $D_{YK} = 0$ until the system reaches $S^2 \equiv S_+^2$. For $S^2 > S_+^2$, the system exhibits a transition toward a spatiotemporal chaos, i.e., $D_{YK} > 0$. This behavior lasts for large pumping intensity values. When decreasing S^2 , the spatiotemporal chaos persists down to the point $S^2 \equiv S_-^2$, as shown in Fig. 2. From this figure, we clearly see a hysteresis loop involving a spatiotemporal chaos, a pulsating localized structure, and a HSS in the range $S_-^2 < S^2 < S_+^2$. The inset in Fig. 2 shows the continuous Lyapunov spectra for different values of the pump intensity. Remarkably, the middle panel of the inset shows two Lyapunov spectra (Γ_2 and Γ_3) obtained for the same parameters values indicating the coexistence of two qualitatively different dynamical behaviors.

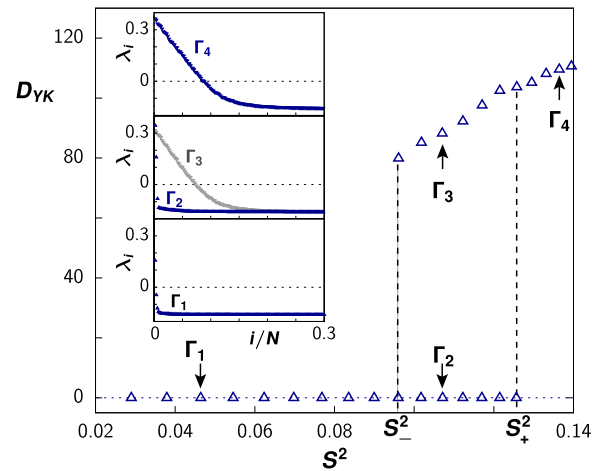


Fig. 2. Bifurcation diagram of spatiotemporal chaos showing the Yorke–Kaplan dimension, D_{YK} , as a function of the intensity of pumping obtained by numerical simulations of Eq. (1). The insets account for the Lyapunov spectra obtained for four values of the pumping intensity indicated by the symbol Γ_j ($j = 1, 2, 3, 4$). The parameters are $\delta = 1$, and $\alpha = 0.16$. The grid points is 512. The spectra are composed of $N = 496$ exponents.

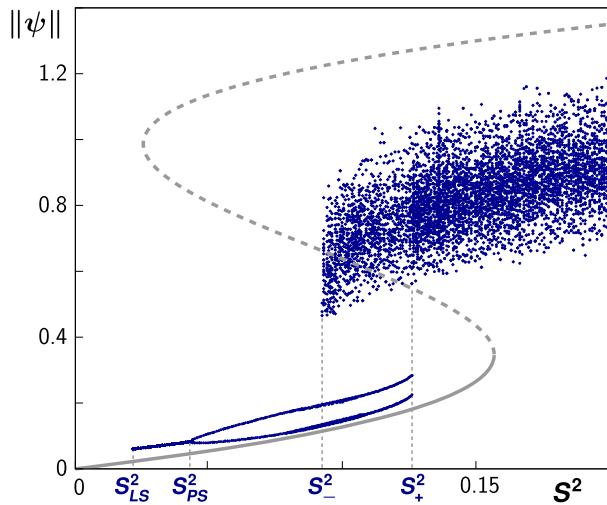


Fig. 3. Bifurcation diagram of model Eq. (1). The total intracavity intensity $\|\psi\|$ versus the pump intensity S^2 with $\delta = 1$, and $\alpha = 0.16$. The continuous and dashed thick gray lines point out the stable and unstable HSS, respectively. The continuous blue lines indicate the extrema of the total intracavity intensity $\|\psi\|$ of localized states. The cloud of blue scattered points accounts for the spatiotemporal chaotic state. Note that the horizontal graduation unit is equal to 0.05.

In what follows, we establish a bifurcation diagram showing a coexistence between the spatiotemporal chaos, the oscillatory localized structure, and the HSS. In order to show different operating regimes, the total intracavity field amplitude $\|\psi\| \equiv \int |\psi(t, \tau)|^2 d\tau$ as a function of the pumping intensity is shown in the bifurcation diagram Fig. 3. The upper (lower) HSS branch indicated by a dashed (solid) gray line is modulationally unstable (stable) [13]. For small pumping intensity, the system has a stationary stable localized state in the range $S_{LS}^2 < S^2 < S_{PS}^2$ (see Fig. 3). When increasing the pumping intensity, the localized state becomes self-pulsating in the range $S_{PS}^2 \leq S^2 < S_+^2$. When further increasing S^2 , the system exhibits spatiotemporal chaos. When decreasing S^2 , the spatiotemporal chaos persists down to S_-^2 . As in the bifurcation diagram of D_{YK} (see Fig. 2), the system presents an hysteresis loop involving three different robust states: HSS, pulsating localized structures, and spatiotemporal chaos.

It is well known that model (1) exhibits radiation from a localized state of two counter-propagating fronts between the homogeneous and the complex spatiotemporal states [32]. An example of this behavior is depicted in the $\tau - t$ map shown in Fig. 4(a). To characterize this transition, we estimate numerically the front speed. Figure 4(b) shows the front speed as a function of the pump intensity in the vicinity of the instability associated with localized states. Right and left fronts propagate with almost the same speed. As the pumping intensity is increased, the front speed continues to increase until the system reaches the lower limit point of bistable HSSs. Similar behavior has been reported in pattern forming systems where the front propagates between a HSS and a periodic pattern [33–35], between either of the two HSSs [36,37], or even between a HSS and the spatiotemporal intermittency [38].

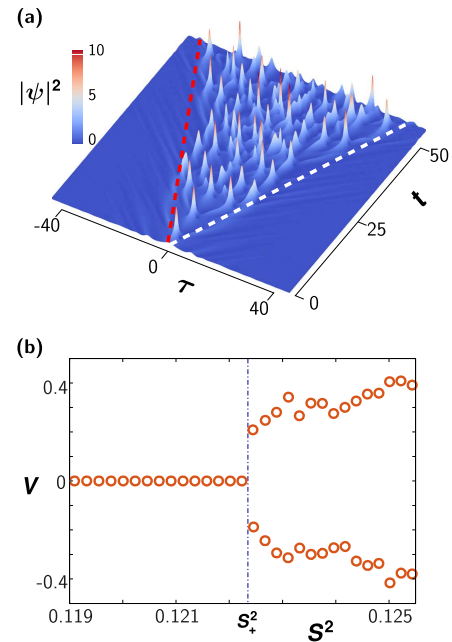


Fig. 4. Front radiation from an oscillating unstable localized state. (a) Spatiotemporal evolution of oscillatory localized structures obtained from the numerical simulation of Eq. (1). The parameters are $S^2 = 0.1225$, $\delta = 1$, and $\alpha = 0.16$. The dashed lines mark a separation between the chaotic and the homogeneous background. From these lines, one can determine the front speed. (b) Front speed V as a function of the pump intensity obtained for $\delta = 1$ and $\alpha = 0.16$.

From a practical point of view, a driven ring cavity made with an optical fiber could support a spatiotemporal regime. However, by using a constant injected beam, i.e., cw operation, it is hard to reach the high-intensity regime where we can observe the spatiotemporal chaos and its coexistence with a homogeneous background. To overcome this limitation, it is necessary to drive the cavity by synchronously pumping with a pulsed laser. The time-of-flight of the light pulses in the cavity should be adjusted to the laser repetition time. All experiments using this simple device with a pulse laser have shown evidence of complex spatiotemporal behaviors [2–4,39]. Therefore, the phenomenon described in this Letter should be observed experimentally.

In conclusion, by using rigorous tools of dynamical system theory, such as Lyapunov spectra, we have quantitatively shown that the complex behavior observed experimentally in the Kerr optical frequency combs [1] and in the fiber cavity [2–4] is of a spatiotemporal chaos nature. We have also shown that the Yorke–Kaplan dimension can be considered as a good order parameter to characterize the bifurcation diagram associated with spatiotemporal chaos. Finally, we have identified different operating regimes, in particular the coexistence between spatiotemporal chaos, the self-pulsating localized structure, and the homogeneous steady state. The observed complex states are exponentially sensitive to the initial conditions, exhibit complex spatiotemporal chaos, and have exponential power spectrum. Hence, this behavior is not of a turbulent nature. Therefore, our finding is important for the analysis, or classification of the various complex spatiotemporal behaviors observed in practical dissipative systems.

Funding. FONDECYT (1150507); Belgian Science Policy Office Interuniversity Attraction Poles (IAP P7-35 «photonics@be»); ANR Blanc OptiRoc (N12-BS04-0011); Laboratoire d'Excellence: Centre Européen pour les Mathématiques, la Physique et leurs Interactions; Fonds National de la Recherche Scientifique.

Acknowledgment. M. G. Clerc is grateful to the financial support of FONDECYT projects 1150507. Z. Liu, S. Coulibaly, and M. Taki are grateful to the Interuniversity Attraction Poles program of the Belgian Science Policy Office under the grant IAP P7-35 «photonics@be», the French Project ANR Blanc OptiRoc N12-BS04-0011, and the “Laboratoire d'Excellence: Centre Européen pour les Mathématiques, la Physique et leurs Interactions” CEMPI. M. Tlidi received support from the Fonds National de la Recherche Scientifique (Belgium).

REFERENCES

1. Y. K. Chembo, D. V. Strekalov, and N. Yu, Phys. Rev. Lett. **104**, 103902 (2010).
2. F. Mitschke, G. Steinmeyer, and A. Schwache, Physica D **96**, 251 (1996).
3. G. Steinmeyer, A. Schwache, and F. Mitschke, Phys. Rev. E **53**, 5399 (1996).
4. M. Anderson, F. Leo, S. Coen, M. Erkintalo, and S. G. Murdoch, Optica **3**, 1071 (2016).
5. P. Manneville, *Dissipative Structures and Weak Turbulence* (Academic, 1990).
6. D. Ruelle, Commun. Math. Phys. **87**, 287 (1982).
7. A. Pikovsky and A. Politi, *Lyapunov Exponents: A Tool to Explore Complex Dynamics* (Cambridge University, 2016).
8. G. Nicolis, *Introduction to Nonlinear Science* (Cambridge University, 1995).
9. M. G. Clerc and N. Verschuere, Phys. Rev. E **88**, 052916 (2013).
10. F. Selmi, S. Coulibaly, Z. Loghmari, I. Sagnes, G. Beaudoin, M. G. Clerc, and S. Barbay, Phys. Rev. Lett. **116**, 013901 (2016).
11. S. Coulibaly, M. G. Clerc, F. Selmi, and S. Barbay, Phys. Rev. A **95**, 023816 (2017).
12. U. Frisch, *Turbulence: The Legacy of AN Kolmogorov* (Cambridge University, 1995).
13. L. A. Lugiato and R. Lefever, Phys. Rev. Lett. **58**, 2209 (1987).
14. M. Haelterman, S. Trillo, and S. Wabnitz, Opt. Commun. **91**, 401 (1992).
15. M. Haelterman, S. Trillo, and S. Wabnitz, Opt. Lett. **17**, 745 (1992).
16. Y. K. Chembo and C. R. Menyuk, Phys. Rev. A **87**, 053852 (2013).
17. T. Hansson, D. Modotto, and S. Wabnitz, Phys. Rev. A **88**, 023819 (2013).
18. A. Coillet, J. Dudley, G. Genty, L. Larger, and Y. K. Chembo, Phys. Rev. A **89**, 013835 (2014).
19. P. Kockaert, P. Tassin, G. Van der Sande, I. Veretennicoff, and M. Tlidi, Phys. Rev. A **74**, 033822 (2006).
20. G. J. Morales and Y. C. Lee, Phys. Rev. Lett. **33**, 1016 (1974).
21. K. Nozaki and N. Bekki, Phys. Lett. A **102**, 383 (1984).
22. D. J. Kaup and A. C. Newell, Phys. Rev. **18**, 5162 (1978).
23. A. J. Scroggie, W. J. Firth, G. S. McDonald, M. Tlidi, R. Lefever, and L. A. Lugiato, Chaos Solitons Fractals **4**, 1323 (1994).
24. D. Turaev, A. G. Vladimirov, and S. Zelik, Phys. Rev. Lett. **108**, 263906 (2012).
25. K. Nozaki and N. Bekki, J. Phys. Soc. Jpn. **54**, 2363 (1985).
26. K. Nozaki and N. Bekki, Physica D **21**, 381 (1986).
27. M. Taki, K. H. Spatschek, J. C. Fernandez, and R. Grauer, Physica D **40**, 65 (1989).
28. S. Wabnitz, Opt. Lett. **18**, 601 (1993).
29. F. Christianen and H. H. Rough, Nonlinearity **10**, 1063 (1997).
30. T. J. Bridges and S. Reich, Physica D **156**, 219 (2001).
31. E. Ott, *Chaos in Dynamical Systems*, 2nd ed. (Cambridge University, 2002).
32. F. Leo, L. Gelens, P. Emplit, M. Haelterman, and S. Coen, Opt. Express **21**, 9180 (2013).
33. Y. Pomeau, Physica D **23**, 3 (1986).
34. M. G. Clerc, C. Falcon, and E. Tirapegui, Phys. Rev. Lett. **94**, 148302 (2005).
35. M. G. Clerc, C. Falcon, and E. Tirapegui, Phys. Rev. E **74**, 011303 (2006).
36. S. Coen, M. Tlidi, Ph. Emplit, and M. Haelterman, Phys. Rev. Lett. **83**, 2328 (1999).
37. S. Coulibaly, M. Taki, and M. Tlidi, Opt. Express **22**, 483 (2014).
38. M. G. Clerc, S. Coulibaly, M. Ferré, M. A. García-Nustes, and R. G. Rojas, Phys. Rev. E **93**, 052204 (2016).
39. F. Mitschke and A. Schwache, J. Opt. B **10**, 779 (1998).

Optics Letters

Nondestructive distributed measurement of supercontinuum generation along highly nonlinear optical fibers

RÉGIS HONTINFINDE,^{1,*} SALIYA COULIBALY,² PATRICE MEGRET,¹ MAJID TAKI,² AND MARC WUILPART¹

¹University of Mons, Mons, Department of Electromagnetism and Telecommunications, Boulevard Dolez 31, Mons 7000, Belgium

²Université de Lille, CNRS, UMR 8523—PhLAM—Physique des Lasers Atomes et Molécules, F-59000 Lille, France

*Corresponding author: regis.hontinfinde@umons.ac.be

Received 6 March 2017; revised 24 March 2017; accepted 26 March 2017; posted 29 March 2017 (Doc. ID 290183); published 21 April 2017

Supercontinuum generation (SCG) in optical fibers arises from the spectral broadening of an intense light, which results from the interplay of both linear and nonlinear optical effects. In this Letter, a nondestructive optical time domain reflectometry method is proposed for the first time, to the best of our knowledge, to measure the spatial (longitudinal) evolution of the SC induced along an optical fiber. The method was experimentally tested on highly nonlinear fibers. The experimental results are in a good agreement with the optical spectra measured at the fiber outputs. © 2017 Optical Society of America

OCIS codes: (120.0120) Instrumentation, measurement, and metrology; (190.0190) Nonlinear optics; (060.0060) Fiber optics and optical communications.

<https://doi.org/10.1364/OL.42.001716>

Supercontinuum generation (SCG) consists of the development of a broad continuous spectrum when high-power optical pulses propagate through a nonlinear medium such as an optical fiber [1]. This phenomenon is well known to the scientific community by its universal aspect and led to many practical achievements. The most important application of SCG to the field of telecommunications is the design of multi-wavelength sources for ultra-broadband wavelength-division-multiplexed systems based on spectral slicing of SC generated by a single laser [2–4]. SCs are also exploited in spectroscopy [5,6], pulse compression [7,8], tomography [9–11], metrology [12,13], and in the generation of optical clocks using frequency combs [14]. During the past decade, SCG in optical fibers has been extensively studied, and many contributions have been published [15–19]. It was notably established that when a fiber is pumped in the anomalous dispersion region and operating in the nanosecond pulse regime, the modulation instability (MI) plays a key role in the spectral broadening [20]. This Letter does not intend to provide an analysis of the SCG mechanisms, as it has already been largely covered by the literature [15–19], but instead aims to fill a gap in the metrology of the SC. Indeed, the SC spectrum can easily be measured at the fiber

output, but no adequate method has been proposed to measure the spatial evolution of the spectral broadening along the fiber. Note that spatial evolution means here the evolution in the longitudinal direction of propagation. So far, the only way to obtain a spatially resolved measurement of the SCG is to use the cutback method, which leads to the destruction of the fiber and, for this reason, cannot be implemented *in situ*, i.e., in a fiber communication network. This cutback method consists of measuring the spectrum spatial evolution with an optical spectrum analyzer (OSA) at discrete points by successively cutting the fiber end by a length given by the desired spatial resolution. In this Letter, an experimental method based on an optical time domain reflectometer (OTDR) is proposed for the nondestructive measurement of the SC spatial evolution along an optical fiber in the nanosecond pulse regime. The interest of our new method is twofold. On a fundamental level, it will provide a nondestructive method to compare the predictions obtained by numerical simulations with experimental results. On a more applied level, this method will enable the design optimization of broadband sources based on SCG. In the field of telecommunications, it could enable the localization of fiber trunks presenting a nonlinear coefficient that is too high (and, thus, a non-negligible crosstalk) along an optical fiber communication link. A first attempt to use a reflectometry technique for the distributed measurement of MI was described in Ref. [21]. However, a spatial resolution of only 27.5 m was reached, and only a first-order MI was characterized. The method proposed in this Letter allows obtaining a worst spatial resolution of 6.6 m. Moreover, second-order MI and SCG can be detected. To the best of our knowledge, this is the first time that the spatial evolution of the SC spectral broadening process along an optical fiber is measured. Until now, the SC spatial evolution could be only estimated by means of numerical simulations or measured by the cutback method [18].

An OTDR [22] is a widely used instrument in the field of telecommunications to characterize a fiber network and to localize defects. It makes it possible to obtain information along a fiber link without causing its destruction. The best spatial resolution of commercially available OTDRs is typically 30 cm. As the internal source of a commercially available

lower than the detection threshold of the OTDR. As soon as the level of the backscattered powers related to the MI Stokes and anti-Stokes wavelengths rises above the OTDR threshold detection, the spatial evolution of the two MI components can be measured. One can notice that for fiber 1, the MI intensity grows until the fiber end while for fiber 2, it grows first and then saturates.

From systematic measurement of the backscattered power spatial distribution performed by tuning the tunable filter 2, a map of the spectrum of the light generated along the optical fiber can be obtained. The mapping of the nonlinear spectral broadening in the tested fibers is shown in Figs. 3(a) and 3(b). From the mapping, one can precisely localize where the different components are generated along the fibers. In particular, the spatial evolution of the fundamental and secondary MI components can be observed.

The goal of the next experimental investigation is to apply the OTDR method to measure the spatial evolution of the full SC, whose development requires the modulation instability, as well as other nonlinear phenomena such as self-phase modulation and stimulated Raman scattering [24]. For that purpose, fibers 1 and 2 were characterized by the same experimental setup with an increased value on the input peak power. P_0 was fixed to 7 W (7.3 W) for fiber 1 (2). The measured spatial evolution of the SC spectrum along fiber 1 (2) is shown in Figs. 3(c) and 3(d). Note that this is the first time, to the best of our knowledge, that a mapping showing the spatial evolution of an SC along an optical fiber is measured. The initial stage of the wave propagation is dominated by an approximately symmetrical spectral broadening detected from 80 m (240 m) distance for fiber 1 (2). This result agrees with the nonlinear wave propagation theory in the nanosecond pulse regime, which predicts that the SC is initiated from the modulation instability [15]. After approximately 175 m (360 m) of propagation, the spectral broadening becomes highly asymmetric due to the significant impact of the third-order dispersion and Raman scattering. After 175 m (360 m) and until the fiber end, the spectrum continues to broaden as a result of cascaded MI processes and Raman scattering (at longer wavelengths) [24]. The peak around 1600 nm in fiber 1 is due to the generated redshifted solitons. For fiber 2, the peak around

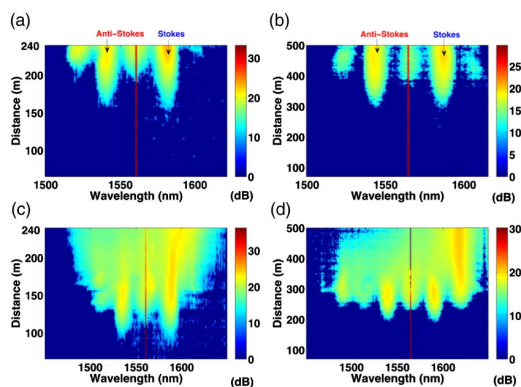


Fig. 3. Mapping of the nonlinear spectral broadening in the fibers under test. (a) and (b) correspond to the mapping of the nonlinear broadening due to the MI evolution in fibers (1) and (2), respectively. (c) and (d) show the mapping of the nonlinear broadening due to the SC generation in fibers (1) and (2), respectively.

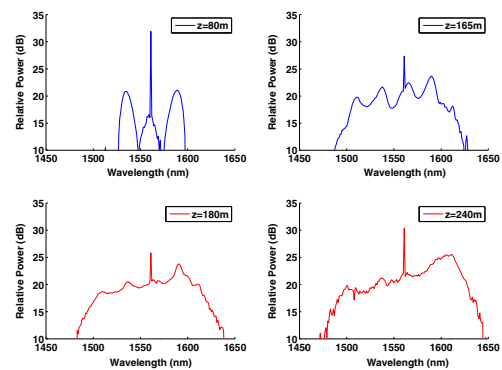


Fig. 4. Selection SC spectra measured at different propagation distances along fiber 1 (80, 165, 180, and 240 m).

1616 nm corresponds to the second-order modulation instability arising from the fourth-order dispersion (β_4) and the presence of the second ZDW. The peak grows over time and shows a slight blueshift, indicating that there is both Raman scattering and a phase-matched transfer of energy across the ZDW in the form of dispersive waves.

The spectral broadening measured at different locations along fiber 1 with the proposed method is displayed in Fig. 4. The light spectrum at 80 m is typical of a location where the two symmetrical MIs are observed. Along a propagation distance of 165 m, the generation of second-harmonic MI components is detected. A slight asymmetry can also be observed in the amplitude of the two fundamental MI components due to the third-order dispersion effect. At 180 m, this asymmetry is more pronounced due to the strong impact of Raman scattering. At 240 m (fiber end), Raman scattering is responsible for the large broadening. The characteristics of the spectrum measured at the fiber end are qualitatively similar to those published for the long regime [15].

In order to validate the nondestructive OTDR method, the output spectra obtained at the end of the fibers were compared with those measured by an OSA. The comparison is presented in Fig. 5, where the optical spectra measured at the end of the fibers with the proposed method are displayed in red, while the spectra obtained with an OSA are displayed in black. Figures 5(a) and 5(b) show the MI spectra measured at the output of fiber 1 (2) with a pump peak power of 2 W (2.3 W). Figures 5(c) and 5(d) show the SC spectra measured at the output of fiber 1 (2) with a pump peak power of 7 W (7.3 W). A good agreement is obtained between the two measurements. Note that the MI frequency shift Ω is not the same for the two fibers. This results from different nonlinear coefficients and dispersion profiles [24]. Let us specify that we measure the mean SC, since an averaging is performed over 30 s when measuring an OTDR trace in order to increase the SNR.

In order to evaluate the effective spatial resolution, the pulse duration at the end of the fiber under test was determined over the whole analyzed spectral range. The maximum pulse duration obtained over the spectral range (1450–1650 nm) was 66 (64) ns for fiber 1 (2). Therefore, worse spatial resolution due to the finite pulse duration is 6.6 m. Note that since OTDRs operate by measuring the backscattered signal intensity as a function of the propagation round-trip time, the calculated

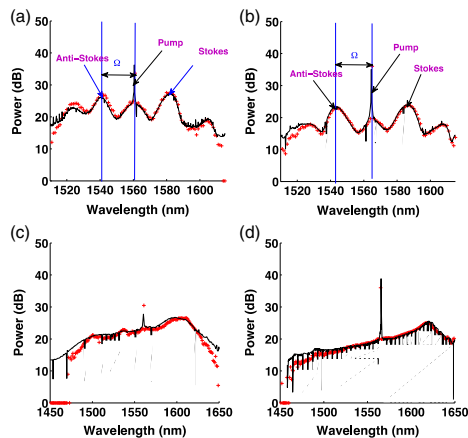


Fig. 5. Comparison of the optical spectra measured at the fiber output with the proposed method (red) and with an OSA (black) at the end of the fiber. (a) MI spectra measured at the output of fiber 1 with a pump peak power of 2 W. (b) MI spectra measured at the output of fiber 2 with a pump peak power of 2.3 W. (c) SC spectra measured at the output of fiber 1 with a pump peak power of 7 W. (d) SC spectra measured at the output of fiber 2 with a pump peak power of 7.3 W.

distance can be affected by the dispersion of the fiber under test. We evaluated the corresponding error by taking into account the two extreme wavelengths of our spectral analysis (1450–1650 nm), neglecting the nonlinear group velocity corrections and assuming a constant dispersion equal to the largest dispersion of the fiber over this range (D_{\max}) and considering a backscattering position located close to the fiber end. This analysis provides an upper bound limit on the distance detuning induced by the dispersion. Taking into account that $|D_{\max}|$ is equal to $2(0.344) \text{ ps} \cdot \text{km}^{-1} \cdot \text{nm}^{-1}$ for fiber 1 (2), the maximum localization detuning is given by 9.81 (3.5) mm. Finally, the spatial resolution of the measurement system can be improved by updating some of the components used in the setup. If a centimeter resolution is required, the modulator can be upgraded in order to generate 100 ps pulses. Working with pulses of 100 ps implies that the backscattered signal will not be strong enough to be detected by a conventional OTDR. A photon-counting OTDR can be used to increase the detection SNR. Such an upgrade would allow characterizing the SC process in a photonic crystal fiber (PCF).

In conclusion, a nondestructive method for the measurement of the SC spatial evolution (in the nanosecond regime) along optical fibers was proposed. The method was successfully tested in two highly nonlinear fibers under two different input peak power conditions leading to MI generation only and to SCG. The spectra measured at the fiber output are in very good agreement with those measured by an OSA, which validates the proposed method at the only accessible point for standard OSA measurement. Moreover, the method can be performed without damaging the fiber and perturbing the intrinsic dynamics of nonlinear processes. It is worth emphasizing that, to the best of our knowledge, mappings of the SC spectral evolutions could, until now, only be estimated by means of simulations

or by using the cutback method. In a more general perspective, this method is not limited to fiber systems, but can be applied for a more general class of nonlinear systems where internal measurement is desired, as long as some reflective points are present along the optical path.

Funding. Interuniversity Attraction Poles program of Federaal Wetenschapsbeleid (BELSPO) (IAP 7-35).

Acknowledgment. The authors thank A. Mussot and G. Bouwmans for providing the highly nonlinear optical fibers, as well as G. Ravet and O. Deparis for interesting discussions.

REFERENCES

1. R. R. Alfano and S. L. Shapiro, *Phys. Rev. Lett.* **24**, 584 (1970).
2. T. Morioka, H. Takara, S. Kawanishi, O. Kamatani, K. Takiguchi, K. Uchiyana, S. Saruwatari, H. Takahashi, M. Yamada, T. Kanamori, and H. Ono, *Electron. Lett.* **32**, 906 (1996).
3. K. Tamura, E. Yoshida, and M. Nakazawa, *Electron. Lett.* **32**, 1691 (1996).
4. H. Sotobayashi, W. Chujo, A. Konishi, and T. Ozeki, *J. Opt. Soc. Am. B* **19**, 2803 (2002).
5. A. B. Fedotov, A. M. Zheltikov, A. A. Ivanov, M. V. Alfimov, D. Chorvat, V. I. Beloglazov, L. A. Melnikov, N. B. Skibina, A. P. Tarasevitch, and D. von der Linde, *Laser Phys.* **10**, 723 (2000).
6. S. T. Sanders, *Appl. Phys. B* **75**, 799 (2002).
7. W. J. Tomlinson, R. J. Stolen, and C. V. Shank, *J. Opt. Soc. Am. B* **1**, 139 (1984).
8. C. V. Shank, R. L. Fork, R. Yen, and R. H. Stolen, *Appl. Phys. Lett.* **40**, 761 (1982).
9. I. Hartl, X. D. Li, C. Chudoba, R. K. Ghanta, T. H. Ko, J. G. Fujimoto, J. K. Ranka, and R. S. Windeler, *Opt. Lett.* **26**, 608 (2001).
10. Y. M. Wang, Y. H. Zhao, J. S. Nelson, Z. P. Chen, and R. S. Windeler, *Opt. Lett.* **28**, 182 (2003).
11. D. L. Marks, A. L. Oldenburg, J. J. Reynolds, and S. A. Boppart, *Opt. Lett.* **27**, 2010 (2002).
12. K. Mori, T. Morioka, and M. Saruwatari, *IEEE Trans. Instrum. Meas.* **44**, 712 (1995).
13. J. Jasapara, T. H. Her, R. Bise, R. Windeler, and D. J. DiGiovanni, *J. Opt. Soc. Am. B* **20**, 1611 (2003).
14. A. S. Mayer, A. Klenner, A. R. Johnson, K. Like, M. R. E. Lamont, Y. Okawachi, M. Lipson, A. L. Gaeta, and U. Keller, *Opt. Express* **23**, 15451 (2005).
15. J. M. Dudley, G. Genty, and S. Coen, *Rev. Mod. Phys.* **78**, 1135 (2006).
16. M. Klimczak, G. Sobon, R. Kaszatelanic, K. M. Abramski, and R. Buczynski, *Sci. Rep.* **6**, 19284 (2016).
17. B. Wetzel, A. Stefani, L. Larger, P. A. Lacourt, J. M. Merolla, T. Sylvestre, A. Kudlinski, A. Mussot, G. Genty, F. Dias, and J. M. Dudley, *Sci. Rep.* **2**, 882 (2012).
18. A. Kudlinski, G. Bouwmans, M. Douay, M. Taki, and A. Mussot, *J. Lightwave Technol.* **27**, 1556 (2009).
19. A. Demircan and U. Bandelow, *Appl. Phys. B* **86**, 31 (2007).
20. J. M. Dudley, G. Genty, F. Dias, B. Kibler, and N. Akhmediev, *Opt. Express* **17**, 21497 (2009).
21. G. Ravet, A. Mussot, M. Wuilpart, A. Kudlinski, C. Caucheteur, and P. Mège, *IEEE Photonics Society Summer Topicals*, 2010, paper WC1.3.
22. D. Anderson and F. Bell, *Optical Time-Domain Reflectometry* (Tektronix, 1997).
23. T. Okuno, M. Hirano, T. Nakanishi, and M. Onishi, *SEI Tech. Rev.* **62**, 34 (2006).
24. G. P. Agrawal, *Nonlinear Fiber Optics*, 5th ed. (Academic, 2013).

Spatiotemporal Chaos Induces Extreme Events in an Extended Microcavity Laser

F. Selmi,¹ S. Coulibaly,² Z. Loghmari,¹ I. Sagnes,¹ G. Beaudoin,¹ M. G. Clerc,³ and S. Barbay^{1,*}

¹Laboratoire de Photonique et de Nanostructures, CNRS, Université Paris Saclay, Route de Nozay, 91460 Marcoussis, France

²Université de Lille, CNRS, UMR 8523 - PhLAM - Physique des Lasers Atomes et Molécules, F-59000 Lille, France

³Departamento de Física, Facultad de ciencias Físicas y Matemáticas, Universidad de Chile, Casilla 487-3, Santiago, Chile

(Received 30 July 2015; published 8 January 2016)

Extreme events such as rogue waves in optics and fluids are often associated with the merging dynamics of coherent structures. We present experimental and numerical results on the physics of extreme event appearance in a spatially extended semiconductor microcavity laser with an intracavity saturable absorber. This system can display deterministic irregular dynamics only, thanks to spatial coupling through diffraction of light. We have identified parameter regions where extreme events are encountered and established the origin of this dynamics in the emergence of deterministic spatiotemporal chaos, through the correspondence between the proportion of extreme events and the dimension of the strange attractor.

DOI: 10.1103/PhysRevLett.116.013901

A record spawned by a natural system may consist of periods where a relevant variable undergoes small variations around a well-defined level provided by its long-time average, with the occasional occurrence of abrupt excursions to values that differ significantly from the average level, called extreme events [1]. Extreme and rare events are ubiquitous in nature. In optics, an extreme event is characterized by a rare, intense optical pulse in a given intensity probability density distribution. The study of extreme events and extreme waves [2] has been motivated by the analogy with rogue waves in hydrodynamics [3] that are giant waves recently observed in the ocean and whose formation mechanism is still not well understood. Physically, it is based on the fact that some conservative systems in optics and deep water waves in the ocean can be described by the nonlinear Schrödinger equation [4]. Most of the studies in this context have taken place in optical fibers where the interplay of nonlinearity, dispersion and noise generates extreme events [5–8]. Extreme events such as rogue waves in optics and fluids are often associated with the merging dynamics of coherent structures [9–11], with a stochastically induced transition in multistable systems [12] or with chaotic dynamics in low dimensional systems [13]. Extreme events have been observed in optical cavity systems, such as an injected nonlinear optical cavity [14], fiber lasers [9,15], solid-state lasers [16] and semiconductor lasers [13,17]. The role of spatial coupling has not been studied until recently in a pattern-forming optical system composed of a photorefractive crystal subjected to optical feedback [18,19] or a low Fresnel number solid-state laser [20], while most of the characterizations of extreme events were done from a statistical point of view, without establishing their origin from the dynamical system point of view.

In this Letter, we report on experimental and numerical results on the physics of extreme event appearance in a

spatially extended nonlinear dissipative system and establish the origin of this dynamics in the emergence of spatiotemporal chaos. Our system is a planar microcavity laser with an integrated saturable absorber [21,22] pumped along a rectangular aperture, implementing a quasi-1D spatially extended nonlinear dissipative system (cf. Fig. 1). Besides the very different dynamical regimes that can be observed in it (e.g., laser cavity solitons [22,23] or excitable regimes [24,25]), a particularity of this system is that in the absence of spatial coupling it does not display irregular or aperiodic dynamics or extreme events [26]. However, spatial coupling through diffraction and nonlinear effects can make the dynamics become more irregular, especially if the system has a large aspect ratio (or Fresnel number) as

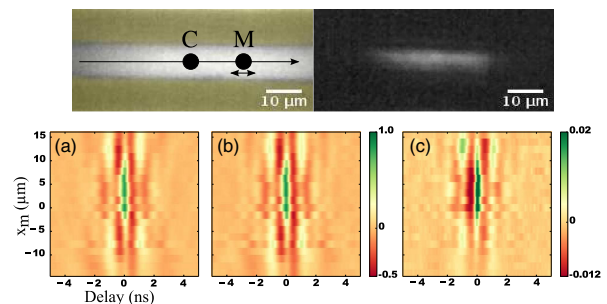


FIG. 1. Top panels: Images of the surface of the extended microcavity laser with an integrated saturable absorber below (left) and above (right) the laser threshold. The dark (yellow) zone is the gold mask delimiting the pumping region. Bottom panels: (a) Temporal cross-correlation $X_{C,M}(t_k, x_m)$ (see text) between the detector responses in points C ($x_m = 0$) and M at delays $t_k = k\Delta t$. (b) Same as (a) restricted to extreme events at point C. (c) Average of the responses at point M and at times where an abnormal event has occurred in the center of the laser in C.

is the case here. Above the laser threshold, self-pulsing takes place, and we study experimentally the impact of the pumping intensity on the intensity statistics and on the occurrence of extreme events. By recording the dynamics simultaneously in two different spatial points, we are able to study whether the extreme events occur through a mechanism of coherent structure collision. Indeed, stationary and propagative laser coherent structures were predicted [27–32] in this system, and stationary structures were observed [22,23] in some parameter regions. With the help of a mathematical model, linear stability and numerical analysis of the dynamics, we unveil the dynamical origin of the extreme events found.

The microcavity structure used in this experiment is described in Refs. [22,23]. A gold mask is deposited onto the sample surface to define the pump geometry. We concentrate on an elongated pump profile with a gold opening having $80\ \mu\text{m}$ length and $10\ \mu\text{m}$ width. The linear microcavity is pumped above threshold, and the intensity in a point close to its center is recorded with a fast avalanche photodiode (5-GHz bandwidth). The temporal signal is amplified thanks to a low noise, high bandwidth amplifier and acquired with a 6-GHz oscilloscope at 20 GS/s ($\Delta t = 50\ \text{ps}$). Up to 50×10^6 points can be acquired in a single trace. Figure 1 shows the near field of the laser below and above threshold, respectively.

Time traces once acquired are treated to display the histogram of the intensity heights. Figure 2 displays histograms versus the pump parameter. At normalized pump power $P/P_{\text{th}} = 1.02$, where P_{th} is the pump at laser threshold, they are characterized by a quadratic decay in the tails, and the probability density function (PDF) looks like a Rayleigh distribution for a positive-valued Gaussian process. As the pump is increased, the statistics develops long tails with an initial exponential decay ($P/P_{\text{th}} = 1.17$). For still higher pump values, the PDF becomes exponential ($P/P_{\text{th}} = 1.20$) and then redisplay Gaussian tails ($P/P_{\text{th}} = 1.25$). The global evolution of the mean amplitude versus pump intensity is reminiscent of the dynamics expected for a zero-dimensional laser with a saturable absorber [33]: Close to threshold, a quite regular amplitude pulse train sets in [see Fig. 2(c)]. For higher pump intensities, the mean pulse period increases and, because of the spatial coupling, the amplitude becomes very irregular and displays a complex dynamics [Figs. 2(d), 2(g), and 2(h)]. We have computed the threshold amplitude for extreme events, adopting the traditional hydrodynamical criterion. We consider as extreme events those events having a height H twice the significant height H_s (mean of the highest tertile of the PDF), i.e., with an abnormality index $AI \equiv H/H_s > 2$ [2]. The height H is extracted as the maximum of the left and right intensity heights $H = \max(H_l, H_r)$. Note that the results do not change significantly by considering either H , H_l , or H_r . To get rid of the large number of small peaks of noise at the

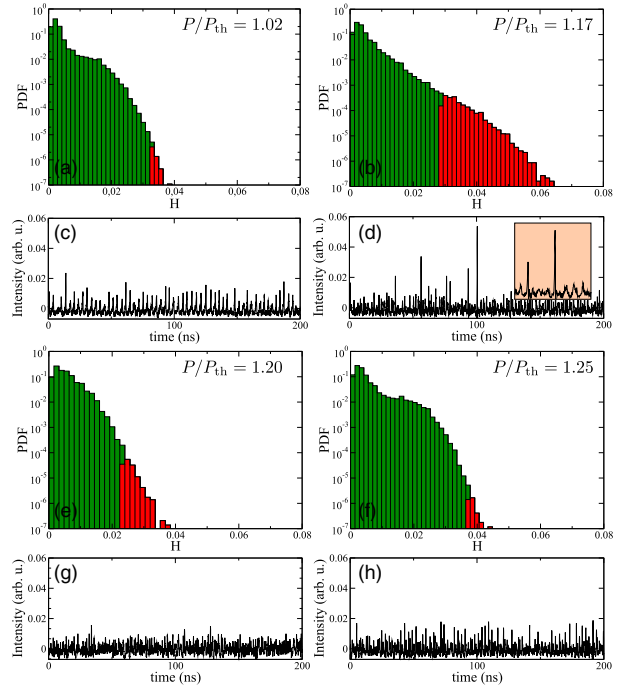


FIG. 2. (a,b,e,f) Logarithm of the PDF of the intensity height H at position C for different normalized pump values. Extreme events ($AI > 2$) are shown in red. (c,d,g,h) Excerpts of the time evolution for the corresponding pumps. (d) A 20-ns zoom on the central extreme event.

left of the PDF, we compute the significant height H_s only by considering events whose height is larger than the observed maximum peak dark noise amplitude, which is about 5 mV (note that the rms noise is only 0.9 mV). This threshold introduces a more stringent criterion for extreme event detection. Extreme events are depicted in red under the histograms presented in Fig. 2. We observe that the maximum number of extreme events is obtained in the PDF with a non-Gaussian tail, i.e., with a normalized pump of 1.17.

The statistics of times between two spikes with $AI > 2$ displays a Kramers statistics with exponential behavior such that spike appearance obeys a Poisson, memoryless process. We now study the spatiotemporal structure of the statistics of emitted pulses. We record the dynamics in two points: one at a fixed position at the center of the laser (represented by point C) and the other moving along the long line laser (point M). This is made by enlarging the laser surface image by optical magnification and placing the detectors in that plane. On the bottom panels in Fig. 1, we plot the normalized cross-correlation $X_{c,m}(k)$ of the $N = 10^5$ first recorded points ($5\ \mu\text{s}$) between the signal recorded at the central detector y_c at point C and the one at the moving detector y_m at location M, $1 \leq m \leq 20$ such that

$$X_{c,m}(k) = \frac{1}{N\sigma_{y_c}\sigma_{y_m}} \sum_i [y_c(i) - \bar{y}_c][y_m(i+k) - \bar{y}_m]$$

where the bar symbol and σ indicate the mean value and the standard deviation. In the central part there is a zone with high positive (green) cross-correlation followed and preceded by two bands of negative cross-correlation. The temporal band in which the cross-correlation is nonzero extends about 2 ns from around zero delay. Therefore, we can infer the existence of a finite correlation length in the system, which is smaller than the lasing system size (about 30 μm). However, since the correlation bands are vertical at these time scales, we do not have clear evidence of propagation effects (at least with the temporal resolution of our setup), though there is a slight bending of the correlated band (in green). In Fig. 1(b) we restrict the cross-correlation around the points where $AI > 2$; i.e., we consider only extreme events. Notice that there are no major differences between the two cross-correlations; hence, there does not seem to be any statistical marker of the appearance of an extreme event in this regime and, in particular, no clear sign of propagation of a coherent structure either. These results indicate that extreme height intensity peaks appear in a spatial correlation zone and disappear almost immediately everywhere in this zone. Correlation is therefore maximum at zero delay for almost all positions detected. Figure 1(c) depicts the average of the responses at position M and at times where an abnormal event has occurred in the center of the laser in C . The average shows a clear time asymmetry around the correlated structure; every selected event begins with a large amplitude dip followed by a large positive peak. On the wings of the correlated zone, we can see another dip. In this system extreme events thus appear and disappear almost simultaneously everywhere in a correlation window. There is no evidence, at least up to our temporal resolution, of a clear collision of coherent structures leading to the observed behavior. Instead, we consider the complexity in the spatiotemporal dynamics itself as the dynamical origin of extreme events.

To this aim, we compare our findings with numerical simulations of an envelope equation of a one-dimensional spatially extended laser with a saturable absorber [34]. The model consists of three coupled nonlinear partial differential equations,

$$\begin{aligned} \frac{\partial E}{\partial t} &= [(1 - i\alpha)G + (1 - i\beta)Q - 1]E + i\frac{\partial^2 E}{\partial x^2}, \\ \frac{\partial G}{\partial t} &= \gamma_g[\mu - G(1 + |E|^2)], \\ \frac{\partial Q}{\partial t} &= \gamma_q[-\gamma - Q(1 + s|E|^2)], \end{aligned} \quad (1)$$

for the intracavity electric-field envelope $E(x, t)$ and the carrier density in the gain (resp. saturable absorber) section

$G(x, t)$ [resp. $Q(x, t)$]. The nonradiative carrier recombination rates are γ_g and γ_q with pumping μ and linear absorption γ . The Henry enhancement factors in both sections are α and β , respectively. Diffraction is included through the complex Laplacian term. Time has been rescaled to the field lifetime in the cavity, which is calculated as 8.0 ps, given the cavity design parameters. Space is rescaled to the diffraction length w_d , which is 7.4 μm . We take parameters compatible with our semiconductor system: $\alpha = 2$, $\beta = 0$, $s = 10$, $\gamma_g = \gamma_q = 0.005$ and $\gamma = 0.5$. The equations are simulated using the Xmds2 package [35] with a split operator method and an adaptive, fourth-order Runge-Kutta method for time integration. The width of the integration region w is $w/w_d = 24$ with a top-hat pumping of width $w_p/w_d = 12$. Based on the results developed in Ref. [34], we can describe the main properties of the plane-wave stationary solutions and of the linear stability analysis. The results are shown in Fig. 4 for the latter set of parameters. The plane-wave characteristic curve of the laser has a C shape with a subcritical bifurcation at threshold for $\mu_{\text{th}} = 1 + \gamma$, provided $s > 1 + 1/\gamma$. In a certain range of parameters, the system also exhibits an Andronov-Hopf bifurcation giving rise to self-pulsation (for $\mu < \mu_H \sim 3.08$). When including the spatial degree of freedom, a linear stability analysis reveals that the upper branch is usually Turing unstable everywhere (gray region), giving rise to a complex spatiotemporal dynamics. An Andronov-Hopf instability can also occur for small harmonic perturbations in space with a band of unstable wave vectors k (blue region disconnected from the vertical axis).

The logarithm of the PDF for the theoretical height distribution for Eq. (1) is shown in Fig. 3. For low pumping it displays a subexponential tail with a small number of extreme events. Then the tail of the PDF progressively becomes more and more exponential at the start of the distribution, with a large deviation for large events giving rise to a maximum number of extreme events for $\mu = 2.9$. The tail of the distribution then becomes quasiexponential at $\mu = 3.1$ and then subexponential again at $\mu = 3.4$, with a decrease in the number of extreme events. These observations reproduce qualitatively well what is found in the experiment. Moreover, the shape of the distribution seems to be strongly correlated to the presence or not of an Andronov-Hopf bifurcation: Only when it is present can we observe a heavy-tailed distribution. At the transition between the Hopf-Turing and Turing-only regions, we observe the maximum number of extreme events (for $\mu = 2.9$).

A characterization of chaos and spatiotemporal chaos can be achieved by means of Lyapunov exponents [36]. These exponents measure the growth rate of generic small perturbations around a given trajectory in a finite dimensional dynamical systems. There are as many exponents as the dimension of the system under study. Additional

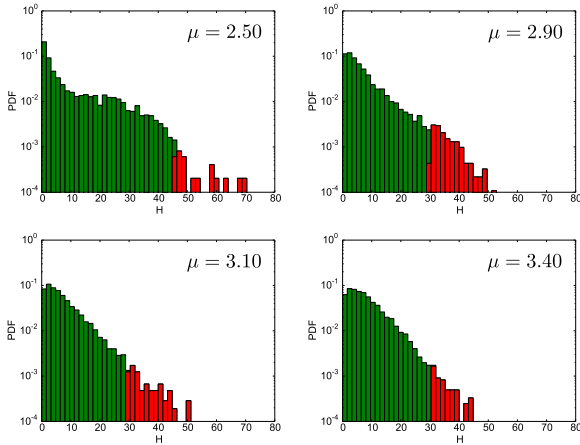


FIG. 3. Logarithm of the PDF of the theoretical height distribution for the 1D laser with a saturable absorber, Eq. (1), versus pump parameter μ . Extreme events ($AI > 2$) are shown in red.

information about the complexity of the system can be obtained from the exponents, for instance, the dimension of the strange attractor (spectral dimensionality) or measures of the dynamic disorder (entropy) [37] or characterization of the bifurcations diagram [38]. The analytical study of Lyapunov exponents is a thorny endeavor and, in practice, inaccessible. Hence, a reasonable strategy is to derive the exponents numerically by discretizing the set of partial differential equations (1). Let N be the number of discretization points; then the system has N Lyapunov exponents λ_i . If the Lyapunov exponents are sorted in decreasing order and in the thermodynamic limit ($N \rightarrow \infty$), these exponents converge to a continuous spectrum as Ruelle conjectured [39]. Therefore, if the system has spatiotemporal chaos in this limit, there exists an infinite number of positive Lyapunov exponents. The set of Lyapunov exponents provides an upper limit for the strange attractor dimension through the Kaplan-Yorke dimension [37], $D_{KY} = p + \sum_{i=1}^p \lambda_i / \lambda_{p+1}$, where p is the largest integer that satisfies $\sum_{i=1}^p \lambda_i > 0$. In the thermodynamic limit the Yorke-Kaplan dimension diverges with the size of the system as a consequence of the Lyapunov density [40]. We have calculated the Lyapunov spectrum (cf. Fig. 4) corresponding to the total intensity integrated over x in the model (1). This figure clearly shows that when the system exhibits extreme events, it is in a regime of spatiotemporal chaos with several nonzero Lyapunov exponents in the Lyapunov spectrum and an absence of structure in the delay embedding.

Moreover, we have computed the proportion of extreme events p_{EE} , the normed kurtosis $\gamma_2 = \mathbb{E}[(X - \mu)/\sigma]^4 - 3$ and the Kaplan-Yorke dimension D_{KY} versus the pump in Fig. 5. Both p_{EE} and γ_2 display a maximum versus pump of around $\mu \approx 3$ with some correlated oscillations. D_{KY} increases steadily from zero at $\mu = 1.525$ and then saturates

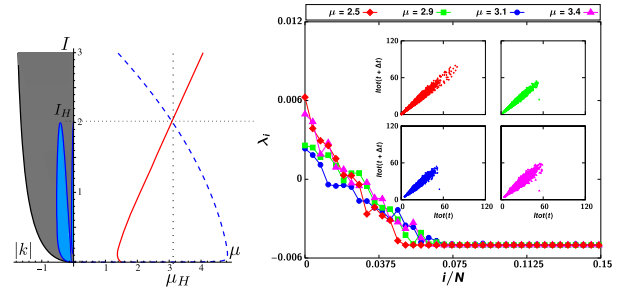


FIG. 4. Phase portrait of the LSA model. The left panel shows the characteristic curve $\mu(I)$ (red) along with the unstable wave-vector regions of the linear stability analysis (Turing instability, grey; Andronov-Hopf instability, blue). The right axis is μ and the left axis is the modulus $|k|$ of the unstable wave vectors. The plane-wave Hopf curve is shown as a dashed blue line. The right panel shows the computed Lyapunov spectrum for different pump parameters and corresponding two-dimensional delay embedding for the total intensity $I_{tot}(t)$.

after $\mu = 2$. From these findings we infer that there is a smooth or supercritical transition of the system into spatiotemporal chaos, and this behavior is concomitant with the increase of the number of extreme events. Note, however, that there is no reason why there should be a strict correlation between D_{KY} and p_{EE} since the latter is related to the structure of the attractor itself and not only to its dimension [41].

In conclusion, we have shown experimental results of extreme event appearance in a quasi-1D broad area laser with a saturable absorber. We have analyzed the physical origin of extreme events that occur because of the onset of deterministic spatiotemporal chaos in the system. Irregular dynamics is obviously a prerequisite for the observation of extreme events, but we show in our work that the proportion of extreme events is not directly linked to the evolution of the Kaplan-Yorke dimension. A higher dimensional dynamics does not necessarily lead to a higher number of extreme events. The origin of extreme events in that case is thus to be found in the nature of the spatiotemporal complexity that takes place, and thus, it could offer interesting prospects for control by changing the system geometry or the nature of the coupling.

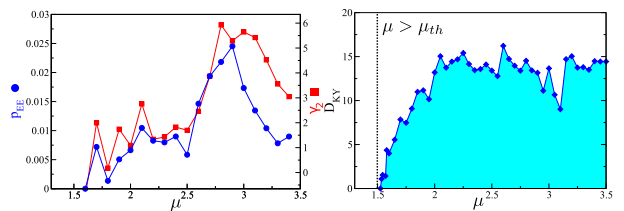


FIG. 5. Left panel: Proportion of extreme events (p_{EE} , blue circles) and normed kurtosis (γ_2 , red squares) versus pump μ . Right panel: Kaplan-Yorke dimension (D_{KY} , blue diamonds) versus pump μ .

F. S., S. C., Z. L., and S. B. acknowledge partial support from the Centre National de la Recherche Scientifique, the French network Renatech and the ANR Blanc project Optiroc. M. G. C. received financial support from FONDECYT Project No. 1150507.

*sylvain.barbay@lpn.cnrs.fr

- [1] G. Nicolis and C. Nicolis, *Foundations of Complex Systems: Emergence, Information and Prediction*, 2nd ed. (World Scientific, River Edge, NJ, 2012).
- [2] M. Onorato, S. Residori, U. Bortolozzo, A. Montina, and F. Arecchi, *Phys. Rep.* **528**, 47 (2013).
- [3] C. Kharif and E. Pelinovsky, *Eur. J. Mech. B, Fluids* **22**, 603 (2003).
- [4] D. R. Solli, C. Ropers, P. Koonath, and B. Jalali, *Nature* **450**, 1054 (2007).
- [5] J. M. Dudley, G. Genty, and B. J. Eggleton, *Opt. Express* **16**, 3644 (2008).
- [6] A. Mussot, A. Kudlinski, M. Kolobov, E. Louvergneaux, M. Douay, and M. Taki, *Opt. Express* **17**, 17010 (2009).
- [7] B. Kibler, J. Fatome, C. Finot, G. Millot, F. Dias, G. Genty, N. Akhmediev, and J. M. Dudley, *Nat. Phys.* **6**, 790 (2010).
- [8] F. T. Arecchi, U. Bortolozzo, A. Montina, and S. Residori, *Phys. Rev. Lett.* **106**, 153901 (2011).
- [9] C. Lecaplain, P. Grelu, J. M. Soto-Crespo, and N. Akhmediev, *Phys. Rev. Lett.* **108**, 233901 (2012).
- [10] A. Antikainen, M. Erkintalo, J. M. Dudley, and G. Genty, *Nonlinearity* **25**, R73 (2012).
- [11] S. Birkholz, E. T. J. Nibbering, C. Brée, S. Skupin, A. Demircan, G. Genty, and G. Steinmeyer, *Phys. Rev. Lett.* **111**, 243903 (2013).
- [12] A. N. Pisarchik, R. Jaimés-Reátegui, R. Sevilla-Escoboza, G. Huerta-Cuellar, and M. Taki, *Phys. Rev. Lett.* **107**, 274101 (2011).
- [13] C. Bonatto, M. Feyereisen, S. Barland, M. Giudici, C. Masoller, J. R. R. Leite, and J. R. Tredicce, *Phys. Rev. Lett.* **107**, 053901 (2011).
- [14] A. Montina, U. Bortolozzo, S. Residori, and F. T. Arecchi, *Phys. Rev. Lett.* **103**, 173901 (2009).
- [15] S. Randoux and P. Suret, *Opt. Lett.* **37**, 500 (2012).
- [16] M. G. Kovalsky, A. A. Hnilo, and J. R. Tredicce, *Opt. Lett.* **36**, 4449 (2011).
- [17] A. K. D. Bosco, D. Wolfersberger, and M. Sciamanna, *Opt. Lett.* **38**, 703 (2013).
- [18] V. Odont, M. Taki, and E. Louvergneaux, *Nat. Hazards Earth Syst. Sci.* **10**, 2727 (2010).
- [19] N. Marsal, V. Caultet, D. Wolfersberger, and M. Sciamanna, *Opt. Lett.* **39**, 3690 (2014).
- [20] C. Bonazzola, A. Hnilo, M. Kovalsky, and J. R. Tredicce, *J. Opt.* **15**, 064004 (2013).
- [21] S. Barbay, Y. Ménesguen, I. Sagnes, and R. Kuszelewicz, *Appl. Phys. Lett.* **86**, 151119 (2005).
- [22] T. Elsass, K. Gauthron, G. Beaudoin, I. Sagnes, R. Kuszelewicz, and S. Barbay, *Eur. Phys. J. D* **59**, 91 (2010).
- [23] T. Elsass, K. Gauthron, G. Beaudoin, I. Sagnes, R. Kuszelewicz, and S. Barbay, *Appl. Phys. B* **98**, 327 (2010).
- [24] S. Barbay, R. Kuszelewicz, and A. M. Yacomotti, *Opt. Lett.* **36**, 4476 (2011).
- [25] F. Selmi, R. Braive, G. Beaudoin, I. Sagnes, R. Kuszelewicz, and S. Barbay, *Phys. Rev. Lett.* **112**, 183902 (2014).
- [26] J. L. A. Dubbeldam and B. Krauskopf, *Opt. Commun.* **159**, 325 (1999).
- [27] I. Perrini, S. Barbay, T. Maggipinto, M. Brambilla, and R. Kuszelewicz, *Appl. Phys. B* **81**, 905 (2005).
- [28] N. Rosanov, S. Fedorov, and A. Shatsev, *Appl. Phys. B* **81**, 937 (2005).
- [29] N. N. Rosanov, S. V. Fedorov, and A. N. Shatsev, *Phys. Rev. Lett.* **95**, 053903 (2005).
- [30] F. Prati, G. Tissoni, L. A. Lugiato, K. M. Aghdami, and M. Brambilla, *Eur. Phys. J. D* **59**, 73 (2010).
- [31] G. Tissoni, K. Aghdami, M. Brambilla, and F. Prati, *Eur. Phys. J. Spec. Top.* **203**, 193 (2012).
- [32] A. G. Vladimirov, A. Pimenov, S. V. Gurevich, K. Panajotov, E. Averlant, and M. Tlidi, *Phil. Trans. R. Soc. A* **372**, 20140013 (2014).
- [33] A. Tierno, N. Radwell, and T. Ackemann, *Phys. Rev. A* **84**, 043828 (2011).
- [34] M. Bache, F. Prati, G. Tissoni, R. Kheradmand, L. Lugiato, I. Protzenko, and M. Brambilla, *Appl. Phys. B* **81**, 913 (2005).
- [35] G. R. Dennis, J. J. Hope, and M. T. Johnsson, *Comput. Phys. Commun.* **184**, 201 (2013).
- [36] P. Manneville, in *Dissipative Structures and Weak Turbulence*, edited by P. Manneville (Academic Press, Boston, 1990).
- [37] E. Ott, *Chaos in Dynamical Systems* (Cambridge University Press, Cambridge, England, 2002).
- [38] M. G. Clerc and N. Verschueren, *Phys. Rev. E* **88**, 052916 (2013).
- [39] D. Ruelle, *Commun. Math. Phys.* **87**, 287 (1982).
- [40] M. R. Paul, M. I. Einarsson, P. F. Fischer, and M. C. Cross, *Phys. Rev. E* **75**, 045203 (2007).
- [41] V. Lucarini, D. Faranda, J. Wouters, and T. Kuna, *J. Stat. Phys.* **154**, 723 (2014).

Dissipative Localized States with Shieldlike Phase Structure

Marcel G. Clerc,¹ Saliya Coulibaly,² Mónica A. Garcia-Ñustes,¹ and Yair Zúrate¹

¹*Departamento de Física, Facultad de Ciencias Físicas y Matemáticas, Universidad de Chile, Casilla 487-3, Santiago, Chile*

²*Laboratoire de Physique des Lasers, Atomes et Molécules, CNRS UMR 8523, Université des Sciences et Technologies de Lille–59655 Villeneuve d'Ascq Cedex, France, EU*

(Received 30 June 2011; published 14 December 2011)

A novel type of parametrically excited dissipative solitons is unveiled. It differs from the well-known solitons with constant phase by an intrinsically dynamical evolving shell-type phase front. Analytical and numerical characterizations are proposed, displaying quite a good agreement. In one spatial dimension, the system shows three types of stationary solitons with shell-like structure whereas in two spatial dimensions it displays only one, characterized by a π -phase jump far from the soliton position.

DOI: 10.1103/PhysRevLett.107.254102

PACS numbers: 05.45.Yv, 89.75.Kd

Macroscopic systems maintained out of equilibrium are characterized by the possibility of the emergence of particle-type solutions or localized states. These states have been observed in different fields such as magnetic materials, liquid crystals, gas discharge, chemical reactions, fluids, granular media, and nonlinear optics media, among others (see the reviews [1–3], and references therein). Although these states are spatially extended, they exhibit properties typically associated with particle-like states. Consequently, one can characterize them with a family of continuous parameters such as position, amplitude, and width. For time-reversible systems where injection and dissipation of energy can be viewed as perturbations—quasireversible systems [4]—the prototype model that exhibits localized states is the parametrically driven damped nonlinear Schrödinger equation [5]. This model has been derived in several contexts to describe the appearance of patterns and localized structures, such as vertically vibrated Newtonian fluid layers [6], nonlinear lattices [7], optical fibers [8], Kerr type optical parametric oscillators [9], easy-plane ferromagnetic materials exposed to an oscillatory magnetic field [10], and a parametrically driven damped chain of pendula [11]. One of the greatest benefits of this model is to present analytical solutions for localized states characterized by a constant phase and a bell-like shape for the amplitude [10].

In this Letter, we show that localized states of quasireversible parametric systems present an unexpectedly rich phase front dynamics. More precisely, the stationary localized states have a shell-type structure in the phase, for a large range of parameters. These stable structures are of three types. We term these solutions phase shielding solitons. Using the asymptotic amplitude equation, valid far from the position of the localized states, we determine analytically the shape of phase fronts and its dynamics. This dynamics is characterized by the juxtaposition of two forces, one due to relative stability between the phases and the other related to spatial variations of the tail of the dissipative soliton. As a result of this force balance, these

localized states exhibit a phase structure that shields the soliton. Numerical simulations show quite good agreement with our analytical predictions.

The envelope of an oscillation for extended conservative systems in the presence of small energy injection through a parameter modulation and energy dissipation—via damping phenomena—is described by the parametrically driven damped nonlinear Schrödinger equation

$$\partial_t \psi = -i\nu\psi - i|\psi|^2\psi - i\partial_{xx}\psi - \mu\psi + \gamma\bar{\psi}, \quad (1)$$

where the envelope $\psi(x, t)$ is a one-dimensional complex field, $\bar{\psi}$ stands for the complex conjugate of ψ , and $\{x, t\}$ describe, respectively, the spatial and temporal coordinates. The detuning parameter is ν , which is proportional to the difference between half of the forcing frequency and the natural frequency of the oscillator field. μ is the damping parameter, and γ stands for the forcing amplitude of the parametric forcing. The higher-order terms in Eq. (1) are ruled out by a scaling analysis, since $\mu \ll 1$, $\nu \sim \mu \sim \gamma$, $|\psi| \sim \mu^{1/2}$, $\partial_x \sim \mu^{1/2}$, and $\partial_t \sim \mu^{1/2}$.

Introducing the following change of variables $\psi = R(x, t)e^{i\varphi(x, t)}$ in Eq. (1), the model reads

$$\partial_t R = 2\partial_x R \partial_x \varphi + R \partial_{xx} \varphi - \mu R + \gamma R \cos(2\varphi), \quad (2)$$

$$\partial_t \varphi = -\nu - R^2 - \frac{\partial_{xx} R}{R} + (\partial_x \varphi)^2 - \gamma \sin(2\varphi), \quad (3)$$

where R and φ stand for the amplitude and phase of ψ , respectively. The previous set of equations in the region of parameters $-\nu - \sqrt{\gamma^2 - \mu^2} \geq 0$, exhibit stationary dissipative solitons of the form $R_s(x, x_0) = \sqrt{2\delta} \operatorname{sech}(\sqrt{\delta}[x - x_0])$ and $\varphi_s = \arccos(\mu/\gamma)/2$ with $\delta \equiv -\nu + \sqrt{\gamma^2 - \mu^2}$ [10] [see Fig. 1(a)]. Hence, the localized states are defined as having a bell shape in the modulus and a constant phase. However, when we try to observe the previous solution, numerical simulations show that an unexpected and rich phase dynamics arises. Such dynamics initially establishes a bell shape in the modulus

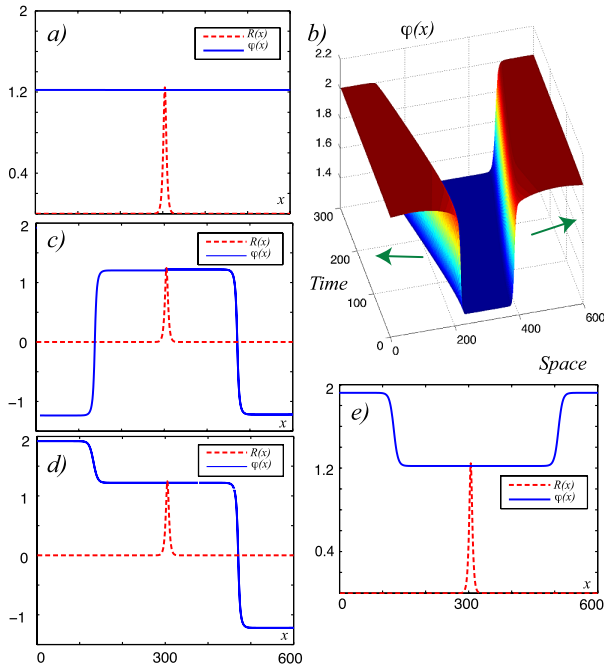


FIG. 1 (color online). Solitons in the parametrically driven damped nonlinear Schrödinger equation: (a) soliton with constant phase; (b) space-time diagram for the phase $\varphi(x, t)$ of Eq. (1) with $\gamma = 0.123$, $\nu = -0.093$, and $\mu = 0.100$; (c), (d), and (e) solitons with phase shell-like structure obtained numerically from Eq. (1) for $\gamma = 0.083$, $\nu = -0.063$, and $\mu = 0.058$.

of the amplitude. Then, a constant phase appears around the position of the localized state. At a latter stage, after some intricate transients, a pair of fronts that connect different phase equilibrium emerge. These equilibria are characterized by $\cos(2\varphi_0) = \mu/\gamma$. Finally, a rather slow dynamics of phase front propagation is established, which ends with the formation of a pair of stationary fronts that connect steady states. Figure 1(b) illustrates the above described time evolution of phase dynamics. The system has four phase equilibria in the range from $-\pi$ to π . Therefore, the stable dissipative solitons have three types of shell-like phase structures. Figures 1(c)–1(e) outline these solutions. Because of the fact that the function $\cos(2\phi)$ has period π , the phase difference at the ends of the dissipative soliton can be zero or π (cf. Fig. 1). Thus, this last localized state is characterized by a phase difference given by zero around the core and π at the ends. It is important to mention that dissipative solitons represented in Figs. 1(a), 1(c), and 1(e), are homoclinic orbits for the spatial system in polar representation $\{R, \varphi\}$. However, the dissipative soliton shown in Fig. 1(d) corresponds to a heteroclinic solution. In Cartesian representation $\{\text{Re}(A), \text{Im}(A)\}$ all these solutions correspond to homoclinic orbits.

For the purpose of understanding and capturing the wealth of these phase front solutions, let us consider

Eq. (1) in a semi-infinite domain, with zero flux boundary conditions. The system can exhibit a dissipative soliton located at one edge, with the phase formed by a single front [see Fig. 2(a)]. In addition it is worth noting that these phase fronts emerge at a distance far from the core of the soliton, i.e., at a distance much larger than $1/\sqrt{\delta}$. Accordingly, $R(x, x_0) \approx 2\sqrt{2\delta}e^{-\sqrt{\delta}(x-x_0)}$ for $x - x_0 \gg 0$, with x_0 at the left edge of the region of interest. Together with Eq. (2) this approximation leads to the following Newton-type equation

$$\partial_{xx}\varphi = 2\sqrt{\delta}\partial_x\varphi + \mu - \gamma\cos(2\varphi). \quad (4)$$

This equation has heteroclinic solutions corresponding to phase fronts, which analytically are well described by

$$\varphi_F(x, x_f) \approx \arctan\left[\sqrt{\frac{\gamma \pm \mu}{\gamma \mp \mu}} \tanh\frac{\sqrt{\gamma^2 - \mu^2}(x - x_f)}{2\sqrt{\delta}}\right], \quad (5)$$

where x_f accounts for the position of phase front, i.e., the point at which the spatial derivative of the phase front has its global maximum. Thus, the phase front solutions are parametrized by a continuous parameter x_f . Figure 2 shows the numerically computed phase fronts, which present a difference of 1% with respect to expression (5). Notice that if one considers the first correction to the previous equation $\varphi \approx \varphi_F + \partial_x\varphi_F/2\sqrt{\delta}$ this difference decreases to 0.8%.

As it can be also seen from Fig. 2(b), this front displays an unexpected dynamical behavior characterized by a non-uniform translation. To describe this dynamics, we promote the front position to a time-dependent function $x_f(t)$. Hence, using Eq. (3) and formula (5), we obtain

$$-\dot{x}_f\partial_x\varphi_F = -(\nu + \delta) - 8\delta e^{-2\sqrt{\delta}x} + (\partial_x\varphi_F)^2 - \gamma\sin(2\varphi_F), \quad (6)$$

where \dot{x}_f stands for the time derivative of x_f . Multiplying the above equation by $\partial_z\varphi_F$ with $z \equiv x - x_f$, and introducing the following inner product $\langle f|g \rangle \equiv \int fg dz$, we obtain the following equation for the phase front after straightforward calculations,

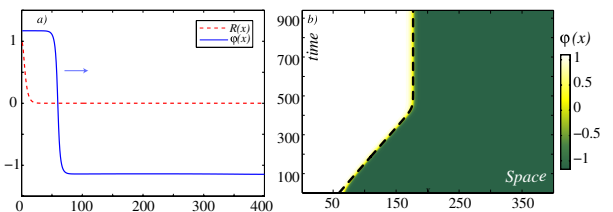


FIG. 2 (color online). Phase propagation: (a) phase front profile considering half of the dissipative soliton; (b) spatiotemporal diagram of phase front obtained from Eq. (1) by $\gamma = 0.083$, $\nu = -0.063$, and $\mu = 0.058$. The dashed curve is the numerical solution obtained using Eq. (7).

$$\dot{x}_f = A + B e^{-2\sqrt{\delta}x_f}, \quad (7)$$

where

$$A \equiv \frac{\langle (\nu + \delta + \gamma \sin(2\varphi_F) - (\partial_z \varphi_F)^2) | \partial_z \varphi_F \rangle}{\langle \partial_z \varphi_F | \partial_z \varphi_F \rangle},$$

$$B \equiv 8\delta \frac{\langle e^{-2\sqrt{\delta}z} | \partial_z \varphi_F \rangle}{\langle \partial_z \varphi_F | \partial_z \varphi_F \rangle}$$

are real numbers, which can be either positive or negative depending on the shape of the phase front. For example, when one considers a front that increases monotonically with the spatial coordinate, A (B) is a negative (positive) constant. The term proportional to A accounts for the constant speed at which the larger phase invades the smaller value. This speed can be understood as a consequence of the energy difference between these states. Hence, this term gives rise to phase fronts propagating towards the soliton position. Conversely, the term proportional to B accounts for the effect of spatial variation of the tail of the amplitude soliton, which induces a force that leads to phase fronts moving away from the localized state. Consequently, the superposition of these two opposing forces generates a stable equilibrium for the position of the phase front, which is consistent with the dynamics illustrated in the space-time diagram in Fig. 2. The dashed curve in Fig. 2(b) represents the solution obtained from Eq. (7), using the above formulas A and B . Modifying the parameters, we observe that as γ increases the equilibrium position is smaller; i.e., the shell-type structure surrounding the soliton decreases. Instead, as ν increases the equilibrium position of the phase front also grows.

Considering now the soliton located at the center of the spatial region, a small disturbance on the system produces some complex transients on the phase dynamics, ending by the formation of a pair of fronts propagating in opposite directions away from the soliton core. The dynamics of these fronts differs from that of the single front by the inclusion of an interaction process which decays exponentially with the distance between the fronts. As the system displays two types of phase fronts monotonically increasing or decreasing, then the soliton exhibits three different types of shield structures in its phase, as shown in Fig. 1. Hence, the dissipative solitons in parametrically driven systems have a rich dynamics of phase fronts.

To understand the correspondence between the constant phase solitons and phase shielding solitons, we have performed a numerical linear stability analysis similar to the one made in Ref. [12], considering both the control parameters and size of the system L . When L is small enough the spectrum—set of eigenvalues associated with the linear stability analysis—is characterized by being centered on an axis parallel to the imaginary one [cf. Fig. 3(b)], where every single eigenvalue begin to collide creating a curve of eigenvalues (a continuum). For a critical value of L this

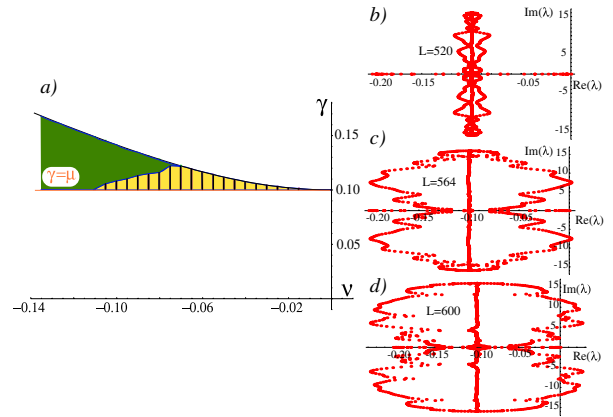


FIG. 3 (color online). Stability of solitons: (a) schematic representation of bifurcation diagram in the $\gamma - \nu$ space for $\mu = 0.050$, the shaded region corresponds to the phase shielding soliton region, and the striped area is the region of soliton with constant phase. (b), (c), and (d) are the spectra of the soliton with constant phase before (system size $L = 520$), during ($L = 564$), and after ($L = 600$) the bifurcation, respectively, for $\gamma = 0.263$, $\mu = 0.050$, and $\nu = -0.083$.

curve collides with the imaginary axis at a nonzero frequency [cf. Fig. 3(c)]. Therefore the system exhibits an Andronov-Hopf bifurcation. Figure 3 outlines the spectrum before, during, and after the bifurcation.

From previous numerical analysis, one can infer that the soliton with homogeneous phase is unstable, over a wide parameter region, for sufficiently large values of L . In short, there exists a critical value of L for which the soliton with constant phase is unstable to small perturbations in phase and amplitude. Because of the analytical complexity of this analysis, we have only determined numerically this critical value. For a system size smaller than the critical one, we observe that for parameters $0 < \gamma - \mu \ll 1$, the soliton with constant phase is stable. Increasing the forcing amplitude γ , the soliton becomes unstable by an Andronov-Hopf bifurcation similar to the one shown in Fig. 3. This figure illustrates the region in parameter space where this solution is stable and unstable. In the shaded region in Fig. 3, we found stable phase shielding solitons.

To study the robustness of the phase dynamics around the soliton, we consider the two-dimensional spatial extension of Eq. (1), that is, the ∂_{xx} operator is replaced by a two-dimensional Laplacian operator $\nabla^2 = \partial_{xx} + \partial_{yy}$. It is well known that this equation has soliton type solutions with a constant phase [13], which are the natural extensions of the one-dimensional case. However, an analytical expression for these solutions is unknown. Considering a similar parameter region of phase shielding solitons in one dimension, we observe a rich phase fronts dynamics in two dimensions. If one slightly perturbs the soliton, after some complex transient in the phase dynamics we observe the appearance of a circular phase front that spreads slowly.

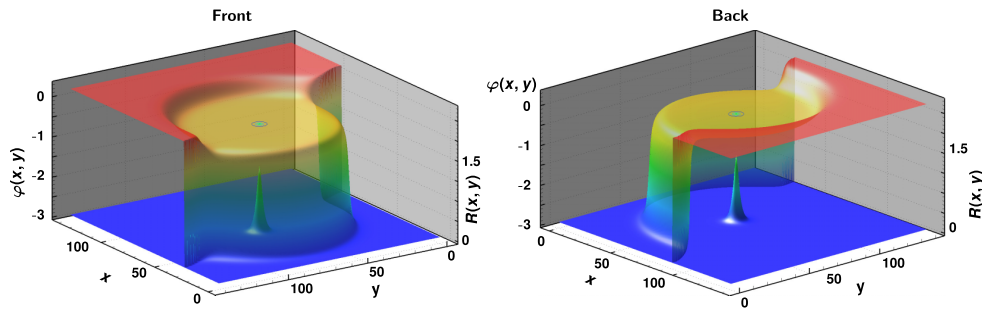


FIG. 4 (color online). Front and back view of a stationary phase shielding soliton observed in two dimensions for the parametrically driven damped nonlinear Schrödinger equation with $\gamma = 0.140$, $\nu = -0.068$, and $\mu = 0.125$. The phase and amplitude field are represented simultaneously. The colored shadow renders the phase shell-like structure $[\varphi(x, y)]$ that surrounds the amplitude soliton localized at the center $[R(x, y)]$.

For later times, the front becomes asymmetric, giving rise to another front. Finally, the two fronts become stationary, creating a shieldlike structure around the soliton. Figure 4 shows the stationary phase structure observed numerically in a two-dimensional system. It is important to note that we only see phase shielding structure as a state of equilibrium for dissipative soliton in a large system size. The two-dimensional solution is characterized by being composed of all the solutions found in one dimension. Indeed, if one performs different cuts containing the center (soliton position), one can recognize the observed solutions in one dimension (see Fig. 1). A surprising property of the shell-like structure observed is that if one calculates the phase change on a path that connects two opposite points with respect to the position of the soliton ($\int_{\Gamma} \vec{\nabla} \varphi d\vec{s}$) within the region close to the position of the soliton one finds that this is zero. Nevertheless, if one takes this type of path far away from the soliton position, one finds $\int_{\Gamma} \vec{\nabla} \varphi d\vec{s} = \pm \pi$.

In conclusion, localized structures in parametrically forced systems have a rich and unexpected phase dynamics, creating novel types of localized states. We expect that phase shielding solitons could be observed experimentally in simple coupled forced oscillators, such as vertically driven fluid layers in narrow cells, optical parametrical oscillators, driven magnetic media, and a chain of coupled oscillators.

Shell-like phase structure must play a significant role in soliton interaction, since bound states of two solitons show a complex phase structure [14]. Experimental observations show an intricate temporal dynamics of dissipative solitons [15] which cannot be explained from uniform phase solitons. Work in this direction is in progress.

The authors thank C. Falcón for fruitful discussions. The authors acknowledge financial support by the ANR-CONICYT 39, “Colors.” M.G.C. and M.A.G-N. are thankful for the financial support of FONDECYT

Projects No. 1090045 and No. 3110024, respectively. M. G. C. also acknowledges ACT Project No. 127.

-
- [1] *Localized States in Physics: Solitons and Patterns*, edited by O. Descalzi, M. Clerc, S. Residori, and G. Assanto (Springer, New York, 2010).
 - [2] H. G. Purwins, H. U. Bodeker, and Sh. Amiranashvili, *Adv. Phys.* **59**, 485 (2010).
 - [3] T. Ackemann, W. J. Firth, and G. L. Oppo, *Adv. At. Mol. Opt. Phys.* **57**, 323 (2009).
 - [4] M. Clerc, P. Couillet, and E. Tirapegui, *Phys. Rev. Lett.* **83**, 3820 (1999); *Int. J. Bifurcation Chaos Appl. Sci. Eng.* **11**, 591 (2001); *Opt. Commun.* **167**, 159 (1999); *Phys. Lett. A* **287**, 198 (2001); *Prog. Theor. Phys. Suppl.* **139**, 337 (2000).
 - [5] I. V. Barashenkov and E. V. Zemlyanaya, *Phys. Rev. Lett.* **83**, 2568 (1999).
 - [6] J. W. Miles, *J. Fluid Mech.* **148**, 451 (1984); W. Zhang and J. Viñals, *Phys. Rev. Lett.* **74**, 690 (1995); X. Wang and R. Wei, *Phys. Rev. E* **57**, 2405 (1998); M. G. Clerc *et al.*, *Phil. Trans. R. Soc. A* **367**, 3213 (2009).
 - [7] B. Denardo *et al.*, *Phys. Rev. Lett.* **68**, 1730 (1992).
 - [8] J. N. Kutz *et al.*, *Opt. Lett.* **18**, 802 (1993).
 - [9] S. Longhi, *Phys. Rev. E* **53**, 5520 (1996).
 - [10] I. V. Barashenkov, M. M. Bogdan, and V. I. Korobov, *Europhys. Lett.* **15**, 113 (1991); M. G. Clerc, S. Coulibaly, and D. Laroze, *Physica (Amsterdam)* **239D**, 72 (2010).
 - [11] N. V. Alexeeva, I. V. Barashenkov, and G. P. Tsironis, *Phys. Rev. Lett.* **84**, 3053 (2000).
 - [12] N. V. Alexeeva, I. V. Barashenkov, and D. E. Pelinovsky, *Nonlinearity* **12**, 103 (1999).
 - [13] I. V. Barashenkov, N. V. Alexeeva, and E. V. Zemlyanaya, *Phys. Rev. Lett.* **89**, 104101 (2002).
 - [14] I. V. Barashenkov and E. V. Zemlyanaya, *Phys. Rev. E* **83**, 056610 (2011); E. Kenig *et al.*, *Phys. Rev. E* **80**, 046202 (2009).
 - [15] W. Wei *et al.*, *Phys. Lett. A* **219**, 74 (1996).

Interaction law of 2D localized precession states

M. G. CLERC¹, S. COULIBALY^{2(a)} and D. LAROZE^{3(b)}

¹ *Departamento de Física, FCFM, Universidad de Chile - Casilla 487-3, Santiago, Chile*

² *Laboratoire de Physique des Lasers, Atomes et Molécules, CNRS UMR 8523, Centre d'Etudes et de Recherches Lasers et Applications, Université des Sciences et Technologies de Lille - 59655 Villeneuve d'Ascq Cedex, France, EU*

³ *Instituto de Alta Investigación, Universidad de Tarapacá - Casilla 7D, Arica, Chile*

received 9 February 2010; accepted in final form 3 May 2010
published online 1 June 2010

PACS 89.75.Kd – Patterns

PACS 75.10.Hk – Classical spin models

PACS 75.25.-j – Spin arrangements in magnetically ordered materials (including neutron and spin-polarized electron studies, synchrotron-source X-ray scattering, etc.)

Abstract – A theoretical study of the interaction of localized precession states on an easy-plane ferromagnetic layer submitted to a magnetic field that combines a constant and an oscillating part is reported. Within the framework the Landau-Lifshitz-Gilbert equation, we perform a comparison of analytical studies and micromagnetic simulations. Close to the parametric resonance, the parametrically driven damped nonlinear Schrödinger equation models this system. By means of this amplitude equation we are able to characterize the localized precession states and their pair interaction law. Numerically, we have a good agreement with the pair interaction law.

Copyright © EPLA, 2010

Introduction. – During the last years, emerging macroscopic particle-type solutions or localized states in macroscopic extended dissipative systems have been observed in different fields, such as: domains in magnetic materials, chiral bubbles in liquid crystals, current filaments in gas discharge, spots in chemical reactions, localized states in fluid surface waves, oscillons in granular media, isolated states in thermal convection, solitary waves in nonlinear optics, among others. Hence, one can infer the universality of the localized-states dynamics. Although these states are spatially extended, they exhibit properties typically associated with particles. Consequently, one can characterize them with a family of continuous parameters such as position, amplitude and width. This is exactly the type of description used in more fundamental physical theories like quantum mechanics and particle physics. However, localized states emerging in extended dissipative systems are characterized by being made of a large number of atoms or molecules (of the order of Avogadro's number) that behave coherently. The paradigmatic example of macroscopic localized states are solitons reported in the context of fluid dynamics, nonlinear optics and Hamiltonian systems [1]. The

solitons arise from a robust balance between dispersion and nonlinearity. The generalization of this concept to dissipative and out-of-equilibrium systems has led to several studies in the last decades, in particular to the definition of *localized structures* intended as patterns appearing in a restricted region of space [2,3].

In one-dimensional systems, localized states can be described, geometrically speaking, as spatial trajectories that connect a steady state with itself, that means, they are homoclinic orbits from the viewpoint of the dynamical-systems theory (see the review [4] and references therein), while domain walls or fronts are seen as spatial trajectories joining two different steady states—heteroclinic curves—of the corresponding spatial dynamical system [5]. In a particular case the localized patterns can be understood as homoclinic orbits in the Poincaré section of the corresponding spatial-reversible dynamical system [4–7]. The particular case of localized patterns can also be understood as a consequence of the interaction of fronts with oscillatory tails [8,9]; the characterization of such a localized structure is well known and details can be found in [10,11]. All the aforementioned scenario cannot be extended to localized states in two-dimensional space systems, which currently lack an equivalent geometrical description as those developed in the one-dimensional systems [4]. There is another type of stabilization mechanism that generates localized structures without

^(a)E-mail: saliya.coulibaly@phlam.univ-lille1.fr

^(b)Current address: Max Planck Institute for Polymer Research - 55021 Mainz, Germany, EU.

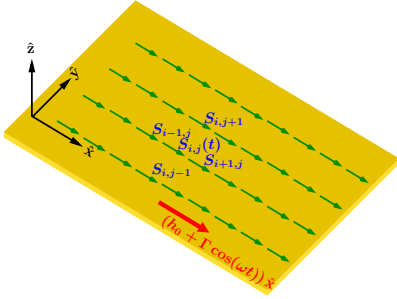


Fig. 1: (Colour on-line) Schematic representation of an uniaxial anisotropic Heisenberg ferromagnetic layer. Small arrows represent the local magnetization ($\mathbf{S}_{i,j}$) and the large arrow stands for the external magnetic field.

oscillatory tails based on non-variational effects [12], where the fronts interaction is led by the non-variational terms [13]. Localized structures that we shall study are of non-variational type.

A characteristic property of particle-type solutions is that their interaction can be described simply in terms of continuous parameters describing the localized states. Recently, improved experimental techniques have increased the interest in the study of interaction of localized states [14,15]. The understanding of the pair interaction law of localized states allows us to comprehend the evolution of the system to equilibrium; more importantly, we expect a more efficient management and control of these localized states for their potential applications. This has a particular technological interest in new storage media like semiconductor cavity [16]. One of the most prominent parametric oscillators in the context of spintronics are the nanopillars [17], the ability to generate and study the localized structures and the interaction between them opens up the possibility of developing new magnetic devices.

The aim of this letter is to study, in the classical spin limit, the interaction of localized precession states on an easy-plane ferromagnetic spin layer submitted to an external magnetic field that combines a constant and an oscillating part. This magnetic system is described phenomenologically by the Landau-Lifshitz-Gilbert equation. In this framework we perform a comparative study of analytical results and micromagnetic simulations. Close to the parametric resonance, the parametrically driven damped nonlinear Schrödinger equation models this system. By means of this amplitude equation we are able to characterize the pair interaction law between localized excitations. Numerically, we have a good agreement with the proposed pair interaction law.

Parametrically driven magnetic layer. – Let us consider a two-dimensional anisotropic Heisenberg ferromagnetic layer formed by $N_x \times N_y$ spins or magnetic moment exposed to an external magnetic field, which is contained in the plane (x, y) and oriented in the direction

$\hat{\mathbf{x}} \equiv (1, 0, 0)$. Figure 1 depicts the setup of the system under study. When the quantum effects are small enough, the spin vectors $\mathbf{S}_{i,j}$ can be treated as classical spin or magnetic moment [18] and satisfies the dynamical evolution $\dot{\mathbf{S}}_{i,j} = -\gamma \mathbf{S}_{i,j} \times (\partial \mathcal{H} / \partial \mathbf{S}_{i,j})$ [19], where γ is the gyromagnetic constant and the Hamiltonian \mathcal{H} has the form [20]

$$\mathcal{H} = \sum_{i,j}^N (-J_x \mathbf{S}_{i,j} \mathbf{S}_{i+1,j} - J_y \mathbf{S}_{i,j} \mathbf{S}_{i,j+1} + 2D(S_{i,j}^z)^2 - g\mu(S_{i,j}^x)H_x). \quad (1)$$

Here, $\{J_x, J_y\}$ are the exchange coupling constants which are of the same order of magnitude, H_x and D account for the external magnetic field and the anisotropy energy, respectively. The characterization and the understanding of this discrete system is a complicated task. Hence we study the continuum limit of this set of the ordinary differential equations [18,21]. Thus we can assume that $\mathbf{S}_{i,j}(t) \rightarrow \mathbf{S}(\vec{r}, t)$, where $\vec{r}(x, y)$ accounts for the coordinates describing the magnetic plane and taking the limit $J_x \gamma (\mathbf{S}_{i+1,j} - 2\mathbf{S}_{i,j} + \mathbf{S}_{i-1,j}) + J_y \gamma (\mathbf{S}_{i,j+1} - 2\mathbf{S}_{i,j} + \mathbf{S}_{i,j-1}) \rightarrow (l_x \partial_x^2 + l_y \partial_y^2) \mathbf{S}$, scaling the spatial coordinates $(l_x \partial_x^2 + l_y \partial_y^2) \mathbf{S} \rightarrow l_{ex} \nabla_{\perp}^2 \mathbf{S}$, where l_{ex} denotes the characteristic interaction length and ∇_{\perp}^2 is the Laplacian operator in the new transversal coordinates ($\nabla_{\perp}^2 \equiv \partial_{xx} + \partial_{yy}$). Finally, introducing phenomenologically the Gilbert damping, the motion of the magnetization field is governed by the well-known Landau-Lifshitz-Gilbert equation

$$\partial_{\tau} \mathbf{M} = \mathbf{M} \times [\nabla_{\perp}^2 \mathbf{M} - \beta (\mathbf{M} \cdot \hat{\mathbf{z}}) \hat{\mathbf{z}} + \mathbf{H}_e - \alpha \partial_{\tau} \mathbf{M}], \quad (2)$$

where $\mathbf{M} \equiv \mathbf{S}/M_s$ stands for the unit vector of the magnetization, with M_s the saturation magnetization; we have also considered the following normalization of scales and parameters $\{\tau \rightarrow \gamma M_s t, \beta \rightarrow 4D/\gamma M_s, \mathbf{H}_e \rightarrow g\mu \mathbf{H}/\gamma M_s\}$, where $\beta > 0$ is the uniaxial easy-plane anisotropy constant, and α is the damping parameter. This damping parameter for a great quantities of materials is small. Assuming that the external magnetic field is constant and neglecting damping effects ($\alpha = 0$), the dynamics of model (2) is time reversible. However, when we consider the effects of damping and an external magnetic field with both a constant and an oscillatory part, model (2) becomes a quasi-reversible type, *i.e.* a time reversible system perturbed with injection and dissipation of energy. The instabilities of these types of systems have been studied during the last decades [22].

As a result of the anisotropy and constant external field ($\mathbf{H}_e = h_0 \hat{\mathbf{x}}$), the natural equilibrium of the previous model (2) corresponds to the magnetization field lying in the direction of the external magnetic field, $\mathbf{M} = \hat{\mathbf{x}}$ (cf. fig. 1). When spatial coupling is ignored, it is easy to show that the dynamics around this equilibrium is described by a nonlinear oscillator with natural frequency $\omega_0 = \sqrt{h_0(\beta + h_0)}$ [23,24]. It is worthy to note that in

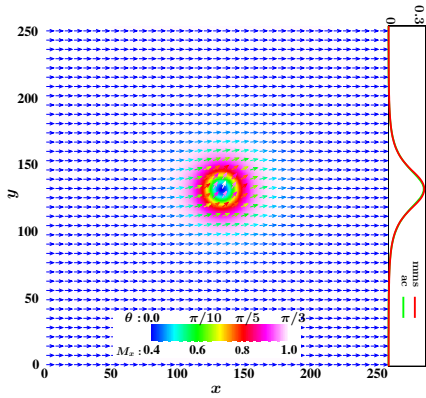


Fig. 2: (Colour on-line) Localized precession states obtained from micromagnetic simulation (mms) of model (2) by $\beta = 1$, $h_0 = 0.1$, $\alpha = 0.01$, $\Gamma = 0.009$ and $\omega = 0.328$. The background color describes the value of the intensity of M_x . The arrows represent the instantaneous local magnetization unit vector \mathbf{M} . Its respective color scale accounts for the value of the angle $\theta \equiv (\hat{\mathbf{x}}, \mathbf{M})$. The inset shows a profile of M_y and is compared with the variational approximation (ac) given by (5).

eq. (2), the magnetization components are proportional to the external magnetic field, which therefore acts as a parametric forcing. Then if this field combines a constant and a time-periodic part ($\mathbf{H}_e = [h_0 + \Gamma \cos(\omega t)]\hat{\mathbf{x}}$ oscillating about twice the natural frequency ($\omega \equiv 2(\omega_0 + \nu)$, where ν is the detuning parameter), the system exhibits a parametric resonance at $\Gamma^2(\beta/4\omega_0)^2 = \alpha^2(\beta/2 + h_0)^2 + \nu^2$ for small $\{\nu, h_0, \alpha, \Gamma\}$ —Arnold’s tongue. Dynamically speaking this resonance corresponds to an undamped precession of the magnetization unit vector around the direction of the external magnetic field with the angular velocity ω_0 .

Localized precession states. — The inclusion of spatial coupling should increase the complexity of the dynamics. For example, one expects the formation of patterns, domain walls, and localized states near the parametric resonance. This wide range of phenomena is described in a unified manner near the parametric resonance by the parametrically driven damped nonlinear Schrödinger equation [25]. In order to show that the LLG system can exhibit this kind of solutions, we have numerically solved (2) using the fixed step fourth-order Runge-Kutta scheme ($dt = 10^{-4}$), over a square lattice of size 250×250 a.u. with spatial a discretization step set to 0.1 in both directions. Numerical solutions of (2) are simultaneously compared with those obtained by integration of the equivalent stereographic representation [26] in order to check their accuracy. Figure 2 illustrates the typical non-propagative localized precession states obtained from these simulations. This magnetic state, is characterized by a localized precession surrounded by a static magnetic state that lies in the x -direction.

Changing the detuning and the amplitude of the forcing, the system exhibits a stable uniform precession state,

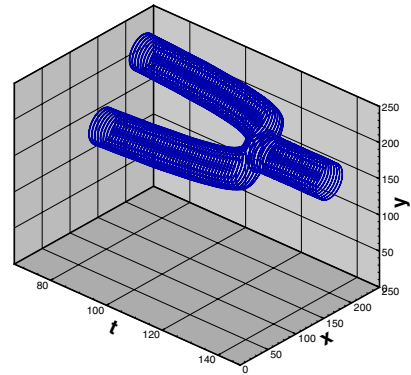


Fig. 3: (Colour on-line) Space-temporal diagram of interaction of a pair of localized precession states obtained from model (2) by the same parameters of fig. 1. The circles represent the core of the localized states, *i.e.* the isolines of the full width at half maximum of the localized state.

which exhibits a spatial instability when the detuning is decreased. This instability is characterized initially by the appearance of a pattern with a well-defined wavelength, which then decomposes into a gas of localized precession states. The subsequent dynamics of this system is led by the interaction of these states. This interaction is characterized by the collision of a pair of localized states, ended by a coalesce process from which there emerges a single localized precession state. In fig. 3 this process is shown.

Parametrically driven damped nonlinear Schrödinger equation. — To understand the localized precession state and the interaction between them, in the quasi-reversible limit ($\Gamma \sim \nu \sim \alpha \ll \omega_0$) and close to the parametric resonance, we can introduce the following Ansatz [23,24] into eq. (2):

$$\begin{aligned} M_x &\approx 1 - \frac{M_y^2 + M_z^2}{2}, \\ M_y &\approx \frac{1}{h_0} \left[1 + \frac{\Gamma}{h_0} \right] \dot{M}_z, \\ M_z &\approx 4\sqrt{\frac{\omega_0 h_0}{\beta(\omega_0^2 + 3h_0^2)}} \psi(\vec{r}, t) e^{i(\omega_0 + \nu)t} + c.c., \end{aligned} \quad (3)$$

to the dominant order. After straightforward calculations and imposing a solvability condition for the corrections of the previous Ansatz we find (*the parametrically driven damped nonlinear Schrödinger equation*)

$$\partial_t \psi = -i\nu\psi - i|\psi|^2\psi - i\nabla_{\perp}^2 \psi - \mu\psi + \gamma\bar{\psi}, \quad (4)$$

with $\gamma \equiv \beta\Gamma/4\omega_0$ and $\mu \equiv (\beta/2 + h_0)\alpha$. This model has been derived in several contexts to describe pattern and localized structures, such as vertically oscillating layers of water [27], nonlinear lattices [28], optical fibers [29], Kerr-type optical parametric oscillators [30], among others.

It is well known that eq. (4) exhibits stable non-propagative dissipative solitons in two spatial dimensions [31]. The localized states have the form $\psi = \pm R_s(r = |\vec{r}'|)e^{i\theta_0}$, where $\cos(2\theta_0) = \mu/\gamma$, and R_s satisfies the equation $\partial_{r'r}R_s + \partial_r R_s/r - \lambda R_s + R_s^3 = 0$, where $\lambda \equiv -\nu + \sqrt{\gamma^2 - \mu^2} > 0$. To our knowledge, there does not exist an analytical solution of the localized state. However the asymptotic behaviors of this solution are well defined: for instance $R(r \rightarrow \infty) \rightarrow e^{-\sqrt{\lambda}r}/\sqrt{r}$. Furthermore, using the variational method, one can also obtain a good approximation by [32]

$$R_s(r) = A_0\sqrt{\lambda} \operatorname{sech} \left(B_0\sqrt{\frac{\lambda}{2}}r \right), \quad (5)$$

where $A_0 = 2.166$ and $B_0 = 1.32$. From this variational approach and using the Ansatz (3), one can have an adequate representation for the localized precession states. In inset of fig. 2, we contrasted this approach with those obtained from micromagnetic simulations of the model (2). We note that there is a quite good agreement.

From the approximated localized state (5), one can infer that for negative detuning, this solution appears by a saddle-node bifurcation when dissipation and energy injection are equal ($\gamma = \mu$ and $\nu < 0$). Furthermore, this solution is unstable when the uniform magnetization $\mathbf{M} = \hat{\mathbf{x}}$ —which supports this localized state—becomes unstable at Arnold's tongue ($\gamma^2 = \nu^2 + \mu^2$, by $\nu < 0$). The characteristic size and amplitude of the localized precession states, respectively, are $1/\sqrt{\lambda}$ and $\sqrt{\lambda}$.

Pair interaction law of localized states. — We consider two localized states sufficiently separated, *i.e.* the distance between them is greater than the characteristic size of the localized states. Hence, we can introduce the following Ansatz: $\psi(r, t) = R(r, t)e^{i\theta(r, t)}$,

$$R = R_s^+ \left(r + \frac{\Delta(t)}{2}\hat{r} \right) + \chi R_s^- \left(r - \frac{\Delta}{2}\hat{r} \right) + \rho(\vec{r}, \Delta), \quad (6)$$

$$\theta = \theta_0 + \varphi(\vec{r}, \Delta),$$

where R_s^\pm are non-propagative dissipative solitons, $\Delta(t)$ stands for the distance between the localized states ($\Delta \gg \sqrt{\lambda}$), \hat{r} is the unit vector in the direction between the localized states, $\chi = \pm 1$ is a sign that defines whether the solutions are in or out of phase, $\rho(\vec{r}, \Delta)$ and $\varphi(\vec{r}, \Delta)$ are, respectively, the corrections functions. Defining $W \equiv R_s^+ + \chi R_s^-$, considering the parameter region where the dissipation and injection of energy are similar ($0 < \gamma - \mu \ll 1$), introducing the above Ansatz into eq. (4) and linearizing correction functions, we obtain

$$W\partial_t W = \vec{\nabla}_\perp (W^2 \vec{\nabla}_\perp \varphi), \quad (7)$$

$$W\partial_t \varphi = \mathcal{L}\rho - 2\mu\varphi - 3\chi R_s^+ R_s^- W, \quad (8)$$

where $\mathcal{L} \equiv -\nu + \sqrt{\gamma^2 - \mu^2} + 3W^2 + \vec{\nabla}_\perp^2$ is a linear operator.

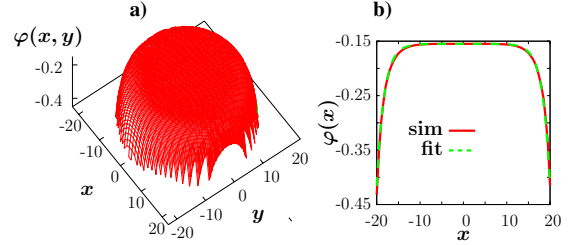


Fig. 4: (Colour on-line) Phase φ around one of the two interacting localized solitons of eq. (4) using $\gamma = 0.53$, $\mu = 0.25$ and $\nu = 0.05$. a) two-dimensional representation, b) solid and dashed lines are, respectively, the profile of φ obtained from the numerical simulation of model (4) and fit (9).

To solve the above equations, we need to derive φ . However finding a global solution for φ remains a difficult task. Nevertheless, if localized states are diluted we can find φ around the center of each dissipative soliton. In order to get φ , we changed our reference system by $\vec{r}' = \vec{r} + \hat{r}\Delta/2$, and in consequence, we approximate the functions $W(r' = |\vec{r}'|) \approx R_s^+(r')$ and $\partial_t W \approx \Delta \partial_{r'} R_s^+/2$. Next, using the approximation (5) and integrating eq. (7), after straightforward calculations we find out that

$$\varphi(r') = -\frac{\Delta}{4} \left(r' - \frac{1}{2B} \operatorname{Shi}(2Br') \right) \equiv \Delta \Theta(r'), \quad (9)$$

where $\operatorname{Shi}(2Br')$ is the hyperbolic sine integral. Figure 4 compares this approximation with those obtained from numerical simulations.

Replacing expression (9) into eq. (8), we find a linear equation in ρ . To solve this linear equation, we use the Fredholm alternative [2]. Therefore we introduce the following inner product: $\langle f|g \rangle = \iint fg \, dx dy$, where \mathcal{L} is self-adjoint and its kernel is characterized by $\{\partial_{r'} R_s^\pm\}$. Then applying this product to eq. (8), we find the following solvability condition (*pair interaction law*):

$$\begin{aligned} \Delta &= -\chi \frac{3}{a\mu} \int_0^{r'} \partial_{r'} R_s^-(R_s^-)^2 R_s^+ (\hat{\mathbf{r}}' - \Delta \hat{\mathbf{x}}) r' dr' d\theta \\ &\approx -\chi \frac{b}{a\mu} \frac{e^{-\sqrt{\lambda}\Delta}}{\sqrt{\Delta}}, \end{aligned} \quad (10)$$

where $a = \langle \partial_{r'} R_s^- | \Theta \rangle$ and $b \equiv 3A \int_0^{r'} \partial_{r'} R_s^-(R_s^-)^2 - e^{-\sqrt{\lambda}r \cos \theta} dr'$. The pair interaction law is derived using the asymptotic behavior of the localized state. Hence, the localized precession states experience an exponential force of attraction ($\chi = 1$) or repulsion ($\chi = -1$) if they are in or out of phase. In the limit of diluted localized states the prefactor $1/\sqrt{\Delta}$ is a correction of the dominant term which is exponential. However, when these states are located closer to this prefactor it becomes more relevant.

Hence the interaction of localized precession states is like over-damped two-dimensional particles with two types of charges where the interaction is only radial. In fig. 5 the evolution of the distance between the localized states

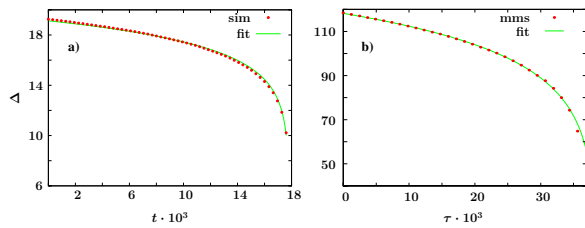


Fig. 5: (Colour on-line) Temporal evolution of the separation distance $\Delta(t)$. The points represent the separation distance obtained from a) micromagnetic simulations of the model (2) using the parameters of fig. 2 and b) numerical simulations of eq. (4), using the parameters of fig. 4. The solid line is the evolution of the separation distance deduced from the interaction law (10).

obtained using the pair interaction law is compared to those obtained from the numerical simulations of the parametrically driven damped nonlinear Schrödinger equation and micromagnetism simulations of the model (2). We find a remarkable agreement.

In the case of reversible two-dimensional systems, using Lagrangian methods one can derive a similar interaction law, however the radial dynamics can be enhanced by the appearance of tangential forces [33,34].

Conclusions. – We have theoretically studied the interaction of localized precession states on an easy-plane ferromagnetic spin layer submitted to a magnetic field that combines a constant and an oscillating parts. We have performed a comparison of analytical studies and micromagnetic simulations. Close to the parametric resonance, we are able to characterize the localized precession states and their pair interaction law. Numerically, we have a good agreement with the pair interaction law.

Given the numerical parameters that we have considered in the micromagnetic simulations in the case of permalloy ($M_s \simeq 10$ kOe) and Ni ($M_s \simeq 6.2$ kOe) the characteristic size of the localized precession state is 43 nm and 57 nm, respectively. Therefore the description presented here corresponds to a particular-type state of nanoscale.

The simulation software *DimX* developed at INLN, France, has been used for all the numerical simulations. MGC acknowledges the financial support of FONDECYT grant No. 1090045. DL thanks the partial financial support from FONDECYT No. 11080229, Millennium Scientific Initiative, P06-022-F, Financiamiento Basal para Centros Científicos Y Tecnológicos de Excelencia CEDENNA and Convenio de Desempeño UTA/Mineduc.

REFERENCES

[1] NEWELL A. C., *Solitons in Mathematics and Physics* (Society for Industrial and Applied Mathematics, Philadelphia) 1985.

[2] PISMEN L. M., *Patterns and Interfaces in Dissipative Dynamics*, in *Springer Series in Synergetics* (Springer, Berlin Heidelberg) 2006.

[3] CROSS M. and GREENSIDE H., *Pattern Formation and Dynamics in Nonequilibrium Systems* (Cambridge University Press, New York) 2009.

[4] COULLET P., *Int. J. Bifurcat. Chaos*, **12** (2002) 2445.

[5] VAN SAARLOOS W. and HOHENBERG P. C., *Phys. Rev. Lett.*, **64** (1990) 749.

[6] WOODS P. D. and CHAMPNEYS A. R., *Physica D*, **129** (1999) 147.

[7] HUNT G. W., LORD G. J. and CHAMPNEYS A. R., *Comput. Methods Appl. Mech. Eng.*, **170** (1999) 239.

[8] CLERC M. G. and FALCON C., *Physica A*, **356** (2005) 48.

[9] BORTOLOZZO U., CLERC U., FALCON C., RESIDORI S. and ROJAS R., *Phys. Rev. Lett.*, **96** (2006) 214501.

[10] KAWASAKI K. and OTHA T., *Physica A (Amsterdam)*, **116** (1982) 573.

[11] CAROLI B., CAROLI C. and FAUVE S., *J. Phys. I*, **2** (1992) 281.

[12] THUAL O. and FAUVE S., *J. Phys. (Paris)*, **49** (1988) 1829; *Phys. Rev. Lett.*, **64** (1990) 282.

[13] HAKIM V. and POMEAU Y., *Eur. J. Mech. B/Fluids, Suppl.*, **10** (1991) 137.

[14] BUCHANAN K. S. *et al.*, *Nat. Phys.*, **1** (2005) 172.

[15] ROTSCHEID C. *et al.*, *Nat. Phys.*, **2** (2006) 769.

[16] BARLAND S. *et al.*, *Nature*, **419** (2002) 699.

[17] YANG Z., ZHANG S. and LI Y. C., *Phys. Rev. Lett.*, **99** (2007) 134101.

[18] MIKESKA H. J., *J. Phys. C*, **11** (1978) L29.

[19] KOSEVICH A. M., IVANOV B. A. and KOVALEV A. S., *Phys. Rep.*, **194** (1990) 117.

[20] KITTEL C., *Rev. Mod. Phys.*, **21** (1949) 541.

[21] HERRING C. and KITTEL C., *Phys. Rev.*, **81** (1951) 869.

[22] CLERC M., COULLET P. and TIRAPEGUI E., *Phys. Rev. Lett.*, **83** (1999) 3820; *Int. J. Bifurcat. Chaos*, **11** (2001) 591; *Opt. Commun.*, **166** (1999) 159; *Phys. Lett. A*, **287** (2001) 198.

[23] BARASHENKOV I. V., BOGDAN M. M. and KOROBV V. I., *Europhys. Lett.*, **15** (1991) 113.

[24] CLERC M. G., COULIBALY S. and LAROZE D., *Phys. Rev. E*, **77** (2008) 056209; *Int. J. Bifurcat. Chaos*, **19** (2009) 3525; *Physica D*, **239** (2010) 72.

[25] COULLET P., FRISCH T. and SONNINO G., *Phys. Rev. E*, **49** (1994) 2087.

[26] LAKSHMANAN M. and NAKAMURA K., *Phys. Rev. Lett.*, **53** (1984) 2497 and references therein.

[27] MILES J. W., *J. Fluid Mech.*, **148** (1984) 451; ZHANG W. and VIÑALS J., *Phys. Rev. Lett.*, **74** (1995) 690; WANG X. and WEI R., *Phys. Rev. E*, **57** (1998) 2405; CLERC M. G. *et al.*, *Philos. Trans. R. Soc. A*, **367** (2009) 3213.

[28] DENARDO B. *et al.*, *Phys. Rev. Lett.*, **68** (1992) 1730.

[29] KUTZ J. N. *et al.*, *Opt. Lett.*, **18** (1993) 802.

[30] LONGHI S., *Phys. Rev. E*, **53** (1996) 5520.

[31] BARASHENKOV I. V., ALEXEEVA N. V. and ZEMLYANAYA E. V., *Phys. Rev. Lett.*, **89** (2002) 104101.

[32] ANDERSON D., BONNEDAL M. and LISAK M., *Phys. Fluids*, **22** (1979) 1838.

[33] STEBLINA V. V., KIVSHAR Y. S. and BURYAK A. V., *Opt. Lett.*, **23** (1998) 156.

[34] GORSHKOV K. A. and OSTROVSKY L. A., *Physica D*, **3** (1981) 428.

Abstract:

Nonlinear systems maintained out of equilibrium can spontaneously generate a variety of self-organized states called dissipative structures. Because of their ability to confine energy, the so-called localized dissipative structures are considered as the macroscopic analogues of elementary particles. As such they are of great interest of the community of the nonlinear science from optics to biology. In this book, problems related to these particle-like properties are discussed. The first part is devoted to the study of the interaction of two isolated or a diluted gas localized structures generated by parametric forcing: forcing by which one of the relevant parameters of the system is modulated. In the vicinity of the parametric resonance, such systems have in common to be described by the same reduced model, the parametrically driven and damped nonlinear Schrödinger equation. The soliton solutions of this equation have the particularity of having two arbitrary parameters: the position and a polarity parameter related to the phase. The interaction of two solitons of the same polarity has been shown to be attractive, resulting in the radiative fusion from which only one of the solitons remains. In the opposite case the solitons repel each other. Being repulsive or attractive, the interaction process is largely dominated by the asymptotic behavior of the solitons. For a multi-solitons states with the same polarity, the number of the remaining solitons follows a self-similar law derived from the isolated pair interaction. The second part of the paper summarizes my works related to the study of extreme events. Within a few years, the study of these very intense, rare and unpredictable localized structures has become a highly attractive research area. Although linear wave analysis can explain some aspects of the behavior of extreme events, it is generally accepted that nonlinearity plays a central role in the appearance of very high amplitude structures. Moreover, the recent observation of similarities between hydrodynamic and optical systems has led to the development of optical non-linear experimental devices to explore dynamic and stochastic aspects. Although the analogies between hydrodynamics and optics have been known since the 1960s, optical studies have shown in 2010 that this correspondence applies even within the limit of extreme nonlinear localization. This led to the first studies in conservative systems that allowed to link nonlinear turbulence processes to the generation of extreme events from noise. These studies have also revealed a new class of extreme events in the form of a rational localized structure known as the Peregrine soliton. However, despite the advances made by nonlinear optics, studies have often been limited to an essentially ideal class of extreme events in the absence of dissipation and more complex dynamics such as internal feedback loops. The works presented here show how the application of the tools of the theory of dynamic systems made it possible to make the link between the extreme events and the spatiotemporal chaos in dissipative systems.

Keywords: Dissipative Structures, Dissipative Solitons, Dynamical system theory, Spatiotemporal chaos, Extreme events

Résumé :

Les systèmes non-linéaires maintenus hors équilibre peuvent générer spontanément une diversité d'états auto-organisés appelés structures dissipatives. De par leur capacité à confiner de l'énergie, les structures dissipatives dites localisées, sont souvent considérées comme les analogues macroscopiques de particules élémentaires. A ce titre, elles cristallisent une grande partie des efforts de la communauté du non-linéaire de l'optique à la biologie. Dans cet ouvrage, des problématiques liées à ces propriétés de type particule sont abordées. La première partie est consacrée à l'étude de l'interaction de deux, puis de N structures localisées générées par forçage paramétrique: forçage par lequel un des paramètres pertinents du système est modulé. Au voisinage de la résonance paramétrique, tous les systèmes ont en commun le fait d'être décrits par le même modèle réduit: l'équation de Schrödinger non-linéaire paramétrique avec dissipation. Les solutions de type soliton de cette équation ont la particularité d'avoir deux paramètres arbitraires: la position et un paramètre de polarité lié à la phase. L'interaction de deux solitons de même polarité a été démontrée attractive avec pour résultat une fusion radiative de laquelle un seul des solitons subsiste. Dans le cas contraire l'interaction est répulsive. Répulsif ou attractif, le processus d'interaction est largement dominé par le comportement asymptotique des solitons. Pour plusieurs solitons de même polarité en interaction, l'évolution du nombre de soliton suit de façon auto-similaire la loi d'échelle obtenue pour deux solitons isolés. La deuxième partie du mémoire résume mes travaux consacrés à l'étude des événements extrêmes. En l'espace de quelques années, l'étude de ces structures localisées très intenses, rares et imprévisibles est devenue un sujet de recherche très attractif. Bien que l'analyse des ondes linéaires puisse expliquer certains aspects du comportement des événements extrêmes, il est généralement admis que la non-linéarité joue un rôle central dans l'apparition de structures d'amplitude très élevée. De plus, l'observation récente des similitudes entre les systèmes hydrodynamiques et optiques a conduit au développement de dispositifs expérimentaux non-linéaires optiques pour en explorer les aspects dynamiques et stochastiques. Bien que les analogies entre hydrodynamique et optique soient connues depuis les années 1960, ce n'est que très récemment, en 2010, que des études en optique ont montré que cette correspondance s'applique même dans la limite de localisation non-linéaire extrême. Cela a conduit aux premières études dans des systèmes conservatifs qui ont permis de lier des processus de turbulence non-linéaire à la génération d'événements extrêmes à partir du bruit. Ces études ont aussi permis la mise en évidence d'une classe fondamentalement nouvelle d'événements extrêmes sous forme de structure localisée rationnelle connue sous le nom de soliton de Peregrine. Pourtant, en dépit des avancées apportées par l'optique non-linéaire, les études se sont très souvent limitées à une classe essentiellement idéale d'événement extrême en l'absence de dissipation et de dynamique plus complexe. Les travaux présentés ici montrent comment l'application des outils de la théorie des systèmes dynamiques a permis de faire le lien entre les événements extrêmes et le chaos spatio-temporel dans des systèmes dissipatifs.

Mots-clés : Structure dissipatives, Solitons dissipatifs, Théorie des systèmes dynamiques, Chaos spatio-temporel, Événements extrêmes